Narrow-Band Single Photons as Carriers of Quantum Information

D I S S E R T A T I O N

zur Erlangung des akademischen Grades

Dr. rer. nat.
im Fach Physik

eingereicht an der
Mathematisch-Naturwissenschaftlichen Fakultät I
Humboldt-Universität zu Berlin

von
Dipl.-Phys. David Höckel
26.11.1979, Mainz

Präsident der Humboldt-Universität zu Berlin:
Prof. Dr. Dr. h.c. Christoph Markschies

Dekan der Mathematisch-Naturwissenschaftlichen Fakultät I:
Prof. Dr. Andreas Herrmann

Gutachter:
1. Prof. Dr. Oliver Benson
2. Prof. Achim Peters, Ph.D.
3. Prof. Dr. Christine Silberhorn

eingereicht am: 01.10.2010
Tag der mündlichen Prüfung: 13.12.2010

Zusammenfassung

Die Nutzung von Quanteneigenschaften für die Informationsverarbeitung, die sogenannte *Quanteninformationsverarbeitung* (QIP), ist ein seit zwei Jahrzehnten zunehmend populäres Forschungsfeld. Es hat sich gezeigt, dass Einzelphotonen die am besten geeigneten Träger für den Transport von Quanteninformation über weite Strecken sind, etwa um verschiedene Verarbeitungseinheiten in der QIP zu verbinden. Obwohl viele Methoden zur Erzeugung von Einzelphotonen existieren, wurde bisher nur wenig Forschungsarbeit an *schmalbandigen* Einzelphotonen, d.h. mit spektralen Breiten im MHz-Bereich geleistet. Allerdings sind solche Einzelphotonen besonders wichtig, wenn Kopplungen zwischen Einzelphotonen und atomaren Systemen, die oft als Verarbeitungseinheiten in der QIP genutzt werden, realisiert werden sollen. Diese Doktorarbeit befasst sich mit mehreren Forschungsaspekten zu schmalbandigen Einzelphotonen, die alle von Bedeutung sind, wenn solche Photonen als Informationsträger genutzt werden sollen. Zunächst wird eine Quelle von schmalbandigen Einzelphotonen vorgestellt. Diese Quelle basiert auf dem Konzept der parametrischen Fluoreszenz innerhalb eines optischen Resonators. Sie emittiert einen konstanten Strom von Photonenpaaren. Eines der beiden Photonen aus dem Paar kann detektiert werden, wodurch die Existenz des zweiten bestimmt ist. Eine statistische Beschreibung dieser Photonenpaare wird vorgestellt und erstmals direkt gemessen. Eine starke nichtklassische Korrelation der beiden Photonen in jedem Paar kann gezeigt und der Einzelphotonencharakter nachgewiesen werden. Um Emission in nur eine einzelne Mode zu erreichen, wurde der Photonenstrom mit Hilfe eines speziell entwickelten Mehrpass-Fabry-Pérot-Etalons gefiltert. Dieser Filter hat einen Durchlassbereich von nur 165 MHz Breite und 65% Transmission und eine Unterdrückung von 46 dB für nicht resonante Moden. Er kann vielfältig genutzt werden, beispielsweise um Quanteninformation tragende Photonen aus einem Rauschhintergrund zu extrahieren. Eine potentielle Anwendung in weltraumbasierten langreichweitigen Quantenkryptographieexperimenten wird vorgestellt. Photon-Atom-Wechselwirkungen werden im zweiten Teil der Arbeit gezeigt. Der Effekt der elektromagnetisch induzierten Transparenz (EIT) wird vorgestellt und experimentell demonstriert. Die ersten EIT Experimente in Cäsiumgaszellen bei Raumtemperatur mit Probepulsen, die nur ein einzelnes Photon enthalten, werden gezeigt. Außerdem wird Amplitudenmodulation eines einzelnen Photons demonstriert. Schließlich zeigt ein umfassender Ausblick wie die entwickelten experimentellen Bausteine erweitert werden können, um Einzelphotonenspeicherung zu erlauben und die Technologie für Quantenrepeater zu demonstrieren.

Abstract

The use of quantum mechanical properties for information processing, the so-called *quantum information processing* (QIP) has become an increasingly popular research field in the last two decades. It turned out that single photons are the most reliable long distance carriers of quantum information, e.g., tools to connect different processing nodes in QIP. While several methods exist to produce single photons, only little research has been performed so far on *narrow-band* single photons with spectral bandwidths in the MHz regime. Such photons are, however, of particular importance when coupling of single photons to atomic systems, which are often used in QIP as processing nodes, shall be realized. This thesis covers several research aspects on narrow-band single photons, all of which are important if such photons should be used as quantum information carriers. At first, a source for narrow-band single photons is introduced. This source is based on the concept of parametric down-conversion inside an optical resonator. It emits a constant stream of photon pairs. One of the two photons from the pair can be detected heralding the presence of the other photon. A statistical description of these photon pairs is introduced and for the first time also directly measured. A strong non-classical correlation of the two photons in each pair is shown and single-photon character is proven. In order to reach single-mode single-photon emission, the stream of photons was filtered with a specifically developed multi-pass Fabry-Pérot etalon. This filter has a passband FWHM of only 165 MHz and 65% transmission and a suppression of off-resonant light by 46 dB. It can be widely used, e.g., to extract quantum information carrying photons out of a background of noise photons. A potential use in the field of space-based long range quantum cryptography experiments is motivated. Photon-atom interactions are shown in the second part of the thesis. The effect of electromagnetically induced transparency (EIT) is introduced and experimentally demonstrated. The first EIT experiments in cesium gas cells at room temperature with a probe pulse containing only a single photon are described. Also, single-photon pulses are amplitude-modulated. Finally, a comprehensive outlook shows how the developed experimental building blocks can be extended in order to show single photon storage and demonstrate quantum repeater technology.

Contents

1. Introduction

In 1965, less than 20 years after the invention of the transistor, G.E. Moore formulated what later became the famous Moore's law [1]. Originally, he found that for minimum component costs the complexity of an integrated circuit doubles approximately every year. Today's definition states, the number of transistors in an integrated circuit doubles about every 18 months. Although the 'law' prevailed and is basically effectual since 50 years, it is clear that it cannot be valid forever. At present, it is expected to persist for only another 10 to 15 years. Even though the predictions of an early end of Moore's law are almost as old as the law itself, at some point there will be more than engineering problems preventing further development, namely when fundamental physical limitations will be reached, e.g., when structure sizes approach the size of individual atoms. Hence, in order to make further growth of computational power possible one has to search for completely new ways of performing information processing.

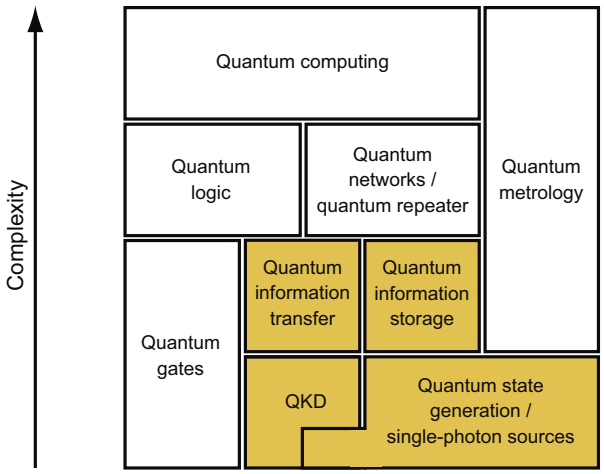

Figure 1.1.: Simplified overview of the field of quantum information processing (QIP). Today, research is mostly focused on the fundamental building blocks in the lower rows, however, first small applications of quantum logic have been demonstrated already and some are even on their way into commercial products. In addition, several groups worldwide aim at building a quantum repeater, which would strongly expand the possibilities of quantum information transfer. The work in this thesis is related to the colored areas.

The development of so-called *quantum information processing* (QIP) started in the 1980s, when fundamental concepts of quantum mechanics were applied to information theory [2]. QIP was found to enable the efficient implementation of algorithms, which

show exponential scaling if implemented using today's classical techniques, like searching unordered databases [3] or factoring [4]. This might eventually pave the way to overcome physical limits of classical computation technology, because QIP promises to solve complex problems that are not efficiently solvable by any classical computing system, due to exponentially increasing demand of computing power with the degree of complexity. Such problems arise across a broad spectrum of application categories, including quantum simulation, bioinformatics, artificial intelligence, cryptanalysis, routing, and logistics. Although QIP is in general still very far from solving real-life problems, it is today a rather versatile research field, as shown in figure 1.1.

Unlike classical information processing QIP is no longer based on bits as basic information unit, but on so-called quantum bits or *qubits*, which are arbitrary states of a two-dimensional Hilbert space spanned by two basis states. For example, a two-level atom can represent a qubit. Several concepts exist to represent qubits technologically. One usually distinguishes qubits for transmission of quantum information, so-called *flying qubits*, and processing nodes consisting of *stationary qubits*. While the race for the best technology option for stationary qubits is still open ranging from single atoms [5, 6] or ions [7–9], quantum dots [10, 11], defect centers in diamond [12] to Josephson qubits [13, 14], single photons, due to their weak coupling to the environment, are generally regarded as the most reliable long distance quantum information carrier, i.e., flying qubit.

One long-term goal in QIP is to interconnect many stationary qubits by flying qubits to a scalable and efficient *quantum network* [15–18]. Although this is still far from realization, flying qubits alone have made it into commercial products already: In 1984 Bennett and Brassard proposed a protocol for secret key distribution [19] that uses the single-particle character of a photon to avoid any possibility of eavesdropping on an encoded message (for a review see [20]). This so-called *quantum key distribution* (QKD) is today a large research field, and QKD based products for computer network encryption are commercially available.

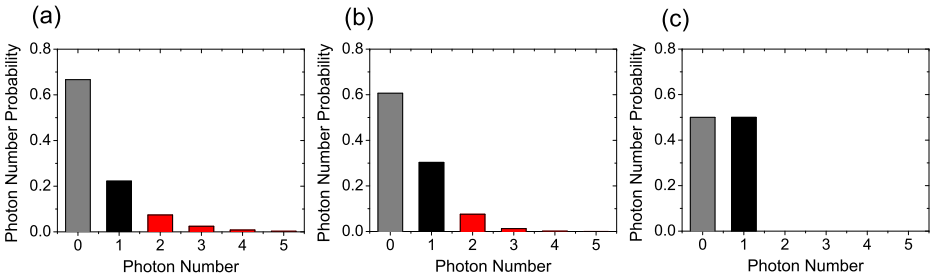

Figure 1.2.: Photon number distributions of (a) thermal light, (b) a coherent state as emitted by a laser well above threshold, and (c) a single-photon source, each with a mean photon number $\bar{n} = 0.5$. The red bars show unwanted higher number photon states.

Working with single photons in QIP generally requires the reliable deterministic generation of single- or few-photon states. However, due to their bosonic character photons tend to appear in bunches. Thus, the photon number distribution of classical light sources, i.e., thermal or laser light, is far from being ideal for QIP and in particular for QKD applications, as shown in figures 1.2(a) and (b). In QKD this characteristic in principle restrains the use of such sources, since an eavesdropper may gain partial information by a photon number splitting attack [21]. Adequate security can be achieved only if extremely weak light pulses containing on average just $\mu < 1$ photons are used. It can be shown [22], that for unconditional security of a QKD implementation using attenuated laser pulses, $\mu \sim t$ is required, where t is the transmittivity of the quantum channel, hence, the larger the losses, the more attenuated must the laser be. Accordingly, in practical implementations $\mu \ll 1$ is necessary. Alternatively, a more complicated protocol named decoy state protocol [23] can be introduced, which selectively modulates the pulse intensity. Similar obstacles occur for linear optics quantum computation (LOQC) [24], where photonic quantum gates [25], *quantum repeaters* [26], and *quantum teleportation* [27] require the preparation of single- or few-photon states *on demand* in order to obtain reliability and high efficiency. An ideal single-photon source for all of these applications would emit a sub-Poissonian photon number distribution with exactly one photon at a time. While due to inevitable scattering and absorption losses such a source is not possible, a typical photon number distribution of a real single-photon source is shown in figure 1.2(c) [28].

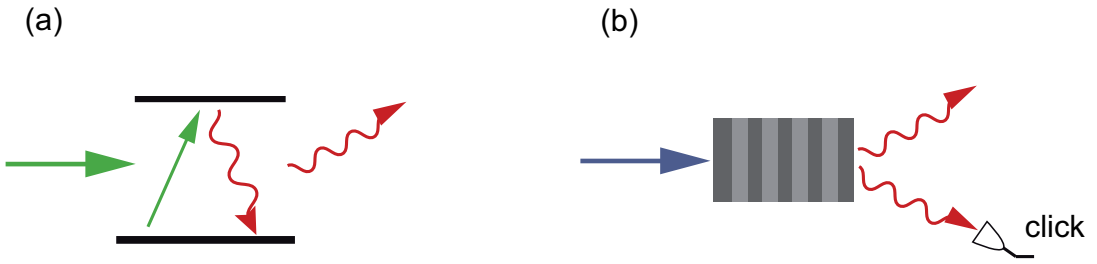

Figure 1.3.: Illustration of two relevant processes for single-photon generation: (a) spontaneous decay of a single isolated two-level system, (b) heralded single-photon generation by spontaneous parametric down-conversion inside a nonlinear medium.

Several promising experimental realizations of single-photon sources exist. Most of them rely on the isolated operation of a single two-level system that delays consecutive photon emission events by the finite time interval of a re-excitation process [29], as shown in figure 1.3(a). Possible are single atoms [5] or ions, which can be trapped and coupled to optical resonators to obtain single-mode emission [30, 31] and to increase the collection efficiency. Single molecules and nanocrystals [32–34] can also be used, however, a drawback is their susceptibility to photobleaching and blinking [35, 36]. Stable alternatives are nitrogen-vacancy defect centers in diamond [37, 38] and to some extend quantum dots [10]. A disadvantage of all these systems is the experimentalist's weak

control of the properties of the generated photons, i.e., wavelength or spectral bandwidth. Usually, these properties are largely determined by the intrinsic properties of the particular system used.

These limitations can be overcome by using a photon source based on the process of spontaneous parametric down-conversion (SPDC). Here, a pair of photons, referred to as *signal* and *idler* photon, is generated from a pump photon of shorter wavelength [39–41], as shown in figure 1.3(b). Signal and idler photons are generated simultaneously [42] and can be correlated in multiple degrees of freedom, like polarization, phase or frequency, which allows to generate entangled photon pairs [43]. By detecting the heralding idler photon the existence of the signal photon in the second channel is announced, which allows to use a SPDC source to approximate a single-photon source. Such a process can take place in a medium with nonzero second-order susceptibility. The properties of the generated photons are determined by energy conservation and phase matching and therefore can be controlled to a large extent. Due to improved fabrication techniques for nonlinear crystals SPDC has become a standard tool of quantum optics. In chapter 2 the concepts of single-photon statistics will be presented together with details about single-photon sources and measurements of photon statistics.

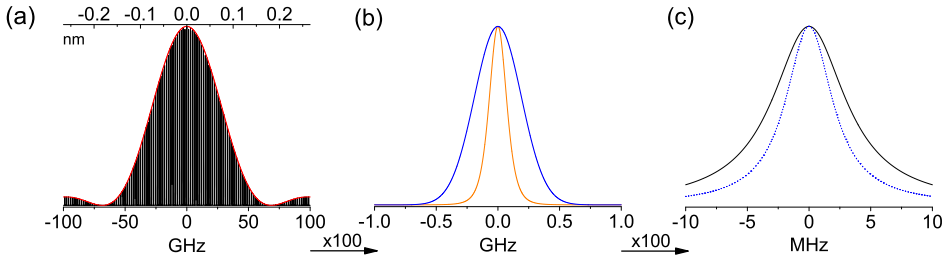

Figure 1.4.: Overview of the spectral bandwidth of several processes relevant for this work. It ranges from a bandwidth of a few 0.1 nm down to the regime of 10^{-5} nm, the x-scale is enlarged 100 times from (a) to (b) to (c), respectively. (a) shows the envelope that encloses the full spectral bandwidth of all modes produced by the down-conversion process (red) and the cavity-shaped single photons (black); (b) shows the filter bandwidth (orange) and the Doppler-broadened linewidth of the atomic system (blue); (c) displays a zoom-in into the spectral bandwidth of a single photon (black) and the natural linewidth of the atomic system (dotted blue). More details of the presented systems will be described later in the chapters 3, 4 and 5.

This thesis focuses on single photons of very narrow spectral bandwidth because of their considerable advantages if used as flying qubits. They can couple to atomic transitions, e.g., in a *quantum interface* between stationary and flying qubits. Furthermore, spectral filtering allows to extract such photons out of a background of noise photons,

e.g., in situations like free-space quantum communication [44–47]. In order to illustrate what is meant by *very narrow spectral bandwidth*, Figure 1.4 shows an overview of spectral bandwidths of different systems studied in this work, ranging down to the regime of 10^{-5} nm. From the available single-photon sources intrinsically only the single atom [30] or ion [48] based sources or such using a Λ-shaped atomic system in a magneto-optical trap [49] (MOT) are able to produce very narrow-band photons. However, such sources require single-atom/-ion traps or a MOT making them complex and not very reliable.

A promising alternative is a *cavity-enhanced* SPDC source, which allows to determine the parameters of the generated photons through the cavity. Down-conversion coherence times are usually ~ 100 fs, hence the generated photons have THz spectral bandwidth. However, by placing the medium in which down-conversion takes place inside an optical resonator, the generated photons' spectral bandwidth can be reduced by several orders of magnitude. This resonator configuration is usually termed *o*ptical parametric oscillator (OPO), and such a source is described in part I of this thesis. Additional spectral filtering of the OPO generated photons allows single-mode operation. OPOs far below threshold have been demonstrated by several research groups [50–53], the OPO used in this work was recently built in our lab [54–57]. The analysis of single-photon statistics of the OPO photons is demonstrated in chapter 3. An appropriate spectral filtering system based on a multi-pass Fabry-Pérot etalon is presented in chapter 4. Due to a sophisticated filter design, active stabilization and by pushing optical properties like surface flatness to the technological limit, the spectral filter has a peak transmission of 65% and a suppression of off-resonant light by 46 dB even though the transmitted and the filtered wavelengths have a frequency difference of $< 0.003\%$ with respect to their absolute wavelength. This filter is used in the preparation of single-mode photons right behind the source, as well as in extracting particular single-photons from a high intensity background. As also shown in chapter 4, other applications of the filtering technology are promising in fields where quantum information carrying photons need to be extracted from a noisy background, namely in long range free-space quantum key distribution.

In addition to single-photon sources, quantum interfaces between atomic and photonic systems are an important field of QIP research. Such an interface that allows to utilize the joint advantages of the two connected physical systems is also a prerequisite for most *quantum repeater* protocols [26]. Implementing a quantum repeater protocol could enable the distribution of quantum states over long distances, which is today strongly limited by photon loss, e.g., in optical fibers. Due to the no-cloning theorem [58, 59] straightforward amplification as in classical telecommunication is not an option in quantum communication. This could be overcome by creating long-distance entanglement [60] from shorter-distance entanglement via entanglement swapping. Such protocols require the capacity to create entanglement in a heralded fashion, to store it and to swap it [61], which is in principle possible by using atomic ensembles as quantum memories in combination with linear optical techniques and photon counting [62].

The transfer of photonic states onto atoms can be realized by the coherent process of *electromagnetically induced transparency* (EIT) [63, 64], as described in part II of this thesis. This part starts with the realization of EIT in cesium, shown in chapter 5. Beyond slow group velocities of light pulses using static EIT, light can be brought to a

complete halt, a technique called dynamic EIT, which can theoretically be explained by the concept of *d*ark-state polaritons as introduced by Fleischhauer and Lukin [65, 66]. Dynamic EIT can be extended to non-classical states [67], and single-photon statistics is preserved during storage [68]. In 2005, single photons have been stored in atomic ensembles for the first time [69, 70]. However, in existing single photon EIT experiments single-photon sources, being based on an atomic system themselves, were used to avoid bandwidth conflicts. The application of a completely different photon source, e.g., based on cavity-enhanced SPDC, would be a purely optical approach and allows the combination of different physical systems capable of QIP. This represents a major step towards the development of larger qubit systems and is therefore strongly aspired. As an important step towards this goal the first single-photon EIT experiments in cesium are presented in chapter 6. While single-photon EIT in rubidium atoms has been shown already [71, 72], cesium offers certain advantages, e.g., the $F = 3 \rightarrow F = 4$ hyperfine ground state clock transition, allowing the realization of all optical atomic clocks [73]. Moreover, the used ^{133}Cs D1-line at $894\,nm$ lies well within the wavelength regime of exciton emission from InAs quantum dots [74], which is relevant for possible coherent interfaces between atomic and solid-state systems [75] in the future. Recently, Reim et al. [76] demonstrated coherent storage and retrieval of sub-nanosecond low-intensity (several thousand photons) light pulses with spectral bandwidths exceeding $1\,GHz$ utilizing a far off-resonant two-photon Raman transition. In this experiment cesium provided the advantage of smaller Doppler linewidth, i.e., $\sim$ 380 MHz in ^{133}Cs compared to $\sim$ 540 MHz in ^{87}Rb at room temperature and larger hyperfine splitting of 9.2 GHz and 6.8 GHz, respectively. The latter sets a limit to the maximum storage bandwidth. In spite of the potential advantages there have been no experiments on the single photon level with cesium ensembles, for the most part because of the problem to filter the strong coupling beam. This problem could be overcome by the multi-pass Fabry-Pérot etalon presented in chapter 4.

In this thesis several important building blocks for an aspired full experimental setup for single photon storage are studied. A schematic of the setup is shown in figure 1.5 together with its association with the field of QIP. The setup can be regarded as *quantum memory* which will be mandatory for quantum network synchronization as well as for information processing purposes [77–79]; several groups in the world work on these kinds of experiments [80]. From now on, the term *single photon storage experiment* will be used to name the envisioned fully developed experiment.

While the whole single photon storage experiment is a work in progress, very important milestones have now been reached already and are described in this thesis. These include the first single-photon EIT measurements in cesium in gas cells at room temperature as well as a comprehensive study of the properties of the heralded single photons produced by the OPO. In addition, much know-how was developed and important building blocks of the experimental setup were fully completed, including a phase-locked laser system and the outstanding spectral filtering. Chapter 8 presents an outlook on the next development steps and new ideas to solve the remaining problems that prevent single photon storage at the moment, namely anti-Stokes noise and limited precision of the central wavelength of the OPO photons. The most important step will be the implementation

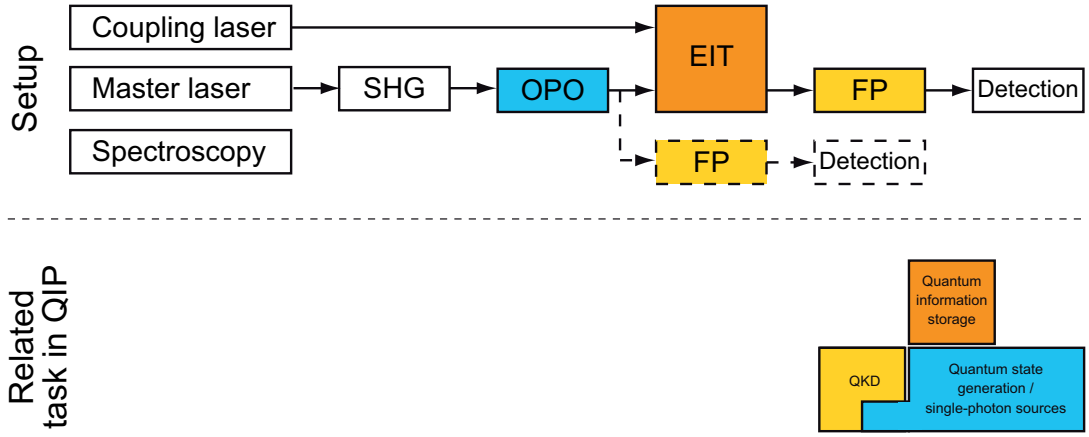

Figure 1.5.: Overview of the experiments described in this thesis together with their relation (colored) to QIP. The master laser is frequency-locked using a spectroscopy setup. Its light is frequency doubled using second harmonic generation (SHG) and pumps the OPO. Subsequently, the OPO photons are filtered by the multi-pass etalon (FP) and then used in an EIT setup. Behind the EIT setup another filter suppresses the coupling beam in order to allow the detection of single photons. Details of the specific building blocks will be presented in subsequent chapters.

of a Raman type memory [76] instead of the EIT based memory. As the overall concept is already widely developed, the realization of the remaining parts and increments of the single photon storage experiment can be envisioned for the near future.

List of experimental configurations

Within the sections of this thesis the following experimental configurations will be discussed in order to study different aspects of the single photon storage experiment. All configurations represent parts of the full experimental setup shown in figure 1.5, in the indicated section the yellow parts of the respective figure are presented in detail. The greyed parts are not used in the particular configuration.

Section 3.2

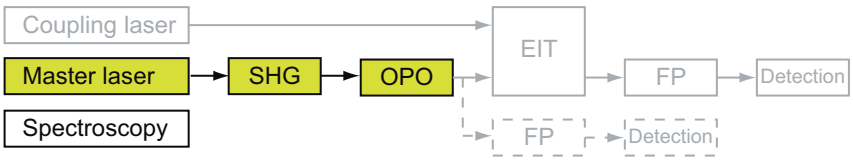

Experimental setup for down-conversion in a double resonant OPO.

Section 3.2.1

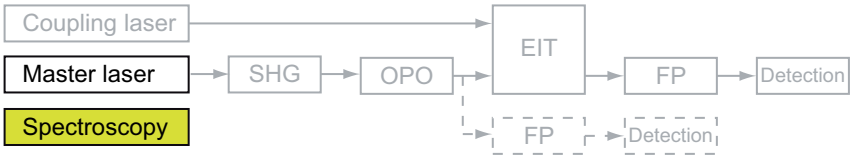

Experimental setup for frequency stabilization of the master laser.

Section 3.4

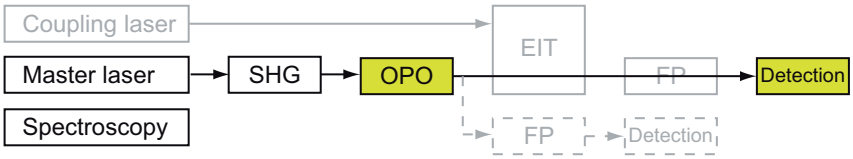

Experimental setup for the direct measurement of combined signal- and idler-photon statistics.

Section 4.1.1

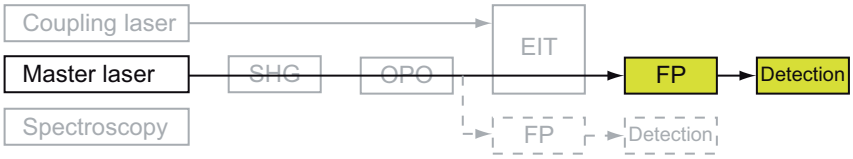

Experimental setup used to verify the multi-pass etalon performance.

Section 4.2

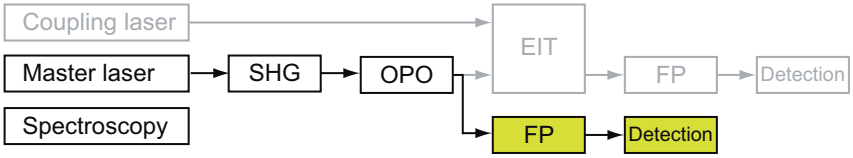

Experimental setup for single-mode operation of the OPO.

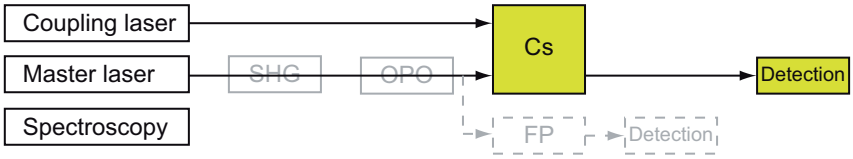

Experimental setup for Doppler-free saturation absorption spectroscopy.

Section 5.3

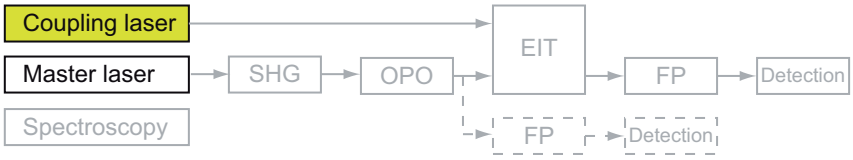

Experimental setup used to lock the coupling laser to the master laser.

Section 5.4

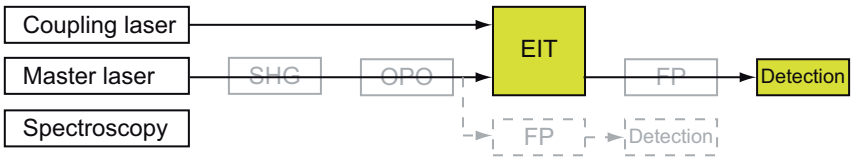

Experimental setup for first EIT measurements.

Section 6.1

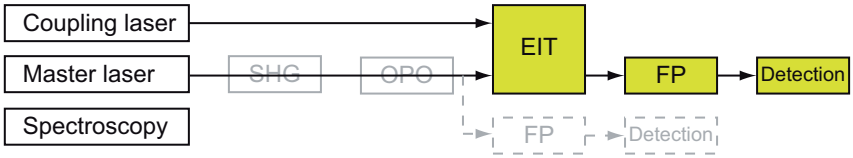

Experimental setup for EIT experiments with a probe beam on the single photon level.

Section 6.2

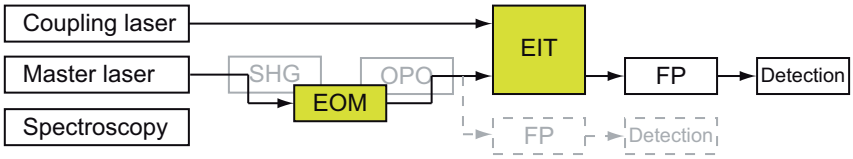

Experimental setup for EIT experiments with probe laser pulses containing only a single photon.

Part I.

Ultranarrow Bandwidth Single Photons

2. Single-Photon Sources and their Characteristics

The introductory chapter gave a broad overview of the field of QIP, some of its experimental challenges and the outline of a single photon storage experiment.

This chapter provides the basis for a more detailed understanding of single photons and their applicability in the field of QIP. An introduction into single-photon statistics as well as single-photon generation and detection will be given **(2.1)**. Additionally, new results are shown, namely the first measurement of single-photon statistics using only a single detector **(2.2)**.

2.1. Single-photon statistics

As pointed out in chapter 1, single photons are crucial for QIP as carriers of quantum information, especially if quantum information needs to be transported between distant nodes of a quantum network via flying qubits. In order to characterize the quantum nature of a particular stream of single photons, their statistics can be analyzed. This in turn allows to categorize single-photon sources with regard to their quality and appropriateness for a specific task.

2.1.1. Correlation functions

In order to gain insight into the photon statistics of a particular source, the emitted field's correlation function has to be regarded. Most important are the first- and second-order correlation functions, which compute coincidences between field amplitudes and intensities, respectively. While the first-order correlation function typically appears in interference experiments, it is not a proper figure of merit to distinguish between the classical or the quantum nature of a light source, an objective that has been the subject of a famous experiment by Taylor already in 1909 [81]. This arises from the fact that there may be no differences between the classical and the quantum predictions in the first-order correlations if the spectral properties of the fields are identical. However, the second-order correlation function is an adequate description. It describes how a certain mode of the electric field is correlated with itself, why it is often termed *auto-correlation* function. After normalization it takes the form [82]

$$g^{(2)}(t,t') = \frac{\langle a^\dagger(t)a^\dagger(t')a(t)a(t')\rangle}{\langle a^\dagger(t)a(t)\rangle\langle a^\dagger(t')a(t')\rangle} = \frac{\langle :I(t)I(t'):\rangle}{\langle I(t)\rangle\langle I(t')\rangle}\,, \tag{2.1}$$

where $a^\dagger$ and a are the creation and annihilation operators of an excitation (photon) in a single mode of the field. In the definition :: denotes normal ordering, meaning all destruction operators are on the right and all creation operators on the left. $I(t) \sim a^\dagger(t)a(t)$ is the time-dependent intensity operator of mode a. The $g^{(2)}$ function describes the degree of correlation between photons emitted at different times t and t' as a function of the temporal separation $\tau = t' - t$ and can be easily calculated from time-resolved photon counting events. In the special case of a stationary single-mode field the equation simplifies to

$$g^{(2)}(\tau) = \frac{\langle : I(\tau)I(0) : \rangle}{\langle I(0) \rangle^2} . \tag{2.2}$$

Plotting $g^{(2)}(\tau)$ immediately reveals the characteristic of a particular source, as shown exemplarily in figure 2.1.

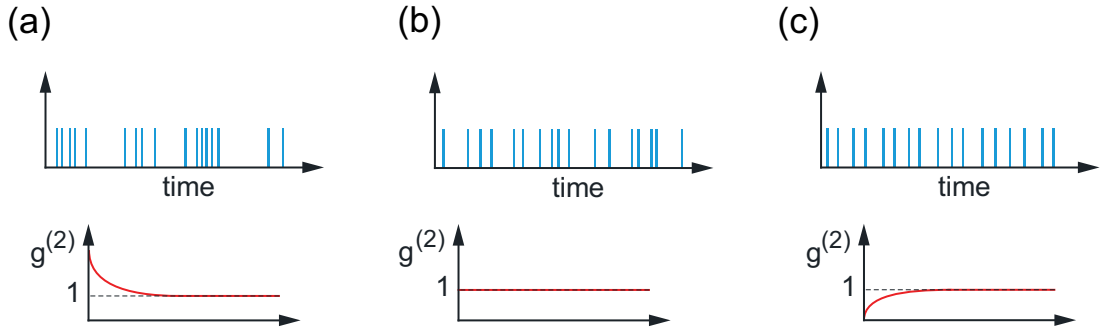

Figure 2.1.: Illustration of photon counting events (top) and corresponding second-order correlation functions $g^{(2)}(\tau)$ (bottom). (a) for a classical chaotic state (e.g. light bulb), (b) in case of coherent light (laser), (c) for a single-photon source (such as sketched in figure 1.3).

Figure 2.1 shows exemplary $g^{(2)}(\tau)$ functions for different states of light produced by different light sources. Classically chaotic states or thermal states, e.g., emitted from a light bulb, show an enhancement in the second-order correlation function near $\tau = 0$. The Cauchy-Schwartz inequality demands $g^{(2)}(\tau) \leq g^{(2)}(0)$ for all τ. Since classical probability distributions of the electric field are positive definite, it can also be shown that $g^{(2)}(0) > 1$, thus $g^{(2)}(\tau) \geq 1$, the source shows bunching behavior. Laser light well above threshold exhibiting Poissonian photon statistics has a flat correlation function $g^{(2)}(\tau) = 1$ for all τ. A single-mode quantum field with photon number variance $V(n) = \langle (a^\dagger a)^2 \rangle - \langle a^\dagger a \rangle^2$ and mean photon number $\bar{n}$ is described by

$$g^{(2)}(0) = 1 + \frac{V(n) - \bar{n}}{\bar{n}^2}. \tag{2.3}$$

For a Fock state, which is an eigenstate of the photon number operator $\hat{n} = a^\dagger a$, $g^{(2)}(0) = 1 - 1/n$ follows. Accordingly, a natural criterion for a single-photon source is to show an *antibunching* dip of $g^{(2)}(0) < 1/2$ [83].

While the calculation of $g^{(2)}(\tau)$ only requires a stream of time-resolved photon counting events, this data is not always easy to measure due to the limited temporal resolution of single-photon detectors. In particular, the widely used single-photon avalanche photo diodes (APDs) have significant dead times of up to $t_{DT} = 50$ ns after detecting a photon. This is due to their operation in Geiger mode, where a very high reverse voltage above the APD's breakdown voltage is used in order to reach a gain of $> 10^5$ through avalanche multiplication. Due to the high voltage, the APD needs to have its signal current actively limited, and the dead time occurs while the reverse voltage is built up again after a photon was detected. To measure correlations for $\tau < t_{DT}$ a so-called Hanbury Brown and Twiss (HBT) setup [84] is generally utilized. Two APD modules detect the light behind the output ports of a 50:50 beam splitter, as shown in figure 2.2 (a). The detection of a photon at APD 1 starts a coincidence counter, which keeps running until APD 2 receives a click. An electronic delay can be used to shift the time origin in order to enable the observation of asymmetric cross-correlation functions. The measured time intervals are then stored and binned in a histogram, as shown exemplarily in figure 2.2 (b).

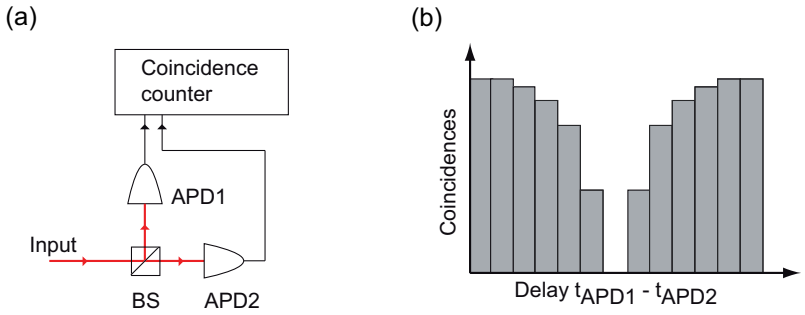

Figure 2.2.: (a) Hanbury Brown and Twiss setup, including a 50 : 50 beam splitter (BS) and start- and stop-APDs (APD1, APD2). (b) Photon count coincidences are binned in a histogram.

An ideal single-photon source will never emit two photons per time interval. Therefore, the probability of a start and a stop detector click with zero time interval in between approaches zero, as shown in figure 2.2 (b). Relating to the time constant of the underlying physical process the probability of detecting a second (stop) photon approaches 1 for long times after detecting the first (start) photon. Even though the experimental HBT measurement differs from the original second-order correlation function $g^{(2)}(\tau)$, it can be generally regarded as a good approximation. A detailed analysis of the relationship between the theoretical $g^{(2)}$ function and the experimentally observed function can be found in reference [85].

2.1.2. A single-photon source based on diamond

Among the various options for single-photon sources – several of them have been mentioned in chapter 1 – the sources based on nitrogen-vacancy (NV) centers in diamonds

are promising [37, 38], in particular, because the experimental setup required to use an NV center as single-photon source is simple and reliable and because the NV center represents a photostable emitter in the visible wavelength range operating even at room temperature. An NV center is a point defect in the diamond lattice, where a nitrogen atom replaces two neighboring carbon atoms, as shown in figure 2.3 (a). Although the NV defect center can be located in a bulk diamond, it behaves like an isolated single atom. This intrinsically leads to the emission of single photons, as any photon emission needs a preceding excitation and is determined by the radiative lifetime. The only requirement for single-photon emission is an efficient isolation of a single NV center in the bulk, e.g., by spatial filtering or by using very small (nano) diamonds which contain a single NV center only. NV centers in diamond can occur in two different charge configurations, either neutral (NV^0) or negatively charged (NV^-), the latter will be studied here. The electronic structure of the NV^- center is reasonably understood [86]. A simplified common model of the energy level schema is shown in figure 2.3 (b)

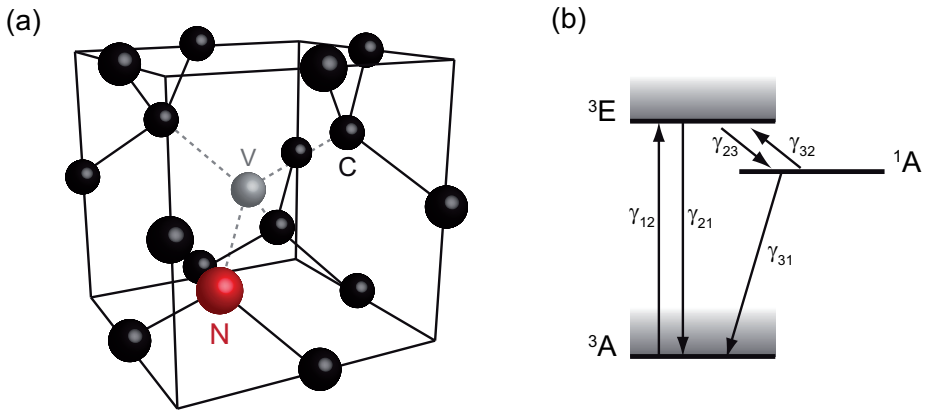

Figure 2.3.: (a) Schematic representation of the atomic structure of the NV defect center, comprising one missing carbon atom (C), i.e., the vacancy (V) and an adjacent substitutional nitrogen atom (N). (b) Energy level schema of the NV^- center. ^{3}A and ^{3}E are the triplet ground and excited state, respectively, and ^{1}A is a metastable singlet state. The grey shaded areas represent the vibronic level structure of the states ^{3}A and ^{3}E.

The NV^- center has a triplet ground and excited state, ^{3}A and ^{3}E, respectively, the particular energetic splitting of the sublevels is caused by spin-spin interactions [87] and, in case of the excited state ^{3}E, also by spin-orbit coupling [88]. The metastable singlet state ^{1}A in between ^{3}A and ^{3}E is strongly suggested by experimental evidence. The transition $^3\text{A}\leftrightarrow{}^3\text{E}$ is associated with a zero phonon absorption/emission line at 637 nm, into which at room temperature around 5% of the light is emitted [89]. The rest goes into phonon sidebands resulting from transitions into higher vibronic levels of the ground and excited state. In bulk diamond the radiative lifetime of the excited state ^{3}E is found to be ≈ 12 ns. A drawback of the NV^- center is, that the frequency of the optical absorption line slightly varies from center to center and that only a small amount of light is emitted

in the Fourier-limited zero phonon line. Today, even commercial products employing NV^- centers as single-photon source are available.

Based on the discussion in section 2.1, it is illustrative to study the single-photon statistics of photons emitted by a single NV^- center. As pointed out, $g^{(2)}(\tau)$ is the relevant parameter to study. It can be analytically obtained from the rate equations, which describe the transitions in the NV^- center. These are

$$\begin{aligned}
\frac{\partial \varrho_1(t)}{\partial t} &= -\gamma_{12}\varrho_1(t) + \gamma_{21}\varrho_2(t) + \gamma_{31}\varrho_3(t) \\
\frac{\partial \varrho_2(t)}{\partial t} &= \gamma_{12}\varrho_1(t) - (\gamma_{21} + \gamma_{23})\varrho_2(t) + \gamma_{32}\varrho_3(t) \\
\frac{\partial \varrho_3(t)}{\partial t} &= \gamma_{23}\varrho_2(t) - (\gamma_{31} + \gamma_{32})\varrho_3(t)\,.
\end{aligned} \tag{2.4}$$

ϱ_1, ϱ_2, ϱ_3 are the populations of the energy levels ^{3}A, ^{3}E, ^{1}A, respectively. γ_{ij} are the corresponding transition rates between these levels, as shown in figure 2.3 (b). With the initial conditions $\varrho_1 = 1$, $\varrho_2 = 0$, $\varrho_3 = 0$ the population of the ^3E excited state ϱ_2 can be obtained. It is directly proportional to the photon emission probability, hence, the second-order auto-correlation function was found to be [90]

$$g^{(2)}(\tau) = \frac{\varrho_2(\tau)}{\varrho_2(\tau \to \infty)} = 1 + Ce^{-\Gamma_2\tau} - (C+1)e^{-\Gamma_3\tau}\,, \tag{2.5}$$

with the coefficient and decay times defined as

$$\begin{aligned}
C &= \frac{\Gamma_3(\gamma_{31} + \gamma_{32} - \Gamma_2)}{(\gamma_{31} + \gamma_{32})(\Gamma_2 - \Gamma_3)} \\
\Gamma_{2,3} &= \frac{1}{2}\left(A \pm \sqrt{A^2 - 4B}\right)
\end{aligned} \tag{2.6}$$

and

$$\begin{aligned}
A &= \gamma_{12} + \gamma_{21} + \gamma_{23} + \gamma_{31} + \gamma_{32} \\
B &= \gamma_{12}(\gamma_{23} + \gamma_{31} + \gamma_{32}) + \gamma_{21}(\gamma_{31} + \gamma_{32}) + \gamma_{23}\gamma_{31}\,.
\end{aligned} \tag{2.7}$$

Based on equation 2.5 experimental data can be directly fitted, as will be shown below.

2.2. Single detector antibunching measurements

Compared to other single-photon sources, e.g., quantum dots, the radiative lifetime of an NV^- center of the order of nsec is quite long. In order to study the single-photon statistics and proof antibunching, a moderate time resolution in the nsec-range is sufficient. This should open up the possibility to measure antibunching with a single detector only, i.e., without a HBT setup, given that a detector with a small dead time t_{DT} compared to the width of the antibunching dip in the $g^{(2)}(\tau)$ function is available. Such a measurement was performed using a superconducting single-photon detector

(SSPD) [91, 92]. SSPDs can be manufactured using NbN meander wire of $\sim$ 5nm thickness on a sapphire substrate, as shown in figure 2.4 (a). The detector is kept at a temperature far below the superconducting transition T_c and is biased with a current I close to the wire's critical current I_c. The detector relies on the principle that a photon is absorbed by a Cooper pair resulting in local suppression of superconductivity and formation of a hotspot, as shown in figure 2.4 (b). The hotspot rises and a resistive

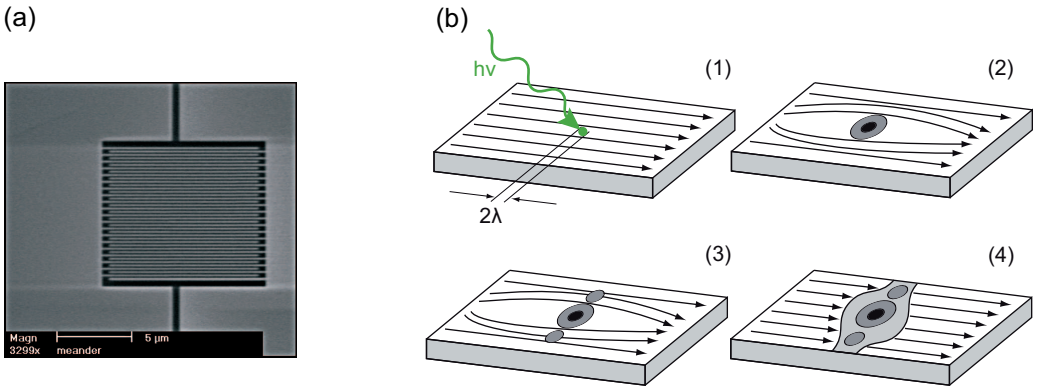

Figure 2.4.: (a) SEM image of a superconducting single-photon detector SSPD [93]. (b) Operation principle of an SSPD: A photon is absorbed by a Cooper pair (1) resulting in local suppression of superconductivity and formation of a hotspot (2). This rises (3) and a resistive barrier is established across the entire width of the wire (4) which causes a voltage signal that can be detected [92].

barrier is established across the entire width of the wire. This causes a voltage signal with an amplitude proportional to I that can be detected [92]. The SSPD offers a very low dark count rate ($\ll$ 1 Hz) and small timing jitter of approximately 20 ps, its $t_{DT} \approx 5$ ns. The experimental setup to perform antibunching measurements with a single SSPD is shown in figure 2.5.

The 514 nm line of an argon ion laser was used to excite an NV^- center in a nanodiamond through an oil immersion objective (NA 1.4), which also collects the emitted light. Spectral filters block the excitation light, a telescope and a pinhole establish a confocal configuration to reduce background light. More details on the setup for single-photon generation using an NV^- center can be found in reference [94]. The emitted single photons were coupled into a single-mode optical fiber and detected either using two APDs in HBT configuration or by an SSPD. The SSPD itself was directly coupled to the fiber and kept in liquid helium. When the SSPD was used, data recording was performed with a 1 GHz digital storage oscilloscope. The oscilloscope was programmed to sample a stream of measurements for 250 ns starting from the first trigger, i.e., the first detector pulse. If a second trigger occurred during the 250 ns, the data was stored on a hard disk. 30.000 of these data files were produced during several hours of measurements. The data files were analyzed in order to extract the peak distances, and from these values a histogram was produced. This is shown as blue curve in figure 2.6.

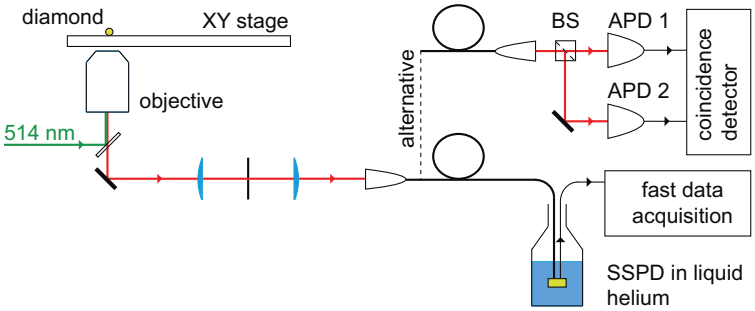

Figure 2.5.: Experimental setup for antibunching measurements on a single NV^- center in a nanodiamond. The nanodiamond can be moved above the objective using an xy-stage. Spectral filters (not shown) block the excitation light, and a telescope and a pinhole establish a confocal configuration to reduce background light. The emitted single photons are analyzed using two APDs in HBT configuration or by an SSPD, respectively.

The grey curve in figure 2.6 shows the conventional HBT measurement using two APDs and the same sample. Both curves perfectly overlap. The data was fitted using equation 2.5. This result shows for the first time that antibunching measurements with only one detector are possible if the detector's death time is short enough for the respective single-photon source.

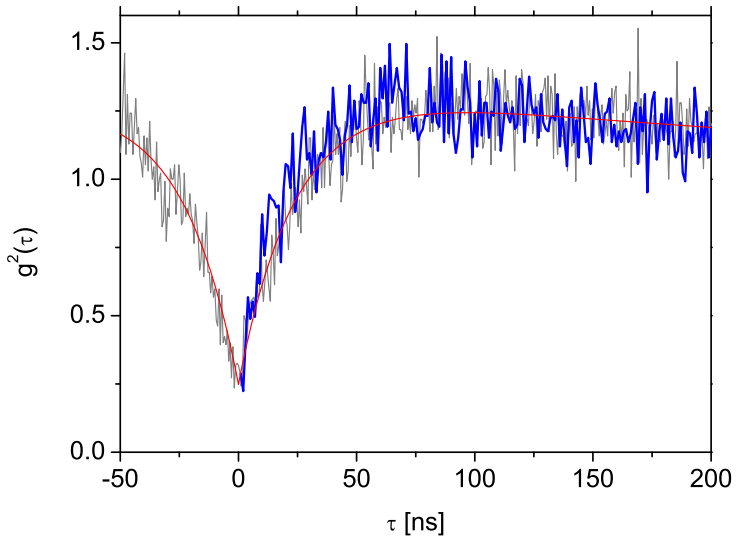

Figure 2.6.: $g^{(2)}$ measurement of a single NV^- center in a nanodiamond. The blue curve was measured using a single SSPD and the grey curve using a usual HBT setup with two APDs. The red line is a fit using equation 2.5.

While the HBT setup will be used further in this thesis to measure single-photon statistics, the above measurements are illustrative to show how the capability to measure single-photon statistics depends on the particular single-photon source and the available detectors. This relationship will be studied again in chapter 3, where the single-photon statistics of the source already built for the single photon storage experiment will be studied in detail.

3. Optical Parametric Oscillator as Heralded Single-Photon Source

Experiments with true single photons first of all require an appropriate photon source. While several experimental realizations of single-photon sources exist, most of them have the disadvantage that the experimentalist has only low control of the properties of the generated photons, i.e., wavelength or spectral bandwidth. In particular, if photons of ultranarrow spectral bandwidth are required, only sources based on atomic systems are intrinsically suitable. However, a photon source based on the process of spontaneous parametric down-conversion (SPDC) can overcome these limitations. Especially a cavity-enhanced SPDC source allows to determine the generated photon parameters through the cavity, thus making ultranarrow spectral linewidth possible. The use of such an optical parametric oscillator (OPO) as single-photon source has been demonstrated by several groups [50–53], the OPO utilized in this thesis was recently built in our group [54–57].

In this chapter, the concepts of parametric down-conversion inside a resonator **(3.1 and 3.2)** together with the underlying nonlinear processes and their experimental realization will be presented. Subsequently, an appropriate description of the photon statistics of a heralded source will be introduced **(3.3)**, which is a prerequisite for performing quantum information processing using such photons. Afterwards, the first direct measurements of heralded single-photon statistics from a parametric down-conversion source will be presented **(3.4)**. Finally, the OPO mode spectrum will be studied **(3.6)**.

Parts of this chapter (3.3 and 3.4) were published in *Direct measurement of heralded single-photon statistics from a parametric down-conversion source*, Phys. Rev. A **83**, 013802 (2011).

3.1. The concept of optical parametric oscillators

During the process of parametric down-conversion a pump photon incident on an appropriate nonlinear medium is split into two photons of lower frequency [41], called signal and idler. Signal and idler photons are generated simultaneously [42], thus, at a low pump rate, by detecting the heralding idler photon the existence of the signal photon in the second channel is announced, and event post-selection can be performed. As shown in figure 3.1, the properties of the generated photons are determined by energy conservation and phase matching and can therefore be controlled to a large extent. Moreover, the bandwidth of down-converted photons can be reduced by mode enhancement inside an optical resonator in order to match the linewidth of atomic transitions, e.g., for applications like quantum networks based on stationary atoms as information processing

nodes and single photons for information transmission.

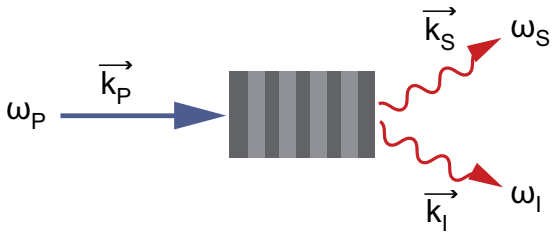

Figure 3.1.: Schematic of the down-conversion process in an appropriate nonlinear medium. A pump photon of frequency ω_p and wave vector $\vec{k_p}$ is split into signal and idler photons, which are described by ω_s, $\vec{k_s}$ and ω_i, $\vec{k_i}$.

In nonlinear interactions photons at a fundamental wavelength create photons at different wavelengths while obeying energy and momentum conservation. Following Maxwell's theory the propagation of an electromagnetic wave inside a dielectric medium induces a polarization $\vec{P}$. Its components can be expressed by a Taylor expansion with respect to the driving electric field $\vec{E}$

$$P_i = \epsilon_0 \left(\chi_{ij}^{(1)} E_j + \chi_{ijk}^{(2)} E_j \, E_k + \chi_{ijkl}^{(3)} E_j \, E_k \, E_l + \ldots \right) . \tag{3.1}$$

The coefficients $\chi^{(n)}$ are the n^{th} order susceptibilities, the second-order term involving $\chi^{(2)}$ is responsible for several frequency mixing processes like second harmonic generation (SHG) and spontaneous parametric down-conversion (SPDC). Secondary elementary waves are generated and can interfere to a macroscopic field if a proper phase relation between the fundamental wave and harmonics is ensured. This phase-matching, which is equivalent to momentum conservation, will be briefly studied below, a more comprehensive analysis can be found in reference [57]. In case of SHG the phase-mismatch between fundamental and harmonic wave

$$\Delta k = k_{2\omega} - 2k_\omega = \frac{2\omega}{c} \left(n_{2\omega} - n_\omega \right) \tag{3.2}$$

must be minimized, i.e., $n_\omega = n_{2\omega}$ is desired. Otherwise, a phase mismatch would lead to different phase velocities for fundamental and harmonic waves and limits efficient conversion to the coherence length. Although several crystal classes have non-vanishing $\chi^{(2)}$, the phase-matching condition limits the options to find an appropriate crystal material. In isotropic crystals normal dispersion demands $n_\omega < n_{2\omega}$, and anomalous dispersion is usually limited to high-absorption materials. However, there are several methods to adjust the relevant crystal parameters in order to achieve $n_\omega = n_{2\omega}$, namely birefringence in anisotropic crystals.

As shown in figure 3.2, phase-matching in such a crystal depends on the propagation direction of the light inside the crystal with respect to the crystal's orientation. By cutting the crystal in a particular angle relative to its optical axes the condition can be fulfilled. Additionally, if ordinary (n_o) and extraordinary (n^e) indices of refraction show

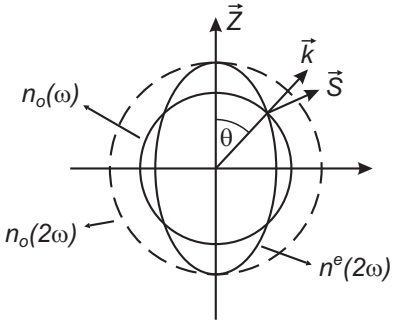

Figure 3.2.: SHG phase-matching. A negative uniaxial crystal shows a single distinguished spatial direction, the optical axis $\vec{Z}$. A polarization perpendicular to the principal plane, spanned by $\vec{Z}$ and the wave vector $\vec{k}$ of the fundamental wave, is called ordinary while in-plane polarization is referred to as extraordinary. The corresponding refractive indices $n_o(\omega)$ and $n^e(2\omega)$ must be equal along the propagation direction $\vec{k}$ in order to achieve efficient conversion. This is possible because only the refractive index of the extraordinary wave $n^e(2\omega)$ depends on the angle between $\vec{Z}$ and $\vec{k}$, hence the angle can be used to adjust phase-matching [57].

different dependencies on temperature, the crystal temperature may be used to change the indices of refraction in order to achieve phase-matching, i.e., the fundamental-wave ordinary index of refraction $n_o(\omega)$ must coincide with the harmonic-wave extraordinary index of refraction $n^e(2\omega)$.

Another possibility is the so-called *quasi-phase-matching*. Here, the sign of the susceptibility switches periodically, which can be achieved artificially by a pulsed electric field, electron bombardment, thermal pulsing, or other methods [95]. If periodic poling takes place at multiples of the coherence length, the build-up of a macroscopic polarization is no longer limited to distances on the order of the coherence length as in unmatched crystals, but a renewed build-up is initiated. The poling period for quasi-phase-matching of m^{th} order is given by

$$\Lambda_m = \frac{2\pi}{\Delta k}\,(2m-1)\ . \tag{3.3}$$

As the corresponding non-linearity d of this process is modified to

$$d_{eff} = \frac{2}{m\pi}\,d\,, \tag{3.4}$$

the crystal orientation with the highest initial nonlinearity d can be chosen before the periodic poling is applied. The crystals available today are mostly fabricated by ferroelectric domain engineering; one example is potassium titanyl phosphate (PPKTP), which is used in this experiment as shown below.

To increase the output power of frequency conversion setups, an optical resonator around the conversion crystal can be used. Especially for two-photon processes like

SHG, where the harmonic power shows a parabolic dependence on the fundamental power, this is advantageous. Depending on the particular application different resonator geometries can be realized. Bidirectional resonators, e.g., the Fabry-Pérot configuration, minimize the number of optical components and enhance the mechanical stability while unidirectional setups, like the bow-tie resonator, avoid back reflections into the pump laser source.

3.2. Narrow-band single photons from a double-resonant OPO

As shown in figure 3.3, the techniques of SHG and an OPO are used in the experimental setup for single-photon generation which is part of the single photon storage experiment.

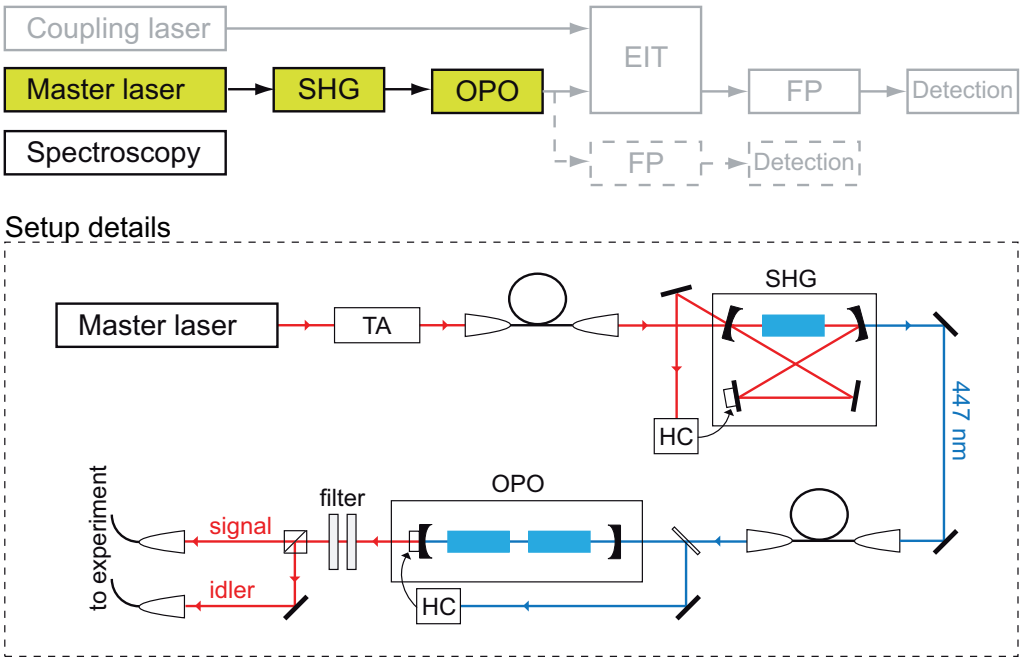

Figure 3.3.: Experimental setup for down-conversion in a double resonant OPO. The light from the master laser is amplified by a tapered amplifier (TA) and subsequently frequency-doubled to blue light at 447 nm using a non-linear crystal of $KNbO_3$ in a bow-tie cavity configuration (SHG). The cavity length is stabilized to the pump laser using the Hänsch-Couillaud method (HC) [96]. The SHG output is mode-cleaned by a single-mode fiber of 2 meters length and fed into the OPO cavity, as described in section 3.2.2. The OPO cavity is stabilized to the frequency-doubled light by the Hänsch-Couillaud method also. Signal and idler photons are filtered by several long-pass filters to suppress any remaining blue pump light and coupled into two different single-mode fibers.

The master laser is an external-cavity diode laser (Toptica Photonics DL100), which

uses a Littrow configuration [97, 98] to reach an intrinsic linewidth of a few 100 kHz and provides around 20 mW of single-mode output power. This laser is stabilized to a hyperfine transition of the cesium D1 line at about 894.3 nm (energy level schema is shown in figure 5.1) in order to present a stable frequency reference for the whole experiment, as shown below. In order to achieve a sufficient master laser power for the subsequent experiments, 17 mW of its emission are fed into a tapered amplifier that generates 250 mW output behind a single-mode fiber. The stabilized and amplified beam is fed into a bow-tie cavity including a non-linear crystal for SHG. The crystal was chosen on the basis of its non-linear coefficient. For SHG of a 894.3 nm fundamental wave $KNbO_3$ shows the best properties. The SHG produces a frequency-doubled blue beam at 447.15 nm with up to 7 mW power in a single TEM_{00} mode. The SHG cavity is stabilized using the Hänsch-Couillaud method [96] which does not need sideband generation. This method is applicable to resonators that show different finesse values for orthogonal polarizations, as it is the case in resonators with birefringent crystals like in this setup. The second harmonic shows a linewidth that is $\sqrt{2}$ times the fundamental value.

3.2.1. Laser frequency stabilization

In order to have a fixed wavelength reference for all lasers used in the single photon storage experiment, the master laser is frequency-stabilized by Doppler-free frequency modulation spectroscopy (FMS) [99, 100] to the $6^2S_{1/2}(F = 3) \rightarrow 6^2P_{1/2}(F' = 4)$ hyperfine transition in cesium (more details about the atomic system will be presented in chapter 5, the level schema can be found in figure 5.1). Compared to the pump-probe technique of saturation spectroscopy [101] the FMS allows an enhanced signal-to-noise ratio by taking advantage of lock-in detection on a phase-modulated probe beam. Figure 3.4 shows the experimental realization of the master laser stabilization. A small amount of the master laser power is split into pump and probe beams, and after phase modulation by an electro-optic modulator (EOM) the probe is superimposed with the counter-propagating orthogonally polarized pump inside a 7.5 cm long cell containing 99.99% pure ^{133}Cs. The cell windows are AR coated in order to avoid parasitic etalons. A dual-layer μ-metal shielding around the cell attenuates DC fields by a factor $\sim 4.5\times10^{-4}$, thus eliminating level shift through earth's magnetic field and splitting through stray fields. Lock-in detection of the probe modulation is performed by demodulation of the electronic signal at the local oscillator (LO) frequency that also drives the EOM, followed by a low-pass filter. A servo including proportional and integral filter stages creates appropriate control signals for diode current and the extended-cavity piezo. The frequency lock is stable for several hours and reduces the short-term linewidth of the probe laser to <50 kHz.

3.2.2. Experimental realization of the OPO

After spatial filtering by a single-mode fiber the blue light from the SHG is coupled into an optical parametric-oscillator (OPO) in double-resonant configuration [51, 102] aiming

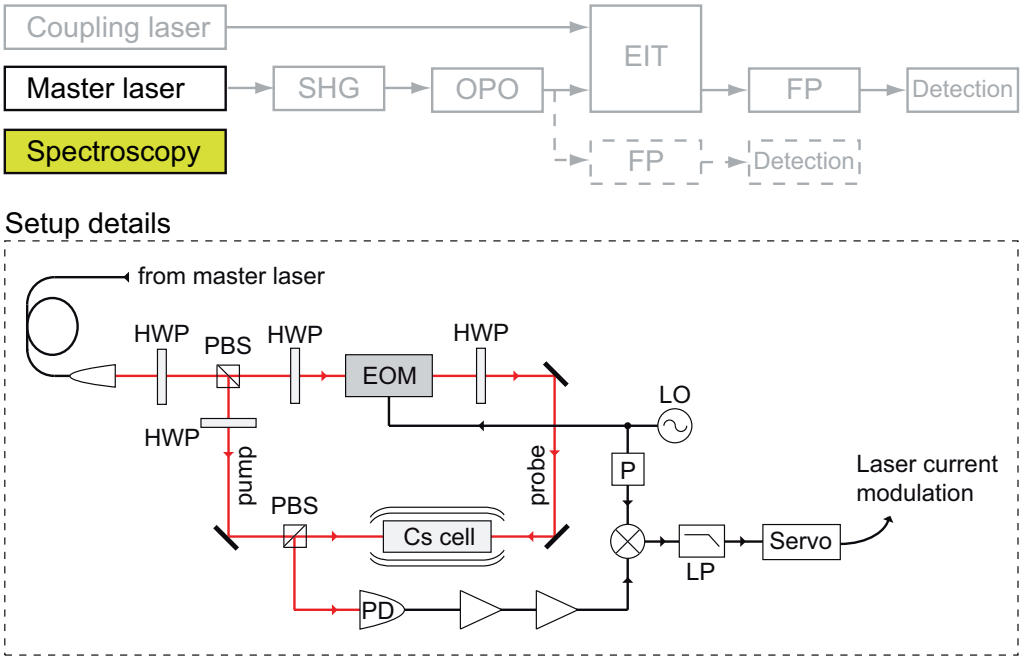

Figure 3.4.: Experimental setup for sub-Doppler frequency stabilization of the OPO master laser to a cesium hyperfine transition via frequency modulation spectroscopy. The laser to be stabilized is split into a pump and probe beam. The probe is phase-modulated by an EOM and is superimposed with the counter-propagating orthogonally polarized pump inside the Cs cell. Lock-in detection of the probe modulation is performed by demodulation of the electronic signal with the phase shifted (P) local oscillator (LO) signal that also drives the EOM, followed by a low-pass filter (LP). Through a servo electronic which modulates the laser current the feedback loop is closed.

at the enhancement of signal and idler and pump fields inside the resonator. Since signal and idler photons generated by frequency-degenerate parametric down-conversion can be separated by polarization only, a type-II process is required, i.e., signal and idler are orthogonally polarized after generation.

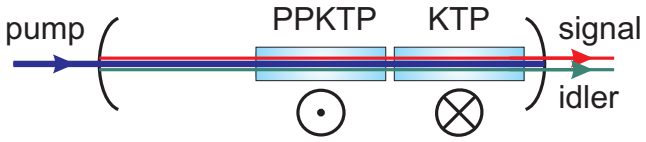

Figure 3.5.: Scheme of the double-resonant OPO using a type-II down-conversion process: A compensating unmatched KTP crystal, turned by 90°, accompanies the PPKTP crystal inside the resonator for equal FSR of signal and idler [57].

For negligible walk-off angle and collinear propagation of signal and idler fields along

the resonator symmetry axis, a periodically poled crystal needs to be selected. Potassium titanyl phosphate (KTP) provides the highest non-linear coefficient for down-conversion at the selected cesium D1 line (894.3 nm). However, KTP is a biaxial crystal, hence, the effective crystal lengths for orthogonally polarized signal and idler fields are different. To ensure simultaneous resonance [51], a second unmatched KTP crystal – turned by 90° – is integrated into the resonator next to the periodically-poled conversion crystal (PPKTP), as shown in figure 3.5.

The resonator is built in Fabry-Pérot configuration with curved mirrors. Incorporating intra-cavity pump losses, an input mirror reflectivity of ~ 0.48 for the pump wavelength ensures impedance matching with an expected resonator finesse $F_P^{th} = 4.2$. Thus, a pump power of 1 mW outside the resonator leads to 1.9 mW circulating power. In addition to this enhancement, the resonant pump allows length stabilization of the resonator, again the Hänsch-Couillaud method is used for stabilization. At signal and idler wavelengths the input mirror is highly reflective, and a finesse value of $F_{S/I}^{th} = 272$ is calculated for signal and idler with an output mirror reflectivity of 0.99. The effective cavity lengths for pump and signal/idler fields correspond to a free spectral range $\mathrm{FSR}_P \approx 1.45$ GHz and $\mathrm{FSR}_{S/I} \approx 1.50$ GHz for pump and signal/idler, respectively. This should yield a cavity bandwidth $\gamma_S = \gamma_I \approx 5.4$ MHz. Experimentally, a cavity bandwidth $\gamma_S = \gamma_I = 7.2$ MHz was found, as will be shown below. The discrepancy is probably caused by reduced mirror reflectivity or absorption.

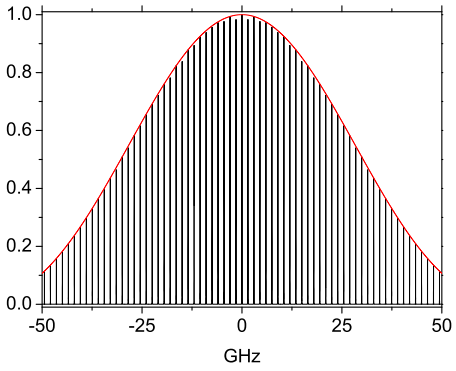

Figure 3.6.: Schematic plot of the normalized spectrum of the photons generated by parametric down-conversion inside the cavity. The broad spectrum of the down-conversion process (red) is modified by the cavity modes (black). The width of the Lorentzian peaks, i.e., the single-photon bandwidth, is determined by the cavity damping rate. The peaks are separated by the free spectral range (FSR).

The signal and idler linewidth FWHM $= \gamma_{S/I}\sqrt{\sqrt{2}-1} \approx 4.6$ MHz [54], the full OPO spectrum consists of a ~ 61 GHz wide phase-matching envelope with individual modes of 4.6 MHz FWHM in ~ 1.5 GHz intervals, as shown in figure 3.6. The OPO emits at a

rate of $\sim 1.4 \times 10^6$ biphotons/s per mW pump power. Such a high rate is only possible with the double-resonance-enhanced cavity design.

The OPO spectrum can be directly measured by studying the temporal cross-correlation between signal and idler modes, as shown in figure 3.7. Here, the temporal distance between the peaks corresponds to the cavity round trip time of ~ 700 ps, this will be further studied in section 3.6. The theoretical background and details about the setup used for the measurement in figure 3.7 can be found in reference [57]. The spectrum will be further studied in section 3.6. From the exponential decay of the correlation function depicted in figure 3.7 (a), cavity decay rates for signal and idler can be derived. They in turn translate into the single-photon bandwidth.

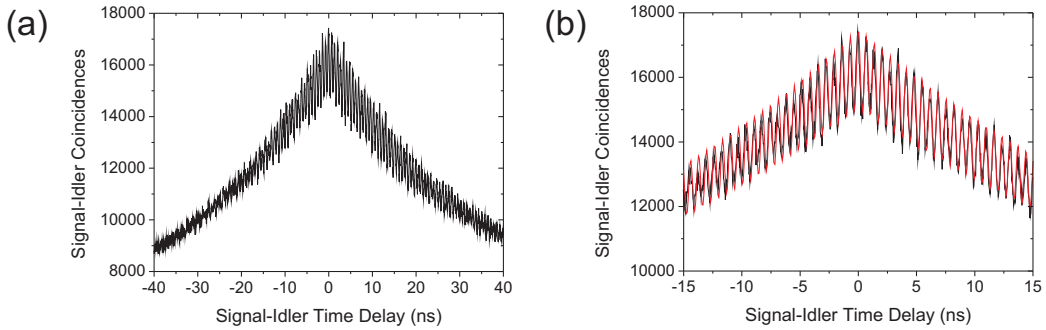

Figure 3.7.: (a) Temporal second-order cross-correlation function between signal and idler modes[1]. (b) Zoom into the region around 0 ns signal-idler time delay. The red dashed line follows a theoretical model presented in reference [57] which takes into account the time resolution of the correlation measurement setup of ~ 620 ps [57].

Corresponding to their narrow spectral bandwidth the signal and idler photons have a coherence time Δt of ~ 220 ns, i.e., the wave packet has a spatial length of ~ 66 meters in air.

3.3. Statistics of heralded single photons

Cavity enhanced down-conversion sources are in several aspects superior to other single-photon sources, namely because of the possible control of photon wavelength and spectral bandwidth together with the relative ease of use. However, an OPO is *not* an *intrinsic* single-photon source. Only its capability to generate two photons at the same time allows to post-select, e.g., signal photons on detection of a heralding idler photon. Hence, the photon statistics of the combined signal and idler output field and subsequently,

[1] This measurement was performed earlier than the other measurements presented in this thesis. The cavity bandwidth was lower at that time, it was derived from the exponential decays in this measurement and found to be ~ 4.4 MHz. For all other measurements, the cavity bandwidth was found to be 7.2 MHz. This is caused by a lower OPO cavity finesse due to slightly degraded mirrors.

after detection of one of the two photons the heralded single-photon statistics are very important and at the same time far less trivial than the photon statistics of an intrinsic single-photon source. Recent publications [103–105] have discussed the characterization of heralded SPDC-based photon sources with continuous-wave excitation, i.e., the source is driven by a cw pump beam (p) at wavelength ω_p and produces signal (s) and idler (i) beam at center frequencies ω_s and $\omega_i = \omega_p - \omega_s$, respectively. However, direct measurements of SPDC photon statistics under cw excitation in the single-photon regime are difficult, due to the fact that detector jitter τ_d is usually far larger than the signal coherence time Δt determined by the spectral width of the generated photons, typically being in the several 100 GHz regime, i.e., $\Delta t \approx 0.1..1$ ps. In particular, triple-coincidence rates between idler and two signal photons, could not be resolved appropriately. In particular the peculiar difference between antibunching in a single-photon source based on spontaneous emission of a two-level system and the 'heralded antibunching' of a heralded single-photon source could not be investigated. In fact, the statistics of the signal remains a classical (thermal) statistics even when conditioned with the detection of an idler. Detection of an idler enhances the probability of immediate detection of a signal. This is the non-classical signal-idler correlation. However, under cw excitation it is then still most likely to detect another signal photon right after (i.e., within the coherence time Δt) the first one. This correlation in triple coincidences, however, is typically completely hidden since experimentally required coincidence windows of duration τ_c are larger than Δt because of the limited time resolution of the setup, i.e., $\tau_c \gg \Delta t$. At least a limit to τ_c is enforced by the detector jitter $\tau_d \approx \tau_c$. Under these conditions, measurements of tripple coincidences only reflect the signal-idler correlation but not the statistics of the signal in heralded mode. In other words, as pointed out in reference [105] a coincidence window prevents the verification of one-arm second-order effects altogether.

To study SPDC single-photon statistics in heralded mode, the conditioned temporal second-order correlation function $g_c^{(2)}$ (analogous to equation 2.2) needs to be regarded. It describes the second-order coherence of the signal field *conditioned* on observing an idler photon at time t_i. For two signal photons at t_1 and t_2 it is defined as follows [103]:

$$g_c^{(2)}(t_1, t_2 \mid t_i) \equiv \frac{\langle \hat{E}_s^\dagger(t_1)\hat{E}_s^\dagger(t_2)\hat{E}_s(t_2)\hat{E}_s(t_1)\rangle_{pm}}{\langle \hat{E}_s^\dagger(t_1)\hat{E}_s(t_1)\rangle_{pm}\langle \hat{E}_s^\dagger(t_2)\hat{E}_s(t_2)\rangle_{pm}} \tag{3.5}$$

with $\langle ... \rangle_{pm}$ being averages over the post-measurement state (i.e., after detection of an idler photon) assuming sufficiently high detector time resolution and unity quantum efficiency for the idler photon detector. It is $\langle \hat{Y} \rangle_{pm} = \langle \hat{E}_i^\dagger(t_i)\hat{Y}\hat{E}_i(t_i)\rangle / \langle \hat{E}_i^\dagger(t_i)\hat{E}_i(t_i)\rangle$. $\hat{E}_s(t)$ and $\hat{E}_i(t)$ represent the scalar photon-units positive frequency electric field operators [106]

$$\hat{E}_j(t) = \frac{1}{2\pi}\int d\omega \hat{A}_j(\omega) e^{-i\omega t}\,, \quad j = s\,, i\,, \tag{3.6}$$

where $\hat{A}_j(\omega)$ is the corresponding output field operator in the frequency domain. As shown in reference [107], these output field operators can be related to the vacuum-state field operators at the input of the non-linear crystal using Bogoliubov transformations [108], which are commutator-preserving relations that transform Gaussian state

inputs into Gaussian state outputs. Thus, because the joint state of signal and idler is produced from the Gaussian vacuum state, it is a Gaussian state too [109]. Therefore, the joint output state is completely characterized by its first and second moments [110]. Its only nonzero moments are given by its temporal auto- and cross-correlation functions [107, 109]

$$\langle \hat{E}_j^\dagger(t+\tau)\hat{E}_j(t)\rangle = e^{i\omega_p\tau/2}R(\tau)\,, \tag{3.7}$$

$$\langle \hat{E}_j(t+\tau)\hat{E}_k(t)\rangle = (1-\delta_{jk})e^{-i\omega_p(t+\tau)/2}C(\tau)\,, \tag{3.8}$$

where δ_{jk} is the Kronecker delta function and $j,k = s,i$. The problem is therewith reduced to finding the appropriate $R(\tau)$ and $C(\tau)$ function for the particular experimental situation. Following reference [109] there is a physical justification for these terms: First, it is expected that for cw pumping the signal and idler photons are emitted at constant average rates. This is consistent with a linear increase of the auto-correlation function $R(\tau)$ from 0 to R_{SPDC} for $\tau = \pm b_1 \to 0$ where the interval $b_1 = \frac{1}{B_{SPDC}}$. Second, an idler photon appearing at a time t_i is accompanied by a signal emission at time t_1 that lies somewhere in the time interval $\pm b_2$ around t_i with $b_2 = \frac{1}{2B_{SPDC}}$. Therefore, the cross-correlation $C(\tau)$ is a constant step function, and it is $\sqrt{R_{SPDC}B_{SPDC}}$ on the interval $\pm b_2$ around $\tau = 0$ and zero otherwise. Accordingly, for an SPDC source the temporal auto- and cross-correlation functions are given in reference [104] as follows:

$$R(\tau) = \begin{cases} R_{SPDC}(1+\tau B_{SPDC}) & -\frac{1}{B_{SPDC}} < \tau \leq 0 \\ R_{SPDC}(1-\tau B_{SPDC}) & 0 < \tau \leq \frac{1}{B_{SPDC}} \\ 0 & \text{otherwise} \end{cases}$$

$$|C(\tau)| = \begin{cases} \sqrt{R_{SPDC}B_{SPDC}} & -\frac{1}{2B_{SPDC}} < \tau < \frac{1}{2B_{SPDC}} \\ 0 & \text{otherwise} \end{cases}\,, \tag{3.9}$$

where R_{SPDC} is the signal/idler photon-generation rate and B_{SPDC} is the bandwidth of the SPDC process. Based on the same physical argumentation in case of a down-conversion process *inside a cavity* with the linewidth γ one can find:

$$\begin{aligned} R(\tau) &= R_{SPDC}e^{-|\tau|/\Delta t} \\ C(\tau) &= \sqrt{R_{SPDC}/\Delta t}e^{-|\tau|/\Delta t} \end{aligned} \tag{3.10}$$

with $\Delta t = \frac{1}{2\pi\gamma}$. The peak shape in both cases is defined by the cavity, the height is unchanged compared to equation 3.9. Figure 3.8 compares auto-correlation and cross-correlation functions $R(\tau)$ and $C(\tau)$ for common configurations of SPDC (figure 3.8 (a)) and cavity-enhanced down-conversion processes, i.e., in an OPO (figure 3.8 (b)). It is apparent that the timescales of the SPDC process are several orders of magnitude smaller compared with cavity-enhanced down-conversion. This is the crucial advantage of cavity-enhanced down-conversion for the coincidence measurements presented here. The coherence time Δt is now determined by the quality of the cavity, i.e., it can be so large, that the timing resolution of the APDs and the data-acquisition hardware is high

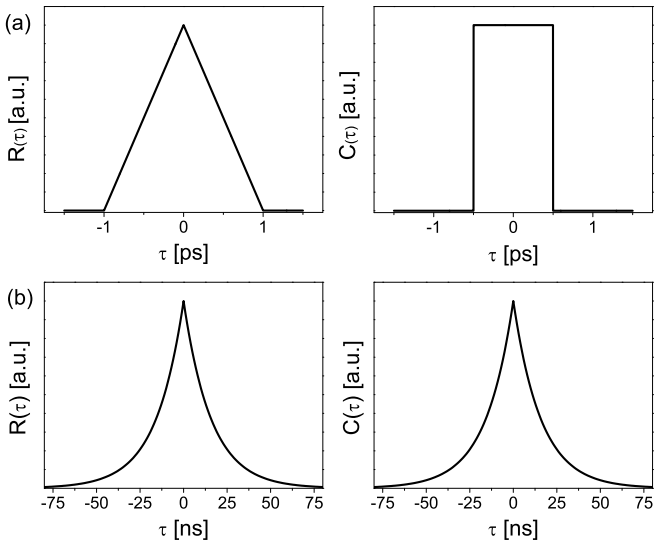

Figure 3.8.: Auto-correlation function $R(\tau)$ and cross-correlation function $C(\tau)$ for a SPDC process with a typical photon bandwidth $B_{SPDC} = 1$ THz (a) and cavity-enhanced down-conversion with a cavity linewidth $\gamma = 10$ MHz (b). Note that vertical scales are different. Note that in (b) the coherence time is determined by the cavity and is orders of magnitude larger than in (a).

enough to allow direct measurements of the signal-signal correlation after heralding with detection of an idler photon. Such measurements will be presented in section 3.4. In the experiment, accessible parameters are the signal idler coincidence rate $P_{si}(t_i + \tau, t_i)$ for having a signal photon at time $t_i + \tau$ and an idler photon at time t_i and the triple-coincidence rate $P_{ssi}(t_1, t_2, t_i)$ for two signal photons at time t_1 and t_2 and an idler photon at time t_i. These coincidence rates can be connected to $g_c^{(2)}(t_1, t_2 \mid t_i)$ in equation 3.5 using the quantum form of the Gaussian moment-factoring theorem (see reference [107]) as follows [104, 105]:

$$\begin{aligned} P_{si}(t_i+\tau, t_i) &\equiv \langle \hat{E}_s^\dagger(t_i+\tau)\hat{E}_i^\dagger(t_i)\hat{E}_i(t_i)\hat{E}_s(t_i+\tau)\rangle \\ &= \langle \hat{E}_s^\dagger(t_i+\tau)\hat{E}_i^\dagger(t_i)\rangle\langle \hat{E}_i(t_i)\hat{E}_s(t_i+\tau)\rangle \\ &+ \langle \hat{E}_s^\dagger(t_i+\tau)\hat{E}_i(t_i)\rangle\langle \hat{E}_i^\dagger(t_i)\hat{E}_s(t_i+\tau)\rangle \\ &+ \langle \hat{E}_s^\dagger(t_i+\tau)\hat{E}_s(t_i+\tau)\rangle\langle \hat{E}_i^\dagger(t_i)\hat{E}_i(t_i)\rangle \\ &= R^2(0) + |C(\tau)|^2 \\ &\equiv P_{si}(\tau) \end{aligned} \tag{3.11}$$

$$\begin{aligned} P_{ssi}(t_1,t_2,t_i) &\equiv \langle \hat{E}_i^\dagger(t_i)\hat{E}_s^\dagger(t_1)\hat{E}_s^\dagger(t_2)\hat{E}_s(t_2)\hat{E}_s(t_1)\hat{E}_i(t_i)\rangle \\ &= 2C(t_1-t_i)C(t_2-t_i)R(t_1-t_2) \\ &+ R(0)[R^2(0)+R^2(t_1-t_2)+C^2(t_1-t_i) \\ &+ C^2(t_2-t_i)] \end{aligned} \tag{3.12}$$

Then, the conditioned second-order correlation function, equation 3.5, can be written as

$$g_c^{(2)}(t_1,t_2 \mid t_i) = \frac{P_{ssi}(t_1,t_2,t_i)R(0)}{P_{si}(t_1-t_i)P_{si}(t_2-t_i)}. \tag{3.13}$$

Hence, it is fully defined by $R(\tau)$ and $C(\tau)$, which are both known for the OPO (equation 3.10) as well as by the experimentally accessible coincidence rates P_{ssi} and P_{si}.

3.4. Coincidence measurements

Based on the available narrow-band photons with very large coherence time Δt from the OPO, it is now possible for the first time to completely reveal triple coincidences and heralded correlations not hidden by coincidence windows anymore.

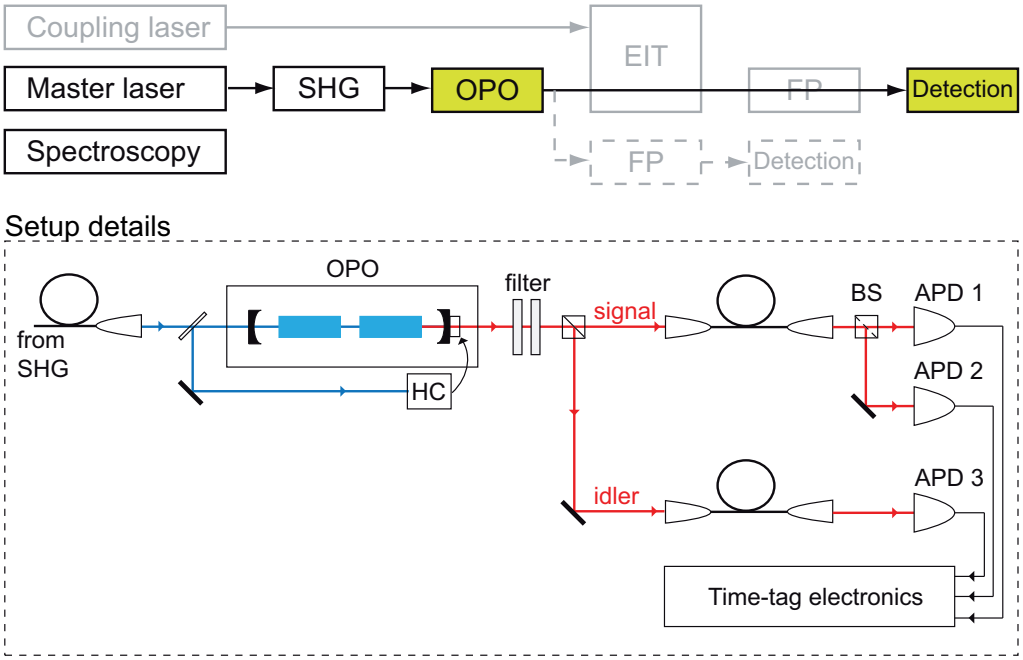

Figure 3.9.: Experimental setup for the direct measurement of triple coincidences and heralded signal-signal correlations. The signal and idler photons produced by the OPO are spectrally filtered to block the pump light and fed to a Hanbury Brown and Twiss setup and to a single avalanche photodiode (APD), respectively. All APD clicks are recorded using time-tag recording.

The experimental setup used to perform such measurements is shown in figure 3.9. Behind the OPO cavity the pump beam is blocked by long-pass filters, the generated signal and idler photons are separated by a polarizing beam splitter, and both are coupled into single-mode optical fibers. One fiber is directly connected to an avalanche photodiode (APD), the other to a Hanbury Brown and Twiss (HBT) setup, as described in section 2.1. Photon arrival times were recorded with 4 ps time resolution using a PicoHarp 300 (PicoQuant) single photon counting system in time-tag mode. From the recorded data the *time averaged* double-coincidence rate $\overline{P}_{si}(t_1, t_i)$ and triple-coincidence rate $\overline{P}_{ssi}(t_1, t_2, t_i)$ is calculated using software post-processing. It should be noted that the measurements in this thesis are denoted as $\overline{P}$ (according to the notation used in reference [103]) because they include averaging over the detection time jitter. However, in our case the detection jitter is negligible compared to all other relevant time scales and thus $\overline{P} \approx P$. Figure 3.10 shows the signal-idler coincidence rate $\overline{P}_{si}(t_1, t_i)$.

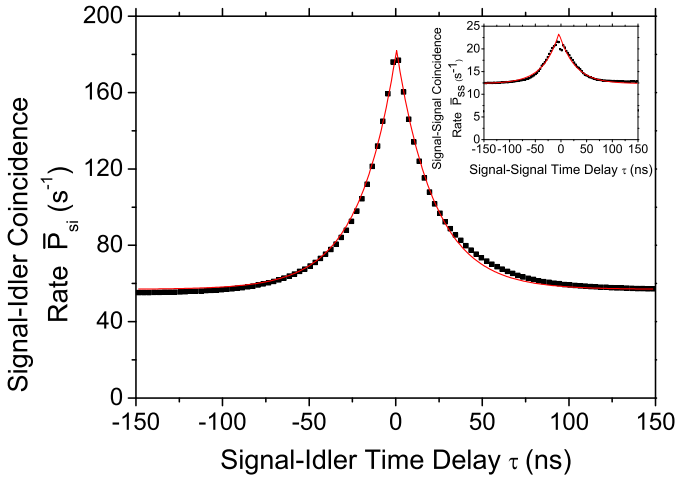

Figure 3.10.: Signal-idler correlation function $\overline{P}_{si}(\tau)$ for an idler photon measured with APD 3 of figure 3.9 at $t_i = 0$ and a signal photon at $t_1 = \tau$ measured either with APD 1 or 2. The shape reflects the OPO cavity linewidth of 7.2 MHz. The inset shows the measured untriggered signal-signal auto-correlation function measured with APD 1 and 2. Both measurements were binned with bin size $\tau_b = 3$ ns $\ll \Delta t$.

The rates were calculated from around 8 hours of raw time-tag data at a signal and idler photon rate of $\sim$ 200.000 counts/s each. Here, $t_i = 0$ is the arrival time of the idler photon. $t_1 - t_i$ and $t_2 - t_i$ are time offsets of corresponding signal photons. During software post-processing, signal photons with time offsets > 150 ns or < -150 ns were regarded as noise and discarded. Unlike in earlier studies [103, 104] no additional coincidence window was introduced. Hence, $\overline{P}$ was directly measured and not only its smeared approximation N as in those studies. To smooth the results for a graphical representation, the data was binned with a bin size of $\tau_b = 3$ ns, which is above the specified

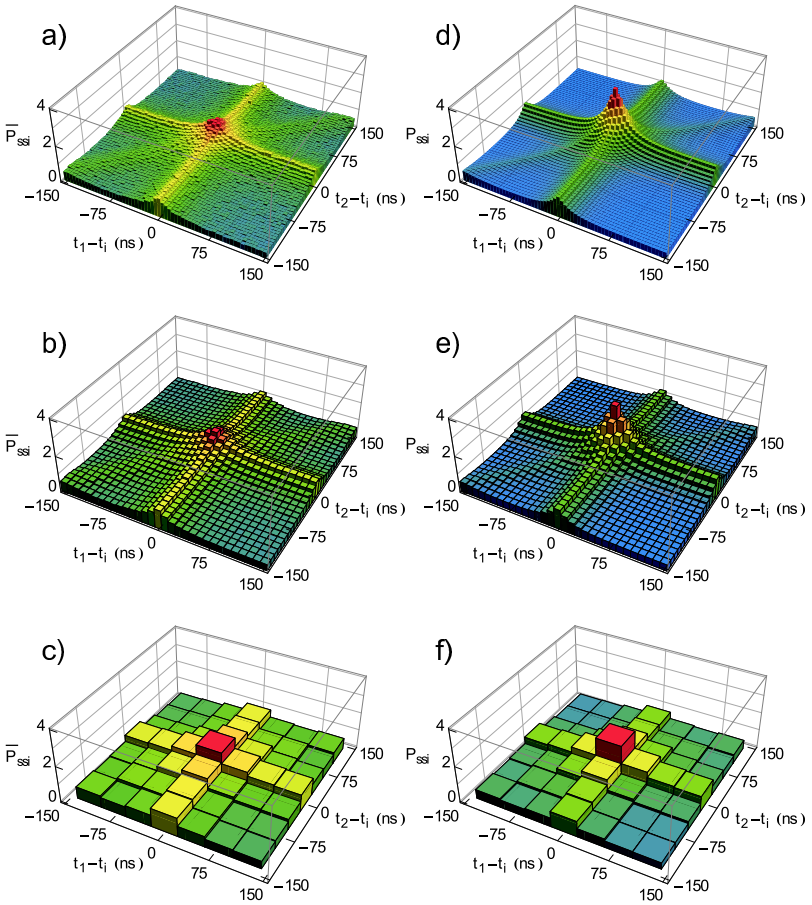

Figure 3.11.: Measured (a,b,c) and simulated (d,e,f) triple-coincidence rates $\overline{P}_{ssi}(t_1, t_2, t_i)$ and $P_{ssi}(t_1, t_2, t_i)$, respectively, for an idler photon at $t_i = 0$ and two signal photons at $t_1 - t_i$ and $t_2 - t_i$. The ridges of the plots are normalized without binning to 1, which represents the theoretical result in case of no background noise [105]. The measurements in a) b) c) as well as the simulations in d) e) f) are binned with bin sizes of 5 ns, 10 ns and 40 ns, respectively. See text for discussion.

detector jitter of $\tau_d = 600$ ps but far lower than Δt. In accordance with equations 3.10 and 3.11 the data is fitted by an exponential decay function and shows excellent agreement. The corresponding cavity bandwidth is found to be 7.2 MHz corresponding to a coherence time Δt of ~ 140 ns. It fits well to the cavity design-bandwidth of 5.4 MHz (see section 3.2.2) if one takes a slight decrease of the cavity finesse over time into account as the cavity was built more than one year ago. The perfect fit shown in figure 3.10 further justifies the characterization of the down-conversion process in the OPO given in section 3.3 which resulted in equation 3.10.

Figures 3.11 a), b), c) show the experimental triple-coincidence rates $\overline{P}_{ssi}(t_1, t_2, t_i)$

for three different bin sizes of 5 ns, 10 ns and 40 ns compared to their theoretical prediction $P_{ssi}(t_1, t_2, t_i)$ in d), e), f). The theoretical plots were calculated from the fitted auto-correlation and cross-correlation functions. In addition to the pure theoretical description in equation 3.10 a constant background A and B was added to account for stray light and noise photons. The auto- and cross-correlation functions therefore read

$$\begin{aligned} R(\tau) &= R_{SPDC} e^{|\tau|/\Delta t} + A R_{SPDC} \\ C(\tau) &= \sqrt{R_{SPDC}/\Delta t} e^{|\tau|/\Delta t} + B\sqrt{R_{SPDC}/\Delta t}\,. \end{aligned} \tag{3.14}$$

At first, figures 3.11 a) and d) will be discussed. Here, a small bin size of 5 ns is introduced for better graphical representation. The ridges running parallel to the axes $t_1 = t_i$ and $t_2 = t_i$ are given by the respective signal-idler correlation. The correlation reflects that signal and idler are always produced in pairs. In the experimental data set these values are used for normalization of the count rate. Away from the central area around $t_i = t_1 = t_2$, triple coincidences reflect the detection of a signal-idler pair together with an accidental detection of another signal photon (signal photons are continuously produced with a constant rate under cw excitation!). In the central area around $t_i = t_1 = t_2$ the correlations are considerably increased. Theoretically, a factor of 4 [105] is expected which can be understood as follows: Both signal and idler photons are created in pairs but with a thermal statistics. The probability to find a second photon in a short time interval within the coherence time is twice as large as in the case of a purely random (Poissonian) process (see also the inset in figure 3.10). At the same time, detecting an idler photon within the time interval Δt close to a signal photon is also twice as likely as a purely random coincidence. In summary, this yields a factor of 4. The measured value of only ~ 2 has several reasons. First, a satisfactory signal-to-noise ratio together with adequate measurement times require the OPO to be pumped slightly above the single photon level. Noise counts result from fully uncorrelated floor due to stray light, dark counts, and remaining pump photons as well as partly correlated counts from non-perfect signal-idler separation. Stronger pumping drives the statistics of pair emission closer to the Poissonian (purely random) case. Second, the time resolution of the measurement system also limits the central peak height. The diagonal bunching structure at $t_1 = t_2$ again reflects signal-signal bunching accidently triggered by random idler events. It can be included in the simulation by adding uncorrelated noise as present in the experiments (offsets A and B in equation 3.14).

Now, larger bin sizes of 10 ns and 40 ns are introduced in figures 3.11 b), c) and in e), f), respectively, in order to highlight the influence of a coincidence time window. Obviously, the shape of the experimental plot corresponds very well with the theoretical expectation. It can be clearly seen, that a coincidence window (introduced artificially here via the binning window) destroys detailed information about triple coincidences. The shape of the correlation-curve can no longer be derived. Only a step-like ridge (normalized to 1) and an enhanced central bin at $t_i = t_1 = t_2$ remains. The central enhancement decreases with decreasing ratio of $\Delta t/\tau_c$ [105]. Eventually, the central enhancement vanishes. Then, no information about the statistics of the pair emission

or heralded signal-signal correlation under cw excitation can be derived. The results in figure 3.11 show this transition for the first time.

Although the measured triple coincidences already contain the full statistical information about the SPDC photon-pair source, it is intuitive to represent the data in terms of the quality of the down-conversion source as *heralded* single-photon source. In order to do that, the second-order signal coherence function *conditioned* on the detection of an idler photon was calculated. To compare the heralded single-photon source with other single-photon sources, $\overline{g}_c^{(2)}(\tau) \equiv \overline{g}_c^{(2)}(t_i, t_i + \tau \mid t_i) = \overline{g}_c^{(2)}(0, \tau \mid 0)$ is most appropriate.

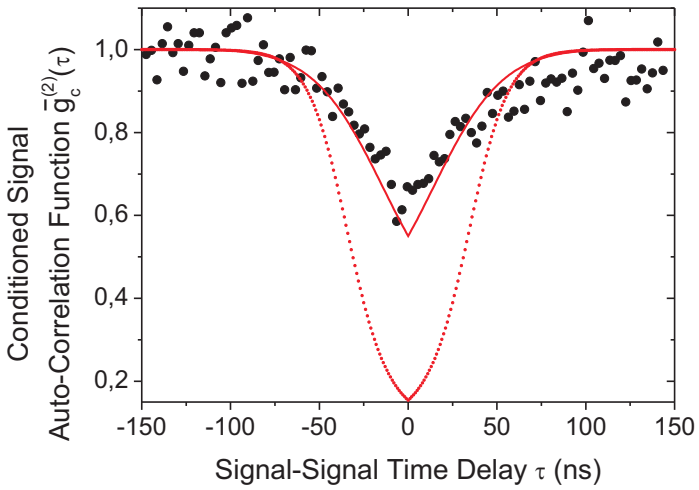

Figure 3.12.: Calculated second-order signal coherence function conditioned on the detection of an idler photon $\overline{g}_c^{(2)}$. The black dots represent measurements, the red line was simulated according to equation 3.13. The dotted line represents the same simulation but without the background noise.

As shown in figure 3.12, an antibunching feature is clearly visible with the typical signature of non-classical light emission. The antibunching dip does not go down to zero because of extra noise contributions, namely from a fully uncorrelated floor due to stray light, dark counts, and remaining pump photons as well as partly correlated counts from non-perfect signal-idler separation. The red line was simulated according to equation 3.13 including these noise contributions. In order to extract the pure (noiseless) heralded-photon statistics of the photons as generated by the cavity SPDC source, the simulation was performed again with the same parameters but without the noise contributions in R and C, i.e., $A = B = 0$ in equation 3.14. The result is shown by the dotted red line in figure 3.12.

The analysis highlights the fact that a heralded antibunching can be observed even if the single-arm statistics (of both idler and signal) is thermal. The dip in $\overline{g}_c^{(2)}(\tau)$ merely shows that photons are generated in pairs, i.e., that there is strong non-classical signal-idler correlation and that this correlation is independent of the pair-emission rate.

However, at the same time the probability to detect two or more photons in one arm within a certain fixed time window can be made arbitrarily small (by reducing the rate or shortening the time window). This is also valid for any single-photon statistics. Thus, the ratio of these two quantities can always enforce a dip, as seen in figure 3.12. In previous measurements where the detector's time jitter τ_d was much larger than the coherence time Δt of the photons [111], the heralded antibunching dip consisted of a single point. In contrast, our measurements plotted in figure 3.12 nicely resolve the coherence times or the temporal shape of the photon wave packet.

3.5. Discussion and short summary

In this subchapter, the concept of optical parametric oscillators and its realization inside a cavity was demonstrated. The single photon storage experiment (figure 1.5) will use an OPO which was recently developed in our group [54–57] as single-photon source. This OPO and the surrounding components of the experimental setup were briefly described. The OPO emits at a rate of $\sim 1.4 \times 10^6$ biphotons/s per mW pump power, and the emitted photons' spectral FWHM is 4.6 MHz. Their wavelength is matched to the $6^2\mathrm{S}_{1/2}(F = 3) \rightarrow 6^2\mathrm{P}_{1/2}(F' = 4)$ hyperfine transition in cesium in order to allow interfacing with an atomic system. More details about the atomic system and its application in the single photon storage experiment will be presented in chapter 5.

The heralded single-photon statistics of the OPO photons were studied in detail. The results show the first direct triple-coincidence analysis of two-photon states emitted from an SPDC source under cw excitation. Due to a tremendously enhanced coherence time compared to SPDC sources without a cavity, the detector's time jitter was negligible. Unlike in earlier studies [103, 104] this allows measurement without a coincidence window τ_c which eventually prevents the verification of one-arm second-order effects [105]. By later artificially introducing a coincidence window of increasing width it was possible to show the transition from a regime, where full signal-idler and signal-signal correlation properties are available to a limit, where the triple coincidences are merely determined by signal-idler correlations. So far only the latter limit was accessible. Signal-idler but also thermal signal-signal correlations were clearly resolved. The heralded antibunching characteristics were investigated, and it was shown that in this system further studies of continuously generated photon states, possibly higher photon number entangled states, can be performed to investigate their (non-)applicability in quantum information tasks.

3.6. OPO mode spectrum

As the analysis in section 3.4 already shows, there is strong non-classical signal-idler correlation, the signal and idler photons are always generated in pairs, i.e., at exactly the same time. Due to this property, the signal-idler cross-correlation function is actually more complex than what was derived in section 3.3. In fact, the signal-idler cross-correlation function $C(\tau)$ given in equation 3.10 exhibits the envelope of the full correlation function. This envelope is sufficient for the description of the triple-coincidence

measurements in section 3.4 because the detector jitter τ_d prevents the resolution of more details anyway. However, figure 3.7 (b) shows that more details are present in the correlation function. The red line depicted in this figure follows a more complex theoretical model of the double-resonant OPO and also takes into account the time resolution of the correlation setup of 620 ps. The full theoretical treatment of the double-resonant OPO can be found in references [57, 56]. Its final expressions for the output spectra are lengthy and will not be noted here explicitly. They follow the convolution of two combs, each consisting of individual Lorentzian lines, with a phase-matching envelope around the corresponding central signal or idler frequencies [112, 54]. The resulting exact cross-correlation function which was used – convoluted with the detector resolution – to calculate the red line in figure 3.7 (b) is given by [54]

$$G^{(2)}_{S/I}(\tau) \propto \left| \sum_{m_S,m_I} \frac{\sqrt{\gamma_S\gamma_I\omega_S\omega_I}}{\Gamma_S+\Gamma_I} \times \right. \\ \left. \times \begin{cases} e^{-2\pi\Gamma_S\left(\tau-\frac{\tau_0}{2}\right)}\, sinc\left[i\pi\tau_0\Gamma_S\right] & \forall\,\tau \geq \frac{\tau_0}{2} \\ e^{+2\pi\Gamma_I\left(\tau-\frac{\tau_0}{2}\right)}\, sinc\left[i\pi\tau_0\Gamma_I\right] & \forall\,\tau < \frac{\tau_0}{2} \end{cases} \right|^2 \tag{3.15}$$

with central signal and idler frequencies ω_S and ω_I, $\Gamma_k = \frac{\gamma_k}{2} + im_k\Delta\omega_{k,eff}$, $m_k \in \mathbb{N}_0$ ($k \in \{S, I\}$). $G^{(2)}_{S/I}$ consists of peaks with a temporal width τ_0 which accounts for the propagation delay between signal and idler photons inside the conversion crystal. The peak structure decays with cavity damping rates γ_S and γ_I, respectively.

Experimentally, the signal-idler correlation can be further studied if the detector jitter is small enough. Using two special APDs (PicoQuant MPD 5CTC) with a detector jitter $\tau_d \approx 50$ ps, this measurement was possible. However, these APDs have only $Q = 0.05$ quantum efficiency at 894 nm wavelength, which requires a high OPO pump intensity of 1 mW. Triple-coincidence measurements as shown in section 3.4 would not be possible with such a low quantum efficiency as the coincidence rate would be too low because it scales with Q^3.

In order to study signal-idler correlations the signal and idler photons generated by the double-resonant OPO were both directly coupled onto two APDs using single-mode fibers. The photon arrival times for $\sim 2 \times 10^9$ events were recorded with 4 ps resolution using a PicoHarp 300 single photon counting system in time-tag mode. Signal-idler correlation events were extracted from the recorded data and the respective time offset $\tau = t_S - t_I$ stored. At first, on a large time scale the data was fitted with an exponential decay function in order to find the peak position, and this information was used to correct for non-identical cable and optical path length. Afterwards, the signal-idler time offset was analyzed in detail for $|\tau| < 2.5$ ns. The same measurement was performed with only the signal photons being analyzed using a Hanbury Brown and Twiss detector configuration. For this signal auto-correlation measurement, the idler photons were discarded and $\sim 1 \times 10^9$ events were recorded.

The result of the full signal-idler correlation measurement is plotted in figure 3.13 (a). From the non-correlated photon rates, a background level due to stray light, non-perfect

filtered pump-light and detector dark counts was measured and subtracted. Additionally, on a broad time scale, the background from photon bunching was approximated by an exponential decay function determined by the OPO cavity linewidth (as shown in section 3.4) and also subtracted, the result from this calculation is shown in figure 3.13 (b). The inset in figure 3.13 (b) shows the signal auto-correlation measurement.

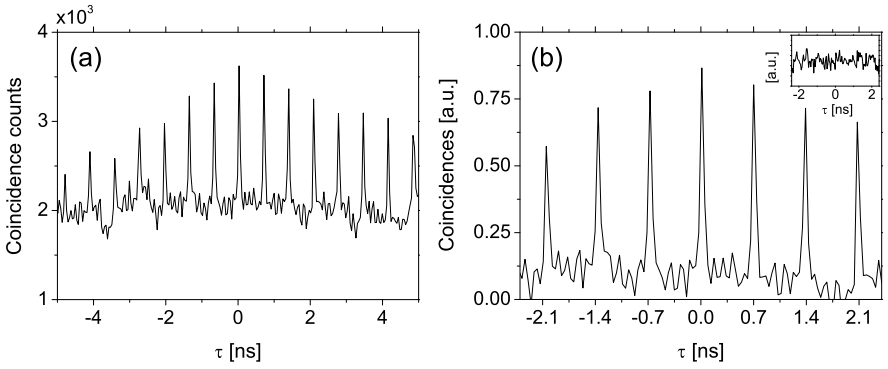

Figure 3.13.: Signal-idler correlation measurement. (a) Plot without noise subtraction. (b) Details around $\tau = 0$ after subtraction of background caused by noise photons and photon bunching. The peaks are equally spaced by ~ 700 ps corresponding to the cavity round trip time t_R. The inset in (b) shows the same measurement but for signal-signal correlations.

In figure 3.13 (b) the distinct time correlation of signal and idler photons is clearly visible. The coincidence counts appear in individual peaks, which are equally spaced by $t_R \approx 700$ ps corresponding to the cavity round trip time. The peak width is determined by the detector jitter t_d. The auto-correlation measurement (inset in figure 3.13 (b)) proves that the measured peak structure is not somehow related to the cavity or any other external effect. The parallel structure is often interpreted in a simple way, i.e., it reflects the signal wave packet which is bouncing between the two mirrors of the OPO. Only every round trip time t_R it is possible to detect a photon outside of the cavity. However, it has to be noted that the signal-idler pair is generated by a pump with a long coherence time ($\tau_{p,coh} \approx 200$ ns [57]) within the cavity. Therefore, before detection of an idler photon, no location of a signal photon wave packet in time shorter than $\tau_{p,coh}$ is possible. This situation is similar to the configuration described by Franson [113] to detect time-energy entanglement. Thus, the mere observation of the parallel structure in figure 3.13 (b) is an indication for time-energy entanglement of the signal and idler photon. The more complex structure of the signal-idler wave packet in an OPO and its relation to entanglement has been pointed out in reference [102], but it was not investigated further. The experimental configuration introduced here may be very useful to perform time-energy entanglement in an OPO in further studies.

4. Spectral Filtering of Single Photons

As shown in chapter 3, the generation of ultranarrow-band single photons is possible using cavity-based parametric down-conversion. However, as shown in figure 3.6, the OPO output is not single mode but a comb-like spectrum with around 50 modes spectrally separated by $\sim$ 1.5 GHz. Hence, in order to generate single-mode photons the OPO output needs to be filtered to transmit just one mode. This chapter presents an appropriate filtering setup together with its application in the single photon storage experiment (figure 1.5) and beyond.

Narrow-band spectral filtering of light is important in a vast field of applications, ranging from wavelength division multiplexing (WDM) in optical communication networks [114] to Brillouin microscopy [115] and lidar systems [116] to name just a few. Several spectral filtering concepts are well-known, however, just a few allow transmission windows in the sub-GHz regime, which equals wavelength on the picometer scale. Here, a filter based on a Fabry-Pérot cavity was chosen.

The chapter starts with the study of a Fabry-Pérot etalon as narrow-band spectral filter **(4.1)**. Subsequently, this filter is used for single-mode operation of the OPO **(4.2)**. In the last section, **(4.3)** a theoretic study is presented how such a filter might possibly enable long range free-space quantum key distribution at daytime.

A part of this chapter (4.1) was published in *Note: An ultranarrow bandpass filter system for single-photon experiments in quantum optics*, Rev. Sci. Instrum. **81**, 026108 (2010), another part (4.3) was published in *Ultranarrow bandwidth spectral filtering for long-range free-space quantum key distribution at daytime*, Opt. Lett. **34**, 3169 (2009).

4.1. Multi-pass etalon for spectral filtering

A Fabry-Pérot filter or etalon is one of the most widely used optical filters. Its free spectral range (FSR) and the transmission linewidth $\Delta\nu$ define the finesse of the device $F = FSR/\Delta\nu$. In theory, the finesse is given by the mirror reflectivity (R) only, yielding $F_r = \pi\sqrt{R}/(1-R)$, but in real setups several material parameters like surface flatness of the optical substrates and mirror tilt together with F_r require to generalize to the so-called *effective* finesse F_{eff} [117]. The performance of the filter is described by the contrast $C = T_{max}/T_{min} = (1+4F_{eff}^2/\pi^2)$ and the peak transmission, which is no longer $T_{max} = 1$ as in the ideal case but [118]

$$T_{eff} = F_{eff}/F_r < 1. \tag{4.1}$$

The effective finesse F_{eff} can be calculated from the reflective finesse F_r and the

surface or defect limited finesse F_d [118],

$$\frac{1}{F_{eff}^2} = \frac{1}{F_r^2} + \frac{1}{F_d^2}. \tag{4.2}$$

The defect limited finesse F_d in turn is calculated from the influence of spherical defects F_S (curvature deviation), Gaussian defects F_G (random aberration), and mirror tilt F_T: $\frac{1}{F_d^2} = \frac{1}{F_S^2} + \frac{1}{F_G^2} + \frac{1}{F_T^2}$. The defect contributions are in each case calculated from the respective deviation δ, expressed as m-th fraction of the operation wavelength λ, $\delta = \lambda/m$, as shown in figure 4.1. The specific contributions to the defect limited finesse were

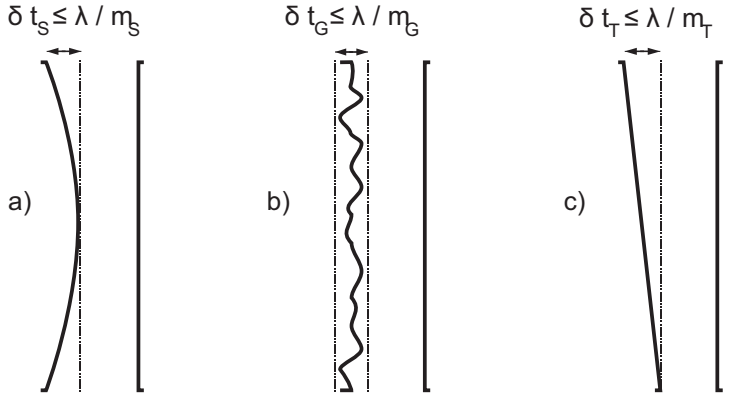

Figure 4.1.: Etalon substrate imperfections. a) spherical defects (curvature deviation), b) Gaussian defects (random aberration), c) mirror tilt.

found to be $F_S = \frac{m_S}{2}$, $F_G = \frac{m_G}{4.7}$ and $F_T = \frac{m_T}{\sqrt{3}}$ [118–120]. The etalon substrate quality and alignment thus limit the effective finesse and so the performance of the spectral filter, i.e., the filter contrast.

Equations 4.1 and 4.2 show that for a good filter performance F_d should be as high as possible and F_r (i.e., R) should be adjusted to maximize both transmission and effective instrument finesse. Besides a maximized surface quality a high F_d requires an active stabilization of the distance and parallelism of the mirror substrates to maximize the tilt-limited defect finesse $F_T \to \infty$, enabling also wavelength scanning of the instrument.

An enhancement of the contrast of the etalon filter can be obtained, if the signal beam traverses the whole etalon several times (n times) thus increasing the filter contrast from the single-pass contrast C_1 to the multi-pass contrast $C_n = C_1^n$. Due to the properties of the Airy-function, the finesse of such a multi-pass setup scales as $F_n = F_1(2^{1/n} - 1)^{-1/2}$ [117], and the transmission scales as $T_n = T_1^n$. Consequently, the increased contrast is achieved at the cost of a lower filter transmission. Therefore, a high single-pass transmission is very important in a multi-pass setup. In particular, if the filter is used in a quantum optics experiment, e.g. with photons carrying qubits, the loss of only a single photon is already associated with complete loss of information.

4.1.1. Experimental realization

The etalon used in this filter setup (Lightmachinery, Inc., Canada) was manufactured from highly polished flat mirror substrates with surfaces matched to $\lambda/280$ at the utilized wavelength of the Cs D1-line of 894 nm (see figure A.1 in the appendix). The reflectivity of the mirrors was specified to $R = 94\%$, i.e., $F_r \approx 51$. Due to a special polishing technique used by the manufacturer, the Gaussian defects including surface roughness can be neglected compared to the spherical defects $F_G \to \infty$, thus leaving the spherical defect limited finesse $F_S = \frac{280}{2} = 140$ and hence $F_{eff} \approx 48$. Actual measurements suggest a slightly higher mirror reflectivity of almost 94.8% and accordingly $F_r \approx 59$ and $F_{eff} \approx 54$. The FSR of the instrument is $FSR = 17.4$ GHz, which means only a deviation from the specified value of 18.2 GHz.

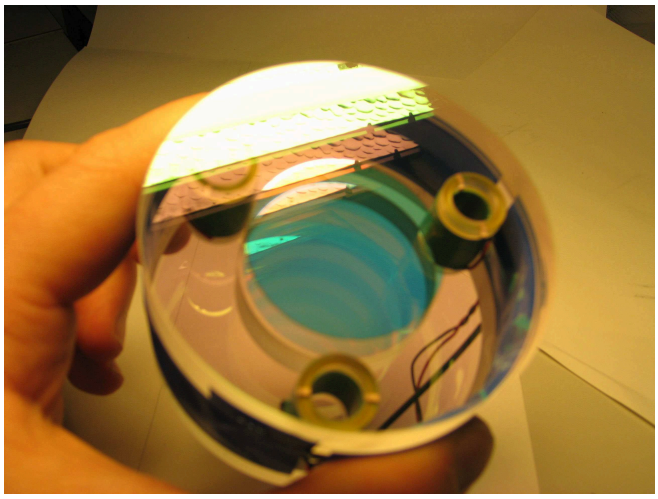

Figure 4.2.: Photograph of the etalon. Three piezo elements in tripod configuration together with an active stabilization using strain gauge sensors control the mirror distance and parallelism.

The mirror substrates of the etalon are connected by three piezo elements (Piezomechanik GmbH, Germany) in tripod configuration, as shown in figure 4.2. A closed-loop controller together with strain gauge sensors in each piezo element controls the mirror distance and parallelism with nanometer-precision, allowing a mirror tilt $< \lambda/1000$. A home-made offset-voltage generator allows individual and combined adjustment of the three piezos. An external ramp generator is used to perform a combined scan of all three piezos, i.e., a scan of the substrates' distance while maintaining parallelism. The whole electronics was built carefully in order to suppress noise as much as possible, because noise already in the mV range on the piezo would impede the necessary mirror parallelism. In order to reduce the inherent noise of the commercial piezo controller, filter capacitors were placed in parallel with the piezos. The spectral filter was built by placing the etalon in a home-made ultra-stable upright housing, as shown in figure 4.3. A 25 mm stainless steel base plate and beneath a 3-point support using small steel

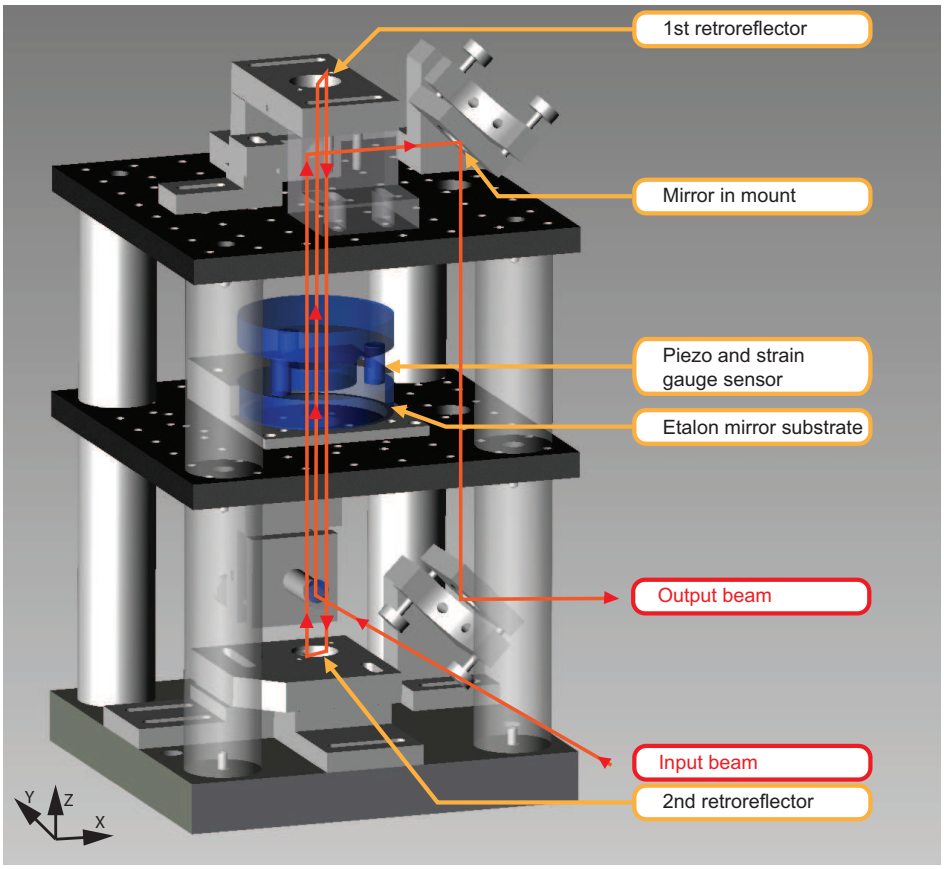

Figure 4.3.: Overview of the multi-pass etalon setup. The etalon itself is enclosed by a double-layered copper box for electromagnetic isolation. The whole setup is placed inside a foamed plastic box for acoustic and stray light isolation.

spheres maintain overall stability. Two solid retro-reflectors with anti-reflection coating are mounted movable in xy-direction and turnable around the z-axis above and below the etalon. The etalon itself is turnable around the z-axis and slightly movable in xy-direction. Small mirrors couple the light into and out of the z-axis. With a 1 mm diameter laser beam of a few mW power the adjustment was done, basically using back-reflections and the shape of the transmission signal as indicators while scanning the piezos. A double-layered copper box encloses the etalon itself, and a foamed plastic box is placed around the whole filter setup for acoustic and stray light isolation. For additional stray light reduction pinholes adjusted to the respective beam diameter are mounted in-between the etalon plates and between the etalon and each retro-reflector.

At first, the triple-pass etalon was analyzed in a test setup, as shown in figure 4.4. By scanning the interferometer mirrors over one FSR and fitting an Airy-function, as shown in figure 4.5, the etalon specifications were recorded.

The measured finesse of 105 is in good agreement with the expected value for the effective triple-pass finesse $F_3 = 106$. The measured peak transmission $T_{max} = 65\%$ is

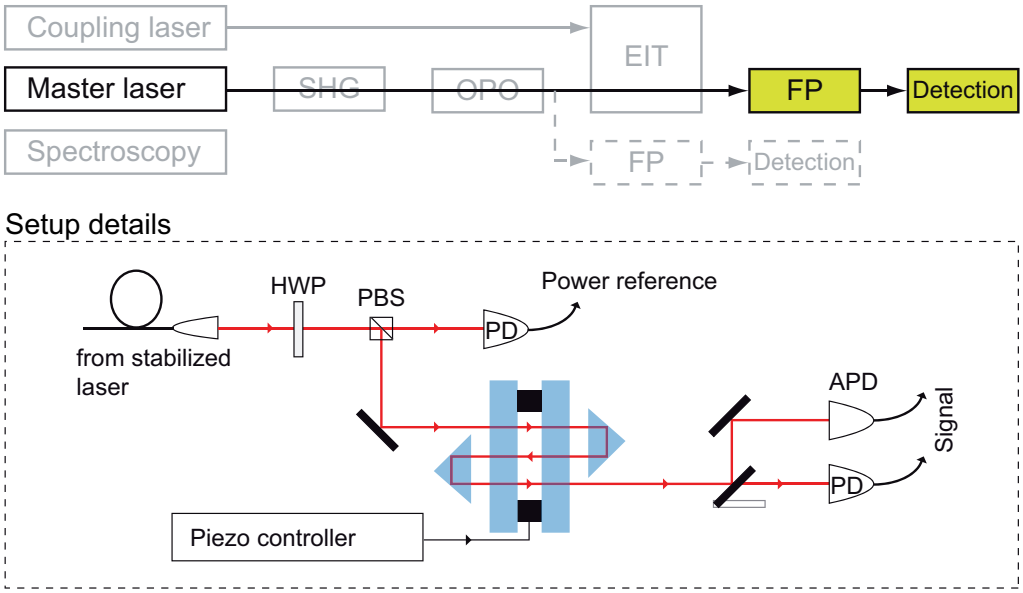

Figure 4.4.: Experimental setup used to verify the etalon performance. Light from a stabilized diode laser is fed into a stray light isolated box containing the multi-pass etalon, a reference detector, and two detectors behind the etalon. After adjusting the instrument, the signal light is strongly attenuated and measurements are performed using a single-photon APD.

lower than the theoretical maximum of $T_3 = 77\%$ and suggests an experimental single-pass transmission of 87% compared to $T_{eff} = 91.5\%$ from equation 4.1. This is probably

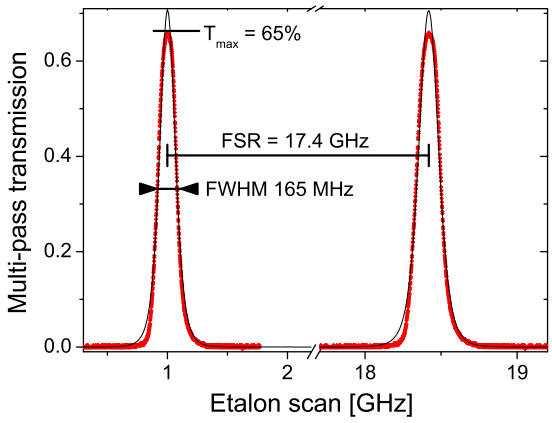

Figure 4.5.: Scan of the interferometer mirrors over one free spectral range (dotted curve). The solid black curve is the fitted Airy-function.

caused by several effects not considered in equation 4.1, i.e., non-perfect anti-reflection

coating of the outside of the etalon mirrors and the retro-reflectors, absorption in mirror substrates, non-perfect reflectivity of the retro-reflectors or coupling mirrors, etc. The triple-pass etalon suppresses off resonant light by 46 dB compared to a theoretically expected value of 90 dB. The single-pass suppression was measured to be 21 dB, which is already lower than the 30 dB expected from the above contrast calculations.

Another aspect studied was the effect of the multi-pass etalon on polarized light. While the etalon itself is polarization preserving, the retro-reflectors employ total internal reflection in order to maximize the amount of reflected light. Thus, the reflected light has an angle-dependent phase shift, i.e., the polarization is not necessarily preserved. It is however possible to use particular areas of the retro-reflectors which induce only a constant polarization rotation and ellipticity. Careful alignment of both retro-reflectors and two half-wave plates thus allows to transmit horizontally and vertically polarized light almost without distortion. It was found that only for one of the two polarization states an ellipticity of $2 - 3\%$ occurs.

4.1.2. Discussion and short summary

A multi-pass etalon was built and its performance studied. With a measured peak transmission of 65% and a suppression of off resonant light by 46 dB the performance is satisfactory for several tasks in the entire single photon storage experiment. The next section shows how this instrument is used to filter OPO photons and how it might be used in free-space quantum key distribution. In chapter 6 another even more challenging application in the context of single photon storage will be demonstrated.

Although the multi-pass contrast of the etalon filter in the setup is significantly lower than predicted by the simple to-the-power-of-n statement in multi-pass etalon theory, it is still $10 - 15$ dB better than other ultranarrow bandpass filters of comparable peak transmission [114]. The contrast measurements suggest that the reduced performance compared to theoretical expectations is caused by stray light and effects of beam broadening between the passes which limit the performance in multi-passing. However, strong variations between theoretical and experimental multi-pass contrast have been observed in other implementations as well [121, 122]. There are other multi-pass etalon implementations with far higher contrast, e.g., > 170 dB [121], but at the cost of much lower peak transmission, e.g., 10% in this example. Directly scaling the 170 dB contrast to an acceptable peak transmission of 60% by using a hypothetical double-pass configuration would result in just 38 dB contrast. Compared to other ultranarrow bandpass filters the etalon based filter is more flexible and adaptable to the particular task. For example, filters based on absorption of an atomic transition, which are often used in single photon experiments in combination with atomic systems [69], are very narrow-band and have good transmission but lack fast and easy tunability. Furthermore, they are only available for a particular wavelength corresponding to the specific atomic level scheme, e.g., there is no suitable atomic system available for a Cs based setup, as will be discussed in chapter 6. Filters based on Fiber Bragg gratings generally have the disadvantage of higher dampings, they are commercially available with < 3 dB attenuation only for telecom wavelengths, and commercial DWDM filters have too broad passbands [114].

Polarization of linear polarized light is mostly preserved, i.e., the whole filter produces $2-3\%$ elliptical polarized light from linear polarized incident light. This is due to the solid corner cube retro-reflectors, and by using hollow retro-reflectors that do not rely on total internal reflection, a considerable improvement of polarization preservation can be expected. This is important in a situation where the filter might be used to filter both signal and idler photons in order to separate them afterwards by using a polarization beam splitter.

4.2. Single-mode operation of the OPO

The multi-pass etalon described above can be used as filter in order to reach single-mode operation of the OPO. Through its small transmission window of 165 MHz FWHM only a single OPO mode will be transmitted as two consecutive OPO modes are spectrally spaced by ~ 1.5 GHz. However, the *FSR* of the multi-pass etalon is only a fraction of the width of the down-conversion process of ~ 61 GHz, therefore, a second filter is required to suppress further OPO resonator modes at a multiple of the *FSR*. An additional small etalon was chosen for this task. This small etalon is composed of a ring piezo with two directly attached mirrors of 0.9 reflectivity. The mirror distance is 3 mm resulting in an $FSR_S = 50$ GHz. The theoretical linewidth without any defects would be 1.7 GHz, but due to mirror imperfections and non perfect mirror parallelism a resulting linewidth of 2.7 GHz was measured which corresponds to an effective finesse of $F_{eff} = 18.5$. The peak transmission was measured to be 88%. Figure 4.6 shows the simulated transmission of the OPO output modes through a filter setup consisting of the two filters.

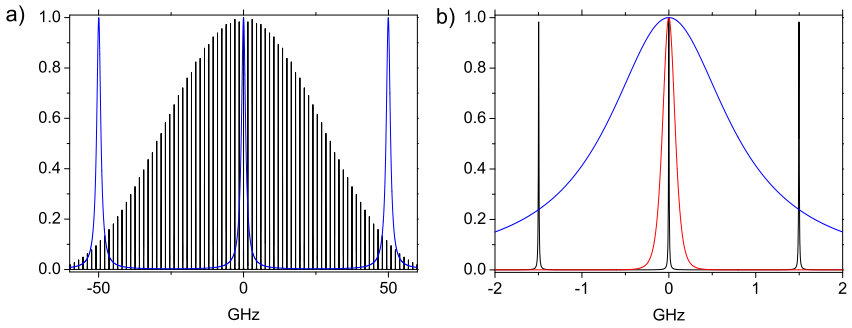

Figure 4.6.: (a) Simulated transmission of the OPO output modes through the filter setup. The black line shows the OPO spectrum within the phase-matching envelope while the blue line follows the calculated transmission of the small etalon. (b) Enlargement of the central OPO mode. The red line shows the measured transmission of the multi-pass etalon. The peak transmission was set to 1 for all filters in order to simplify the diagram.

For simplification, in the simulation the peak transmission of each filter was set to one. The experimental setup including both etalons is shown in figure 4.7. With both etalons in place a peak total transmission of 50% was measured showing only a small reduction compared to the theoretical maximum of 57% with the two particular filters. The reduction is mostly caused by a non-perfect beam shape behind the first etalon limiting the performance of the second etalon. Other effects like parasitic etalons were reduced as far as possible using AR coated surfaces and appropriate separation of the instruments.

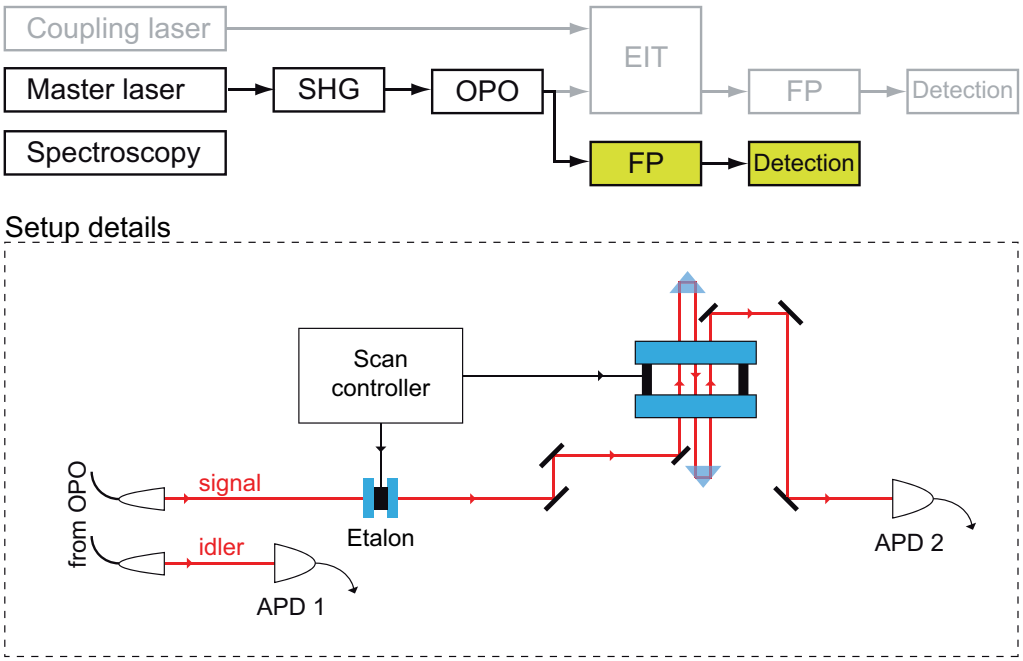

Figure 4.7.: Experimental setup for single-mode operation of the OPO. The signal field is filtered using two consecutive Fabry-Pérot etalons, see text.

In order to scan the OPO output using both etalons, they need to be scanned jointly. Due to different required voltage ramps and non-linearities, caused for example by hysteresis, this is not a trivial task. Using two simultaneously triggered arbitrary waveform generators a mostly linear scan across a few GHz was possible. However, due to non-perfect alignment of the two etalons the transmission was mostly constant for a range of below 1 GHz only. However, as such a combined filter is normally not operated in scanned mode but with a fixed central wavelength, this is not a problem for the further experiment. Figure 4.8 shows the result of several performed scans of the OPO photons.

The peak positions remain constant to < 300 MHz, and the OPO FSR is clearly visible. To further study the OPO output, an additional filter built from a heated Cs vapor cell was used together with the two-etalon filter (shown as black curve in figure 4.8). As the master laser for the whole experiment is locked to a Cs transition, one of the OPO lines is expected to be spectrally located just at the position of this Cs transition. Accordingly,

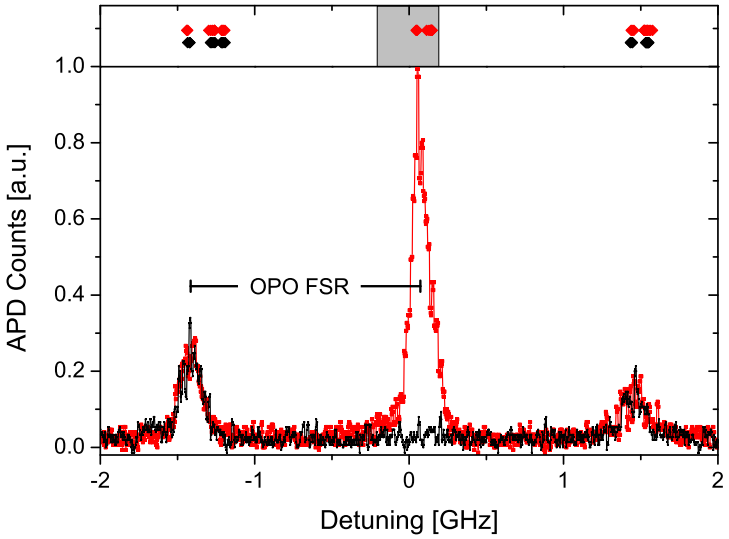

Figure 4.8.: Scan of the combined 2-etalon system over ∓ 2 GHz around the $6^2S_{1/2}(F = 3) \rightarrow 6^2P_{1/2}(F' = 4)$ Cs^{133} transition. The black (red) dots show measurements with (without) the Cs absorption cell in place. The grey area represents the width of the Doppler-broadend Cs transition at the adjusted cell temperature of 40 °C. The top figure shows fitted peak positions of several scans, the bottom figure shows one scan exemplarily. The different OPO modes separated by one FSR of the OPO cavity are clearly visible, the FWHM of the peaks of ~ 130 MHz is largely determined by the width of the multi-pass etalon. The variations in peak height are caused by non-perfect etalon alignment resulting in non-constant etalon transmission during the scan. The central mode is fully absorbed by the Cs atoms as expected (black curve).

this spectral mode is fully absorbed by the Doppler-broadened Cs transition, which has a width of around 380 MHz. This corresponds exactly to the measurement, where the side-peaks remain unchanged while the central peak is fully absorbed. The measurement proves that the combined filter fully suppresses all but one spectral modes of the OPO, i.e., the output field is indeed single mode.

4.2.1. Doppler-free saturation absorption spectroscopy

In order to measure the exact frequency of the OPO photons, a Doppler-free saturation absorption spectroscopy setup can be envisioned. Such a setup would consist of a glass cell filled with isotopically pure ^{133}Cs and two counter-propagating laser beams, a probe and a pump beam. The OPO idler photons could be used as probe beam, whereas for the macroscopic pump beam the master laser could be used. Two AOMs could detune

the pump laser around the Cs transition.

Although the required setup is in principle straightforward, the experimental realization is challenging due to excess noise from the intense pump light on the single-photon detector that is required for detecting the OPO photons. First tests showed that, even though probe and pump beam are counter-propagating and although a very high-quality polarization filter was used to suppress the pump light in front of the detector, it is not possible to use the required pump power in such a setup. The resulting stray light, e.g., from back-reflections from the cell windows in spite of AR coating, would even destroy the single photon counting APD ($> 10 \times 10^6$ counts/s). However, it is possible to perform such measurements if temporal filtering is used. This was tested with an AOM that regularly switches the pump light on and off together with a push-pull control of the APD gate, the experimental setup is shown in figure 4.9.

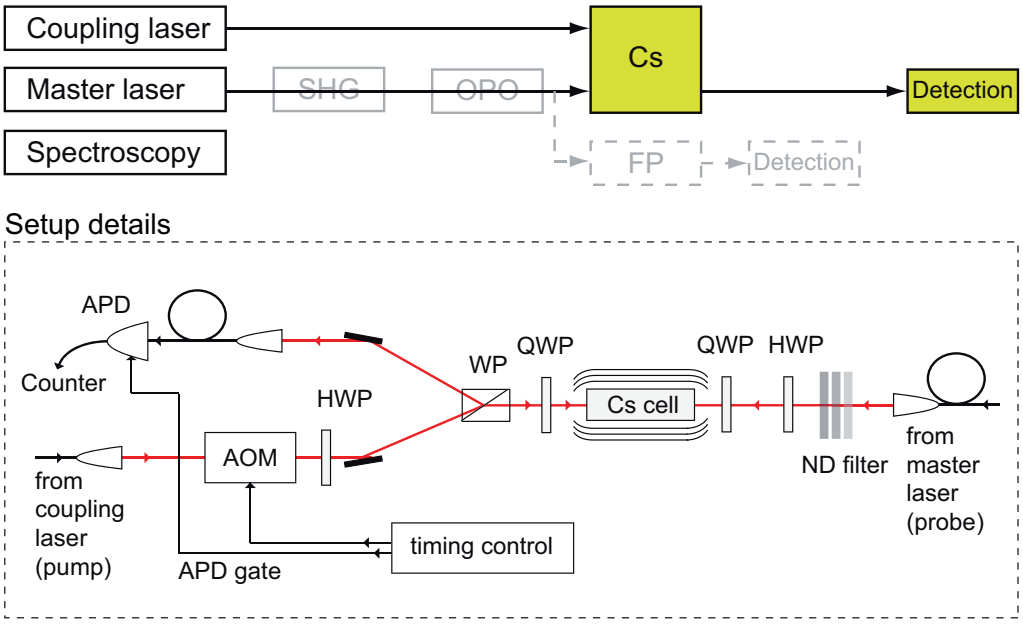

Figure 4.9.: Doppler-free saturation absorption spectroscopy setup with temporal filtering. Master laser (here: probe laser) and coupling laser (here: pump laser) are counter-propagating through a magnetically shielded Cs cell. A Wollaston prism (WP) is used to combine the beams and filter pump light which might be accidentally reflected at the cell window. The pump laser is switched by an AOM, it is further blocked in front of the detector by spatial filtering using a single-mode fiber. A gated APD detects the probe light behind the cell.

Figure 4.10 shows the optimized timing control signals which were found in experimental pre-studies using attenuated light from the master laser as probe light instead of the OPO photons. The timing was optimized with respect to all relevant experimental parameters, i.e., adequate signal-to-noise ratio of the probe laser modulation through

absorption spectroscopy, low detector noise caused by the coupling laser, and a required probe power as low as possible. It accounts for AOM rise/fall times and APD gating death times.

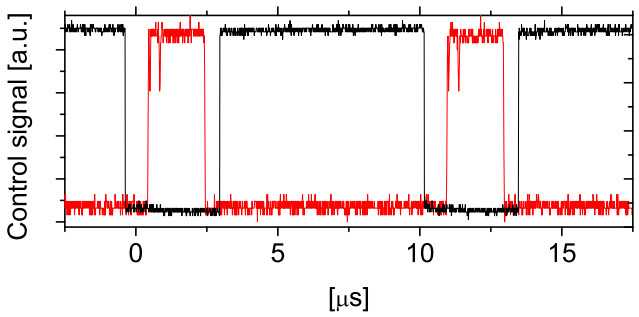

Figure 4.10.: Timing control for single-photon spectroscopic measurements. The red line shows the control signal for the AOM which switches the pump laser, the black line is the APD gate control signal. The small dip in the AOM signal is caused by the electronics, it does not affect the pump laser amplitude.

With this optimized timing configuration Doppler-free absorbtion spectroscopy measurements were possible with a minimum probe intensity in front of the cell of around 1.5×10^5 counts/s. A peak transmission of 30% through the cell was measured with a time-averaged pump intensity of 0.55 mW, as shown in figure 4.11.

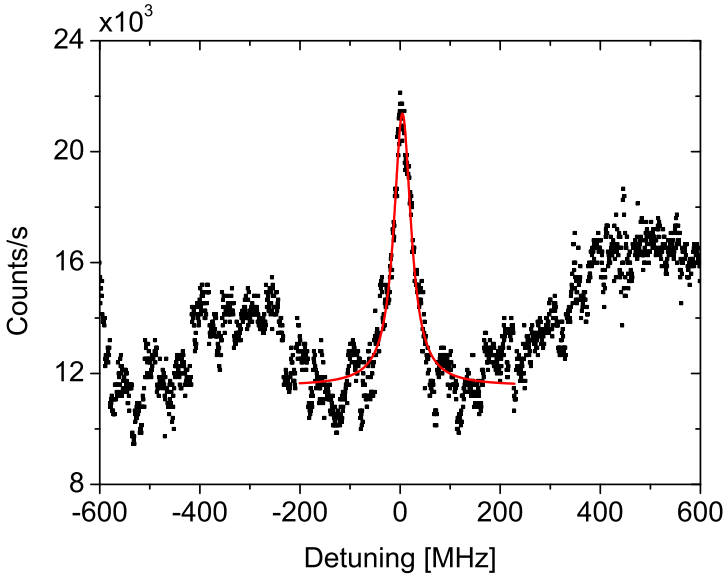

Figure 4.11.: Scan of the pump beam around the $6^2S_{1/2}(F = 3) \rightarrow 6^2P_{1/2}(F' = 4)$ Cs^{133} transition frequency in a Doppler-free absorption spectroscopy setup using temporal filtering. The peak was fitted with a Lorenzian, the FWHM is 40 MHz. The background is frequency dependent due to scattering of pump light in the Cs cell.

The scan in figure 4.11 was performed by modulating the laser current of a free running laser. The probe beam had an intensity of only 1.5×10^5 counts/s ($\sim 4.3\times10^5$ photons/s), it was frequency locked to the $6^2S_{1/2}(F = 3) \rightarrow 6^2P_{1/2}(F' = 4)$ Cs^{133} transition. The peak FWHM is 40 MHz, but it can be expected to be narrower if a frequency locked pump beam is used which can be scanned by two AOMs.

This measurement can be regarded as proof-of-principle demonstration of Doppler-free saturation absorption spectroscopy measurements utilizing OPO photons. It should be extended by two AOMs for scanning of the pump laser instead of a free running laser that was scanned by current modulation, as it was used in this test experiment. This improvement should further reduce the FWHM of the peak. Although a very low probe intensity was used, the Doppler-free transmission peak is clearly visible in figure 4.11. If used in combination with coincidence detection of signal and idler photons in an appropriate coincidence window of 200 ns length and with signal photon filtering using both etalons as shown above in figure 4.7, a signal-to-noise ratio around 1.5 times higher can be expected. This means that absorption spectroscopy with single OPO photons as probe beam should be possible if appropriate components (AOMs) for frequency scanning of the pump beam are available. Such an experiment will be performed in the near future.

4.2.2. Discussion and short summary

Single-mode operation of the OPO using two etalon filters was shown. Without scanning, the filters are stable for hours and an excellent total transmission of 50% was reached. The combined filters allow triggering of a measurement system only if an idler photon of a specific spectral mode is present. Due to the energy conservation during the down-conversion process, it can be expected, that the corresponding signal photon wavelength is sharply defined as well. This would allow triggering of storage experiments exactly when a spectrally compatible signal photon is present. Alternatively, the filtered photons could be used as single-mode single-photon source for other experiments. In the future, further studies of the single-mode single photons are planned with regard to photon statistics and correlations of signal and idler photons filtered with two individual filters. A second double-pass etalon whose FSR is already sufficient for filtering of OPO photons was already built. A very interesting experiment would be to perform coincidence measurements between different combinations of signal and idler spectral modes. One can expect to find strict correlations between the spectral modes [123] and possibly extend this to studies of multi-mode entanglement [124].

In addition, it was shown that the central wavelength of the single-mode photons is in the interval of the Doppler-broadened Cs transition, which is a prerequisite for later experiments involving a (quantum) interface between OPO generated photons and atoms. Although the fluctuation of the peak position in the scanned measurement is mostly caused by the limited performance of the joint-scanning electronics, for in-depth studies of the spectral properties of the OPO modes the transmission width of the multi-pass etalon is too broad. A solution would be to combine the filtering with a Doppler-free Cs spectroscopy setup to study spectral parameters of the OPO photons

with MHz resolution. Pre-studies for such an experiment were already performed and the realization will certainly be possible in the near future.

4.3. Ultranarrow bandwidth spectral filtering for long range free-space quantum key distribution at daytime

As already mentioned in the beginning of this chapter, spectral filtering of single photons is important for several tasks in quantum optics. In particular, the ability to work with very narrow-band single photons paves the way to other interesting applications. This shall be exemplified here in the field of quantum key distribution (QKD) [20].

4.3.1. Introduction

In quantum information technology QKD stands out as the first true application. Several fiber or free-space links have been realized [44, 45, 125–127], and today it is possible to link distances of > 100 km and build QKD networks [128]. However, due to losses in optical fibers the length of fiber based links is limited. Quantum repeaters (see chapter 8) might be a possible solution but the experimental realization of a long range repeater-supported QKD link is still far away. Recently, satellite based QKD implementations have gained much attention as they would allow to bridge global distances [129, 46] with a single link, mainly due to the fact that most of the propagation path is in empty space with no absorption. Only a small fraction of the path (corresponding to less than 10 km) is in atmosphere where the photons undergo absorption and turbulence-induced beam spreading. While geostationary satellites are too distant to implement a single-photon link, several proof-of-principle experiments have been performed, showing that QKD links to low-earth-orbit (LEO, from 500 to 2000 km above earth surface) satellites are possible [130, 131, 45, 132]. The feasibility of a single-photon down-link from a LEO satellite was also demonstrated [133]. Bonato et al. presented an analysis of different aspects of QKD between a LEO satellite and a ground station [46], showing among others the great advantage of a downlink over an uplink with regard to link-efficiency. This is mainly caused by beam displacement in the atmosphere induced by turbulent eddies. In the uplink the beam first travels through the turbulent atmosphere and then propagates, aberrated, in the vacuum to the satellite. The initial atmosphere-induced aberrations greatly increase the beam spreading, resulting in a very strong attenuation for a given receiver telescope size. For a relatively low satellite, at 500 km above the earth surface, the attenuation is of the order of more than 50 dB. On the other hand, for satellite downlinks the beam arrives at the atmosphere with a size much larger than any turbulent eddy, therefore there, is no significant beam wandering. Moreover, the beam propagates through the turbulent atmosphere only in the final part of its path, resulting in a reduced beam spreading compared with the uplink and hence an attenuation of the order of around 15 dB only. Consequently, proposed projects for space-based QKD [134] aim at distributing an entangled two-photon state from space to two receivers on earth which, among other experiments, would allow to establish a QKD link between the two

receiver positions, as shown in figure 4.12.

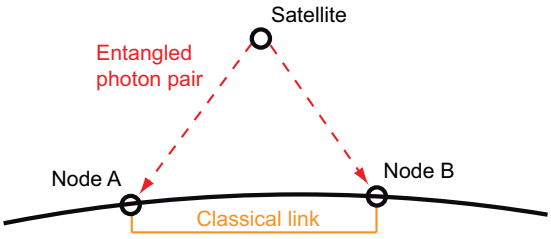

Figure 4.12.: Proposed experiment for distribution of entangled two-photon states from space to two receivers on earth (Node A,B). The received photon states would allow fully secure communication between the nodes over a classical channel.

In spite of the progress already made, most free-space QKD experiments are limited by the fact that they work at night-time only, due to stray light leading to detector noise during daylight operation. In fact, the two crucial points for any communication system are the amount of attenuation of the link and the noise introduced into the system. This is even more important for quantum communication, since the signal transmitted is ideally one photon, and one cannot increase the signal power in order to have a good enough signal-to-noise ratio (SNR). The only available tools are the reduction of the link attenuation and of the background noise. SNR calculations in reference [46] show, that for a link distance of 500-2000 km (i.e., LEO satellites) the SNR is greater than one only at night-time. On the other hand, due to the high signal attenuation key rates are usually very low [131] meaning that long key generation times are required. Being able to perform QKD during all times of the day, i.e., also with additional noise photons from daylight, is therefore an advantage. The relative brightness of a clear day typically increases by three orders of magnitude compared to a night with a full moon [135].

Both, the above theoretical considerations and the experimental realizations rely already on several filters to suppress stray light, namely spatial filtering, temporal filtering, and spectral filtering. Potential further improvement for the first two filtering techniques is limited, due to refractive index inhomogeneities induced by atmospheric turbulences causing beam wandering and spreading. In contrast, spectral filtering is not pushed to the limit yet, the filters used so far have a spectral transmission FWHM as broad as 0.15 to 10 nm.

4.3.2. Etalon performance in a QKD setup

To demonstrate the advantage of a multi-pass Fabry-Pérot etalon in this context, the effect of an additional filter on the potential performance of a long range free-space QKD setup was calculated. The calculations were based on the following requirements: For acceptable key rates, e.g., with state-of-the-art decoy-state based QKD setups [23, 136, 137], the overall attenuation of the quantum channel should not much exceed 30 dB [131]. As today's long range QKD setups work with an overall attenuation of already 25 –

30 dB [45], any additional damping by the filter should be as low as possible. Other requirements, namely tunability and long-term stability are already met by the multi-pass Fabry-Pérot etalon. Polarization preservation is desirable, otherwise several filters may be needed in front of each detector when a polarization-based encoding is used. In general, the etalon filter should be matched to the properties of the specific QKD setup. The latter refers for example to the available photon source and timing resolution. The filter FWHM should be of the order of a few 100 MHz to 1 GHz, i.e., $\sim 0.2 - 2$ pm at the relevant wavelength for transmission through the atmosphere, e.g., $\lambda \approx 800$ nm. To give an example: With a single-photon source of 1 GHz linewidth the etalon mirror distance should be adjusted to 0.5 mm, i.e., $FSR = 300$ GHz.

At first, the transmission of photons from a LEO satellite needs to be simulated. For a receiving telescope described as a circular aperture of radius R the link-efficiency η is given by [46]

$$\eta = \eta_0 \left(1 - e^{-2R^2/w_{LT}^2}\right) , \tag{4.3}$$

with the long-term beam width w_{LT} and an empirical factor η_0 for detection efficiency, pointing losses and atmospheric attenuation which can be found to be $\eta_0 \approx 0.1$ [129]. For a collimated Gaussian beam of waist w_0, w_{LT} is found to be [138]

$$w_{LT}^2 = w_0^2 \left(1 + \frac{L^2}{Z_0^2}\right) + 2\left(\frac{4L}{kr_0}\right)^2 , \tag{4.4}$$

where $Z_0 = \frac{\pi w_0^2}{\lambda}$ is the Rayleigh range of the beam, L is the propagation distance and r_0 is the Fried parameter given by

$$r_0 = \left[0.42k^2 \int_0^L C_n^2(z) \left(\frac{L-z}{L}\right)^{5/3} dz\right]^{-3/5} . \tag{4.5}$$

This estimation in equation 4.5 is performed by integrating the turbulent contribution of the atmosphere along the whole optical path. The refractive index structure constant C_n^2 can be found in reference [139] to be $C_n^2(h) = 0.00594(v/27)^2(h \times 10^{-5})^{10} e^{-h/1000} + 2.7 \times 10^{-16} e^{-h/1500} + A * e^{-h/100}$, where $A = 1.7 \times 10^{-14}$ and $v = 21 ms^{-1}$.

Furthermore, the background noise for the downlink needs to be taken into account. The noise power received by the telescope P_N and the number of noise photons per detector gating N_{Photon} can be expressed as follows [135]

$$P_N = H_b \Omega_{fov} R^2 \Delta\nu \tag{4.6}$$

$$N_{Photon} = \frac{P_N \Delta t}{E_{Photon}} , \tag{4.7}$$

where H_b is the brightness of the sky background in $Wm^{-2}sr^{-1}\mu m^{-1}$, Ω_{fov} is the field of view of the telescope in sr and R its radius. $\Delta\nu$ is the bandwidth of the spectral filter, Δt the width of the detector time gate and E_{Photon} the mean noise photon energy defined by $\Delta\nu$. H_b is strongly related to the weather conditions, typical values can be

found in table 4.1 [140, 141].

Conditions	Cloudy daytime	Hazy daytime	Clear daytime	Full moon clear night	New moon clear night
Typical brightness H_b $(Wm^{-2}sr^{-1}\mu m^{-1})$	150	15	1.5	1.5×10^{-3}	1.5×10^{-4}

Table 4.1.: Typical values for brightness of the sky background for different weather conditions.

4.3.3. Results

The figure of merit for the QKD satellite downlink is its signal-to-noise ratio, including the transmission T_{Signal} (T_{Noise}) of signal (noise) photons by the multi-pass Fabry-Pérot etalon (see section 4.1.1), the number of noise photons per detector gating N_{Photon} and the link-efficiency η

$$SNR = \frac{\eta}{N_{Photon}} \cdot \frac{T_{Signal}}{T_{Noise}} \,. \tag{4.8}$$

In reference [46] parameters for a real world scenario are provided which where then combined with the measured parameters of our multi-pass Fabry-Pérot etalon. The simulation includes a $\Delta\nu = 1$ nm bandpass filter for the incoming photons, $\Delta t = 1$ ns detector gating, an earth-based receiving telescope of 1.5 m diameter with field-of-view 0.016° for a 500 km down-link from a LEO satellite to earth. As shown in figure 4.13, the simulation clearly demonstrates that such a filter brings daytime operation of satellite-based QKD within reach. For example, with a transmitting telescope diameter $d_T =$ 30 cm during a clear day the SNR would be already around 4.8 dB.

In a real long range free-space application the beam undergoes spatial fluctuations and wave-front distortion. Although for a satellite down-link one can expect these effects to be lower than for an up-link or a long range link on earth's surface [46], it should be tested in such a setup whether they reduce the filter transmission. If so, the effect could be compensated by using adaptive optics, as already shown in reference [142]. As a simple test for the sensitivity of the instrument to wave-front distortion, a hot soldering-iron was put below the beam in front of the filter [143], but no notable change in filter transmission was observed.

4.3.4. Discussion and short summary

Simulations were demonstrated that show how a multi-pass etalon could enable free-space quantum key distribution between low orbit satellites and earth due to a significant increase of the signal-to-noise ratio of such a link. In this context the flexibility of etalon based filters is again a great advantage, e.g., it allows fast and easy tunability to compensate for Doppler shift of photons from moving satellites. All in all, it seems

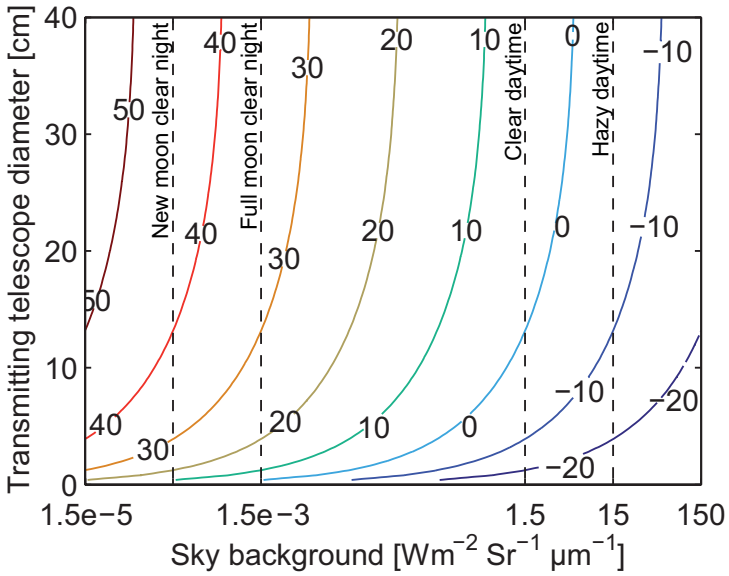

Figure 4.13.: Calculated SNR (in dB) of a satellite down-link over a distance of 500 km as a function of background noise (i.e., ambient condition) and transmitting telescope diameter. The simulation assumes the use of a receiving telescope of $d_R = 1.5$ m diameter with field-of-view 0.016° as used in satellite laser ranging applications and includes experimental data from the etalon filter characterization (section 4.1.1). In first approximation the SNR depends only on the field-of-view and not on d_R, because signal and noise photons change consistently if d_R is changed. The dashed lines show typical sky background intensities for different ambient conditions, the respective values are from reference [135]. Without the added etalon filter during daytime the SNR would always be below zero [46].

advisable to include such a filter in planned space-based QKD setups or long range free-space QKD setups on earth.

In addition to the benefits here, such a filter might be a reasonable addition in situations where the quantum channel is implemented along with a conventional channel on the same fiber or when multiplexed quantum channels are used [144]. Such a shared resource optical network infrastructure would be much more cost effective than dedicated dark fibers for each single quantum channel. However, severe challenges arise because of noise in the quantum channel, e.g., due to spontaneous Raman scattering from the conventional channels. A multi-pass etalon-based filter might be well suited for noise reduction, especially if very narrow-band single photons are used to realize the quantum link.

Part II.

Slowing and Reshaping of Single-Photon Pulses in Atomic Ensembles

5. Towards Photon Storage in Atomic Ensembles

Atomic ensembles are very promising candidates for storage of quantum information. In addition to the single-photon source, a quantum interface between atomic and photonic systems is a significant part of the entire single photon storage experiment. This building block will be described in the following second part of the thesis. The present chapter provides basic concepts of such interfaces **(5.1)** together with a full theoretical description of the particular effect of so-called *electromagnetically induced transparency* (EIT) **(5.2)**. A phased-locked laser system for EIT experiments is introduced **(5.3)** and and some first experimental results are presented **(5.4)** and discussed **(5.5)**. Finally, the EIT effect is used as phase modulator **(5.6)**.

Parts of this chapter (5.3, 5.4) were published in *A robust phase-locked diode laser system for EIT experiments in cesium*, Appl. Phys. B **94**, 429 (2009).

5.1. Quantum interfaces between light and atomic ensembles

Coherent interaction between photons and atoms has attracted much attention over the last decades. The field is of particular relevance since it has been realized, that a collective superposition state of many atoms can be utilized for this interaction. Thus, a large collection of atoms, an atomic ensemble, can be efficiently coupled to quantum light [145]. The simplest situation in which such coupling occurs is, when a particular ground state is mapped onto two different exited states via two optical modes. It was shown almost 15 years ago, that if the optical modes posses quantum entanglement and the light is absorbed by the atomic ensemble, the quantum entanglement can be mapped on a collective superposition of the two final states of the atom [146]. It turned out that not only in this case but for all types of quantum interfaces between atomic ensembles and light known up to now, a large resonant optical depth $d \gg 1$ is the most significant requirement.

Research on coherent interaction between photons and atomic ensembles is motivated on one hand by quantum information processing, where the ability to map quantum states between light and matter is crucial. Proposals and first demonstrations concerned quantum memories as fundamental building blocks of quantum repeaters [17] and photon storage for more advanced quantum networks [18]. Even for short storage times, using atomic systems for storage (e.g., instead of a fiber-based delay line) has the advantage that they are able to provide retrieval on demand. This feature is also utilized in deterministic sources of single photons and entangled photon pairs, that were proposed

and demonstrated previously [17, 70] and that are needed in linear optics quantum computing [24]. On the other hand, tailoring the optical properties of matter by coherent preparation establishes very long optical delay lines [147] and tremendously enhances non-linear coefficients [148].

A gas cell containing alkali atoms at room temperature is one of the simplest atomic ensembles available in the laboratory. Nevertheless, it can work very well as quantum memory. Most of the experiments demonstrated so far utilize a Λ-type level schema in such alkali atoms (see figure 5.1). Typically, a weak probe beam is sent into an ensemble, which is optically pumped by a much stronger coupling beam. If both probe and coupling beam are off-resonant, a coherent Raman transition is introduced in case the two-photon resonance condition is met. On condition that probe and coupling beam are nearly resonant the phenomenon of electromagnetically induced transparency is observed.

5.2. Electromagnetically induced transparency in cesium vapor

5.2.1. Brief review of EIT

Since its first demonstration in 1991 by Harris et al. [63], EIT has attracted much attention, and its capability to slow down [147] and even stop light [66] was shown. In 2001, an EIT based setup for light storage in atomic vapor at room temperature was first demonstrated [71, 65]. Storage times of up to 0.5 ms have been reached. In the meantime, even single photons have been stored in such setups [69], but with shorter storage times on the order of a few μs. EIT can also be utilized for all-optical control of amplitude and phase of a light pulse down to the single photon level. Such a control facilitates loading of single photons into an optical cavity in quantum interfaces [15] or their storage in an atomic ensemble [72]. Cross-phase modulation on the single photon level mediated by EIT [149, 150] is important for establishing optical quantum gates [151]. Both regimes can be described within a common theoretical framework applicable for any Λ-type system [152]. More details will be given in section 5.2.2. Most of the EIT experiments so far have used rubidium atoms [71, 72]. Cesium, however, offers certain advantages, e.g., the $F = 3 \rightarrow F = 4$ hyperfine ground state clock transition allowing the realization of all optical atomic clocks [73]. The ^{133}Cs D1-line at $894\,nm$ (see figure A.1 in the appendix) lies well within the wavelength regime of exciton emission from InAs quantum dots [74], which is relevant for possible coherent interfaces between atomic and solid-state systems [75]. Details of EIT experiments using Cs will be demonstrated in section 5.3.

Very recently, Reim et al. [76] demonstrated coherent storage and retrieval of sub-nanosecond low-intensity (several thousand photons) light pulses with spectral bandwidths exceeding $1\,GHz$ by utilizing a far off-resonant two-photon Raman transition. In this experiment cesium provided the advantage of smaller Doppler linewidth, i.e., ~ 380 MHz in ^{133}Cs compared to ~ 540 MHz in ^{87}Rb at room temperature, and larger hyperfine splitting of 9.2 GHz and 6.8 GHz, respectively. The latter sets a limit to the maximum storage bandwidth. In spite of the potential advantages there have been no experiments so far on the single photon level with cesium vapor, for the most part because of the problem to filter the strong coupling beam. This problem was overcome in

this work, and EIT experiments on the single photon level will be described in the next chapter 6.

5.2.2. Theoretical background

In this thesis the focus is on EIT in cesium vapor in a gas cell at room temperature. The used level schema of the D1-line in ^{133}Cs is Λ-shaped. It is displayed in Figure 5.1 and consists of the two hyperfine levels of the $6^2S_{1/2}$ ground state and of the $6^2S_{1/2}(F = 4)$ level. The two ground state levels $|b\rangle$ and $|c\rangle$ are coupled via dipole-allowed transitions to the common excited level $|a\rangle$ by a coherent coupling field of Rabi frequency Ω and by a weak probe field of Rabi frequency α, respectively.

In case of homogeneous broadening EIT can be achieved if the intensity of the coupling laser is larger than the product of the decay rates of the coherence between the lower level γ_{bc} and the homogeneous linewidth γ. It can be shown, that in case of an inhomogeneous broadened system, e.g., in case of Doppler-broadening relevant for ^{133}Cs at room temperature, EIT can still be achieved if $\Omega^2 \gg \gamma_{bc}\gamma$ [153].

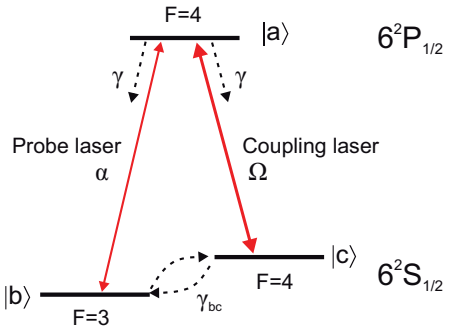

Figure 5.1.: Parts of the ^{133}Cs D1-line form a Λ-shaped three level atomic system. The upper level $|a\rangle$ decays to $|b\rangle$ and $|c\rangle$ with a decay rate γ. The relaxation rate between the lower levels is called γ_{bc}.

Optical Bloch equations The theoretical description of the system is based on the atom-field interaction Hamiltonian

$$H = \hbar\omega_a |a\rangle\langle a| + \hbar\omega_b |b\rangle\langle b| + \hbar\omega_c |c\rangle\langle c| - h\alpha e^{2\pi i\nu_p t} |a\rangle\langle b| - h\Omega e^{2\pi i\nu_c t} |a\rangle\langle c| + \text{H.}c.\,. \quad (5.1)$$

Here, $\hbar\omega_x$ ($x \in \{a, b, c\}$) is the energy of the corresponding atomic level and ν_c and ν_p are the laser frequencies of coupling and probe field. Using the Liouville equation

$$\dot{\rho} = -\frac{i}{\hbar}[H, \rho]$$

time evolution is described. In order to account for incoherent processes like damping or dephasing, one makes use of the master equation formalism including the coupling to

a reservoir in thermal equilibrium [154]. The equations of motion for the density matrix elements in a rotating frame are then given by the optical Bloch equations [155]

$$\begin{aligned}
\dot{\rho}_{ab} &= -\left(i\omega_{ab}+\gamma_{ab}\right)\rho_{ab} + i\alpha e^{-2\pi i\nu_p t}\left(\rho_{bb}-\rho_{aa}\right) + i\Omega e^{-2\pi i\nu_c t}\rho_{cb} \\
\dot{\rho}_{ac} &= -\left(i\omega_{ac}+\gamma_{ab}\right)\rho_{ac} + i\Omega e^{-2\pi i\nu_c t}\left(\rho_{cc}-\rho_{aa}\right) + i\alpha e^{-2\pi i\nu_p t}\rho_{bc} \\
\dot{\rho}_{cb} &= -\left(i\omega_{cb}+\gamma_{bc}+\gamma_{deph}\right)\rho_{cb} + i\Omega^* e^{2\pi i\nu_c t}\rho_{ab} - i\alpha e^{-2\pi i\nu_p t}\rho_{ca} \\
\dot{\rho}_{aa} &= -\gamma_a\rho_{aa} + i\alpha e^{-2\pi i\nu_p t}\rho_{ba} - i\alpha^* e^{2\pi i\nu_p t}\rho_{ab} + i\Omega e^{-2\pi i\nu_c t}\rho_{ca} - i\Omega^* e^{2\pi i\nu_c t}\rho_{ac} \\
\dot{\rho}_{bb} &= -\gamma_{bc}\rho_{bb} + \gamma_{bc}\rho_{cc} + \gamma_{ab}\rho_{aa} - i\alpha e^{-2\pi i\nu_p t}\rho_{ba} + i\alpha^* e^{2\pi i\nu_p t}\rho_{ab} \\
\dot{\rho}_{cc} &= -\gamma_{bc}\rho_{cc} + \gamma_{bc}\rho_{bb} + \gamma_{ac}\rho_{aa} - i\Omega e^{-2\pi i\nu_c t}\rho_{ca} + i\Omega^* e^{2\pi i\nu_c t}\rho_{ac}
\end{aligned}$$

with $\gamma_{ab} = \gamma_{ac} = \gamma + \frac{1\gamma_{bc}}{2}$). Here the following assumptions apply: (1) the decay rates of the transitions $|b\rangle \leftrightarrow |c\rangle$ are equal ($\gamma_{bc} = \gamma_{cb}$), which is generally the case because this decay is determined by the time of flight of the atoms through the interaction region; (2) all other dephasing mechanisms are summarized in the dephasing term γ_{deph} that is later handled as a fit parameter; (3) co-propagating coupling and probe lasers as well as a frequency difference between the transitions ($|a\rangle \rightarrow |b\rangle$) and ($|a\rangle \rightarrow |c\rangle$) that is small enough to ignore the residual Doppler-shift.

Applying the rotating wave approximation [154] a stationary solution of the optical Bloch equations is obtained by assuming $\dot{\rho} \equiv 0$ and normalization $\mathrm{T}r\left(\rho\right) = 1$. In case of a weak probe field the calculations can be limited to the first order in the Rabi frequency of the probe field α. The absorption of the probe field is then governed by the first-order solution of the off-diagonal density matrix element ρ_{ab}. In the steady state this can be found to be

$$\begin{aligned}
\rho_{ab}^{(1)} = & \frac{-i\alpha}{(\gamma_{ab}+i\Delta_{ab})(\gamma_{bc}+\gamma_{deph}+i\Delta_{bc})+\Omega^2}\cdot \\
& \left[\gamma_{bc}+\gamma_{deph}+i\Delta_{bc}(\rho_{aa}^{(0)}-\rho_{bb}^{(0)})+\right. \\
& \left.\frac{\Omega^2}{\gamma_{ac}-i\Delta_{ac})}(\rho_{cc}^{(0)}-\rho_{aa}^{(0)})\right]
\end{aligned} \tag{5.2}$$

with the detuning terms $\Delta_{ab} = (\omega_a - \omega_b) - \nu_p$, $\Delta_{ac} = (\omega_a - \omega_c) - \nu_c$, and $\Delta_{bc} = \Delta_{ab} - \Delta_{ac} = \Delta_{cb}$.

Susceptibility Now, from equation 5.2 the susceptibility can be calculated [156, 157]

$$\chi = \eta\left\{\frac{\rho_{ab}^{(1)}}{\alpha}\right\} \qquad \text{with} \qquad \eta = \frac{3}{8\pi^2}N_{Cs}\gamma_a\lambda_{ba}^3 \tag{5.3}$$

with N_{Cs} being the density of the Cs gas, γ_a the total decay rate of the excited state and $\lambda_{ba} = \frac{c}{(\omega_a-\omega_b)}$ the wavelength of the probe laser transition.

As the experiment is performed at room temperature, Doppler-broadening needs to be accounted for. This can be achieved by convoluting the susceptibility with the velocity

distribution of the moving atoms

$$\chi = \eta \int d(\overrightarrow{v}\,\overrightarrow{k}) f(\overrightarrow{v}\,\overrightarrow{k}) \frac{\rho_{ab}^{(1)}(\overrightarrow{v}\,\overrightarrow{k})}{\alpha} \,. \tag{5.4}$$

The velocity distribution can be approximated by a Lorentzian distribution [153, 158] with the Doppler-linewidth Δw_D

$$f(\overrightarrow{v}\,\overrightarrow{k}) = \frac{1}{\pi} \frac{\Delta w_D/2}{(\Delta w_D/2)^2 + (\overrightarrow{v}\,\overrightarrow{k})^2} \tag{5.5}$$

in order to obtain analytical results for χ. To describe atoms with the velocity $\overrightarrow{v}$, the substitutions $\Delta_{ac} \to \Delta_{ac} + \delta$, $\Delta_{ab} \to \Delta_{ab} + \delta$ and $\Delta_{bc} \to \Delta_{bc}$ with $\delta := \overrightarrow{v}\,\overrightarrow{k}$ are performed in $\rho_{ab}^{(1)}$, and $\rho_{ii}^{(0)}$. Now equation 5.4 can be solved by contour integration in the complex plane.

Using the definition of the complex index of refraction $\tilde{n} = n - i\,\kappa$ with extinction coefficient κ and using $\chi = \tilde{n}^2 - 1$, one finds $\mathrm{I}m\,[\chi] = \mathrm{I}m\,[n^2 - \kappa^2 - 2in\kappa - 1]$. Since $n \cong 1$ in dilute vapor, $\mathrm{I}m\,[\chi] \cong -2\kappa$ follows, which allows the transmission T to be calculated using the absorption coefficient $\alpha_{EIT} = \frac{2\pi}{\lambda_{ba}} \mathrm{Im}\,[\chi]$ [101] and the length of the gas cell L_{Cs}

$$T = e^{-\alpha_{EIT} L_{Cs}}. \tag{5.6}$$

It can be further shown, that the width of the transparency window is scaling with $\Delta\nu_{EIT}^{Dopp} \sim \Omega^2/\Delta w_D$ in the case of Doppler broadening instead of $\Delta\nu_{EIT} \sim \Omega^2/\gamma_a$ for a gas at absolute zero temperature [155].

According to reference [159] dispersive properties like the index of refraction

$$n \sim \mathrm{R}e\,[1 + \chi]\,^1 \tag{5.7}$$

or the group velocity

$$v_g = \mathrm{R}e \left[\frac{c - \nu \frac{\partial(1+\chi)}{\partial k}}{(1+\chi) + \nu \frac{\partial(1+\chi)}{\partial \nu}} \right]$$

can be calculated. The first summand in v_g accounts for frequency dispersion, the second is attributed to spatial dispersion. Experimentally, the EIT caused pulse delay in Cs τ_{EIT} cell will be studied,

$$\tau_{EIT} = L_{Cs} \left(\frac{1}{v_g} - \frac{1}{c} \right) . \tag{5.8}$$

The dependence of absorption and index of refraction on probe laser detuning is simulated in figure 5.2 using equations 5.6 and 5.7. In the figure the solid line gives the situation for a coupling laser of Rabi frequency $\Omega = 0.5$ MHz while the dashed line shows the situation without a coupling laser for reference. Figure 5.2(a) shows the absorption coefficient, the transparency window is visible only in the presence of the

[1] Due to the definition of the Rabi frequencies no additional factor 2π is required.

coupling laser. Figure 5.2(b) exhibits the corresponding index of refraction with a steep slope if the coupling laser is applied.

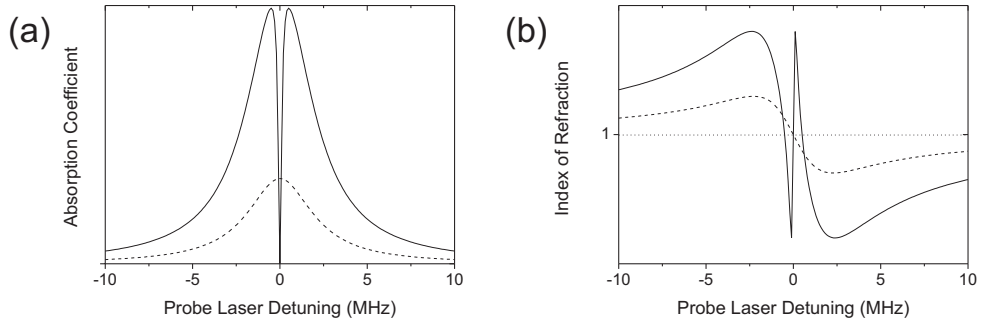

Figure 5.2.: (a) Absorption and (b) index of refraction around the probe laser transition. The absorption shows the typical feature of high transmission on resonance while the index of refraction exhibits a steep slope as required for low group velocities. The dashed lines show the situation without coupling laser for reference.

5.3. Laser source for EIT experiments

Several parts of the whole experiment have been described already in previous chapters. The master laser for the EIT experiment is the same as for single-photon generation, here it is used as probe laser. However, another external-cavity diode laser (Toptica DL100) is needed as coupling laser for EIT. This second laser employs also a Littrow configuration [97, 98] to reach an intrinsic linewidth of a few 100 kHz and provides around 20 mW of single-mode output power. Consistent with the ^{133}Cs D1-line the two lasers operate at around 894 nm. To obtain a stable frequency reference for the whole experiment, the master laser is again stabilized to the $6^2S_{1/2}(F = 3) \rightarrow 6^2P_{1/2}(F' = 4)$ hyperfine transition by Doppler-free frequency modulation spectroscopy (FMS), as described in detail in section 3.2.1. To stabilize the coupling laser wavelength relative to the master (probe) laser, an optical phase-locked laser system was built.

5.3.1. Optical phase-locking

Optical phase-locked laser systems have been studied for many years. Pioneering work was done in the 1960s using He-Ne lasers [160, 161] and was considerably extended in the 1980s [162]. Phase-locking of Nd:YAG lasers can today be realized routinely with a very low residual phase-noise in the order of 1 μrad [163]. However, phase-locking of diode lasers requires significantly more effort. Due to their high reliability and low cost diode lasers are favorable, especially when lasers operating at a particular wavelength, like an atomic resonance frequency, are needed. The quality of the phase-lock of two

lasers propagating in a medium limits the degree of coherence prepared. Besides the EIT experiment described here, coherence is required for many other novel applications ranging from coherent beam combining [164] to atom interferometry [165].

Generally speaking, an optical phase-locked loop (OPLL) consists of an optical slave oscillator (laser), whose output is phase-compared with the output of a master oscillator (laser) by a phase detector. The phase detector's output is proportional to the phase difference between the two oscillators. This phase-error signal is low-pass filtered and used to control the frequency modulation of the slave oscillator. In a heterodyne OPLL the phase difference of two lasers with different wavelengths is locked to a stable reference phase from a local oscillator. Therefore, the heterodyne OPLL is often called frequency offset-locked loop.

Although several descriptions of phase-locked laser systems can be found in the literature, these systems often have special features, for example tens of gigahertz scanning range [166], that make them over-engineered for an application where just two fixed or only minor tunable wavelengths are required. Other implementations often use a combination of digital and analog phase detectors [167] leading to more complex systems and more potential sources of phase-noise.

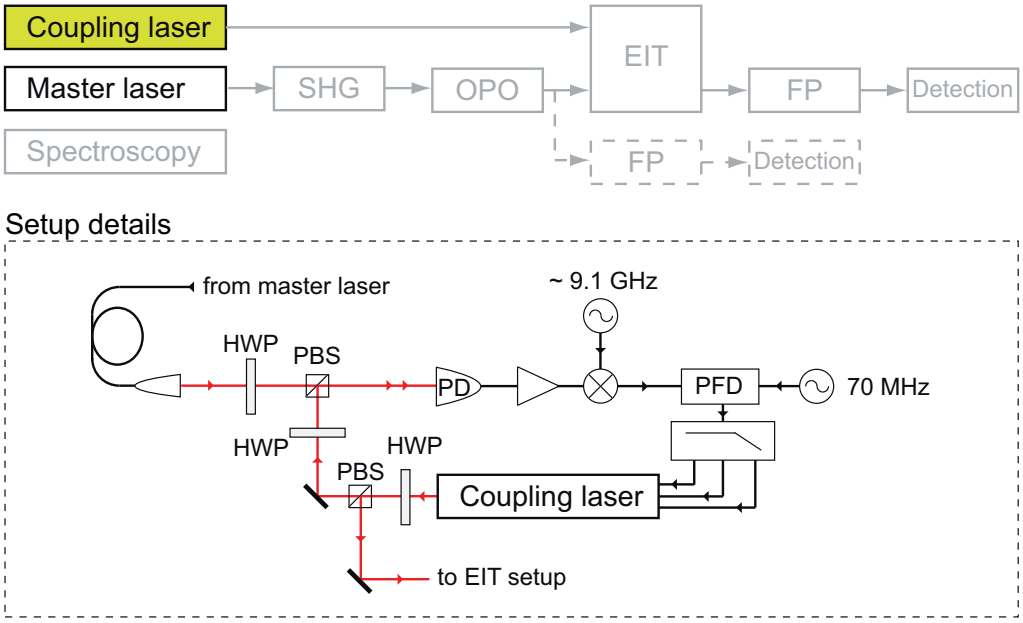

Figure 5.3.: The probe laser (master) is stabilized using a frequency modulation spectroscopy (FMS) setup. An OPLL locks the coupling laser to the probe laser: Both lasers are superimposed on a fast photo diode (PD), the beat-note is amplified and mixed down with a microwave signal source. A phase frequency detector (PFD) detects the phase difference between the beat-note and another 70 MHz local oscillator. This phase error signal is used to control the coupling laser using a 3-path feedback loop.

In order to provide a stable coupling laser resonant with the $6^2S_{1/2}(F = 4) \rightarrow 6^2P_{1/2}(F' = 4)$ hyperfine transition (see figure 5.1) and minimal phase fluctuations between coupling and probe laser, the coupling laser is offset frequency-locked to the probe laser with a frequency offset of exactly 9.19263177 GHz, which represents the frequency splitting between the $6^2S_{1/2}(F = 3)$ and $6^2S_{1/2}(F = 4)$ energy level in ^{133}Cs. As shown in figure 5.3, around 1 mW of power is split off of both lasers and is superimposed on a fast photo diode (Alphalas UPD-IR2, bandwidth 10 GHz) to generate the beat-note frequency between the two lasers. This signal is amplified by 50 dB using two GaAs 18 GHz amplifiers (DA-LightCom) and mixed down using a $\sim$ 9.12263177 GHz local oscillator (Work SSG-10) and a fast mixer (Mini-Circuits ZMX-10G). Part of the mixer's output signal is used to monitor the beat-note with a spectrum analyzer. The main signal feeds a digital phase/frequency detector after a 190 MHz low-pass and amplification by another 25 dB (MiniCircuits ZFL-500). The detector (Hittite HMC439QS16G, available in a small module with matched I/O signal lines) has an ultra-low single-sideband phase-noise of -153 dBc/Hz@10 kHz and $0.01 - 1.3$ GHz input frequency. It generates a 2 V_{pp} output signal representing the actual phase difference between its two input ports. A second 70 MHz local oscillator (Novatech Instruments DDS409A) is used as a reference and is connected to the second input port. The two oscillator frequencies sum up to the exact frequency difference between the $6^2S_{1/2}(F = 3)$ and the $6^2S_{1/2}(F = 4)$ energy level. All oscillators are electronically phase-locked to a 10 MHz reference signal produced by a low-noise analog signal generator (Agilent E8257D), which leads to an absolute accuracy of the order of 10^{-8} for the reference signal, i.e., $\sim$100 Hz for the total offset frequency. This value could easily be decreased if necessary with a better frequency standard, e.g., by using a GPS disciplined oscillator.

5.3.2. Filter electronics

Several filters are used to close the feedback loop and control the coupling laser frequency by the phase-error signal. Three feedback paths are combined to compensate for slow, medium, and fast laser frequency fluctuations. The slow feedback path is established using a piezoelectric actuator that tilts the diffraction grating inside the laser head. The path has a bandwidth of around 1 kHz and is capable of compensating for slow frequency fluctuations and drifts. The medium and fast feedback paths both modulate the injection current of the laser diode. Injection current modulation leads to carrier density modulation and temperature change effects that induce frequency modulation. The medium path uses a field-effect transistor mounted parallel to the laser diode to modulate the current. Depending on the modulation signal a part of the DC current bypasses the laser diode. The bandwidth of this path is several MHz, and it allows current changes in the order of 2 mA leading to frequency changes in the order of several GHz. The fast path uses a Bias-T to directly modulate the diode current. Its electronic bandwidth reaches from $\sim$300 kHz up to over 100 MHz, although the modulation depth considerably decreases for higher frequencies above a few MHz [168]. Still, this path allows to compensate for very fast frequency fluctuations with small amplitudes. Simulations show that the phase error variance σ_ϕ^2 is approximated by the sum of the

linewidths $\Delta\nu_M$ and $\Delta\nu_S$ of the master and slave laser divided by the feedback loop noise bandwidth [169]

$$\sigma_\phi^2 = \frac{2(\Delta\nu_M + \Delta\nu_S)}{B_w} \,. \tag{5.9}$$

The combined linewidth of the two lasers is of the order of 500 kHz. Therefore, to reach an aimed phase error variance $\sigma_\phi^2 < 0.1$ rad^2, a minimum feedback loop noise bandwidth of $\sim$10 MHz is required.

Figure 5.4 shows an overview of the electronic realization of the phase detector and the loop filters together with the relevant filter parameters and the approximate overall attenuation of each path, which proved to be sufficient for our laser system. The indicated parameters depend on the characteristics of the specific laser system, Bias-T, and supporting electronics.

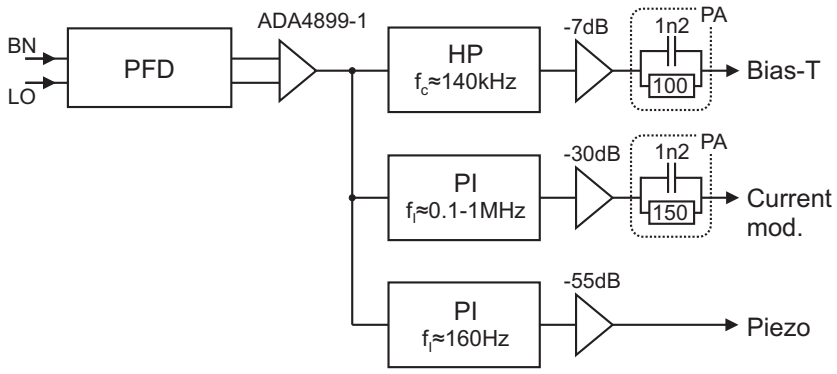

Figure 5.4.: The phase/frequency detector (PFD) compares the amplified beat-note signal (BN) and the local oscillator frequency (LO). Its output is used to drive three feedback paths via appropriate loop filters. The loop filters consist of a high pass (HP), two flexible proportional integral filters (PI), several amplifiers/attenuators and two simple phase advance circuits (PA).

The filters in the medium and fast path were built with LMH6702 operational amplifiers, the slow path uses an LF444 operational amplifier. It proved very useful to have decoupled controller parameters, i.e., decoupled gains of the proportional and integral terms [170]. The medium and fast paths are impedance-matched to 50 Ohm, and all cables are kept as short as possible to reduce delays.

5.3.3. Phase-lock performance

To characterize the OPLL the spectrum of the beat-note signal between the coupling and probe laser was measured, as shown in figure 5.5.

As discussed above, the performance of the feedback system is given by the phase-noise variance of the OPLL. This can be calculated from the fraction of power contained

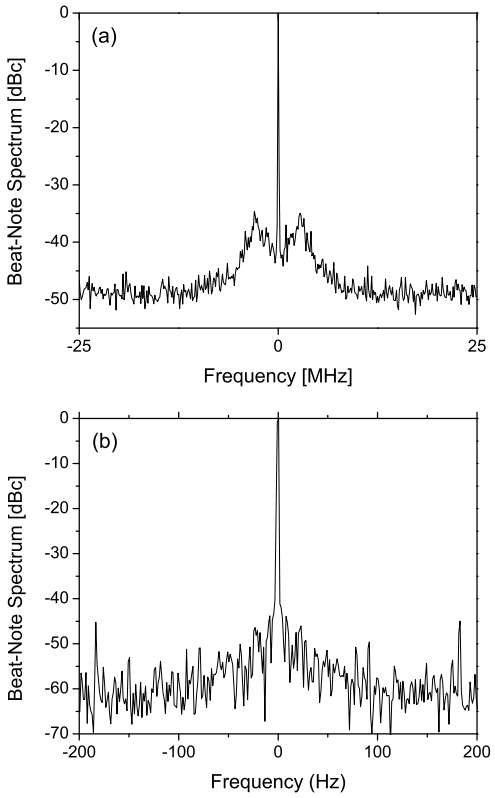

Figure 5.5.: (a) Measured beat-note between the phase-locked probe and coupling laser (resolution/video bandwidth=10 kHz). (b) Detail around the beat-note (resolution/video bandwidth=1 Hz).

in the beat-note signal [171] with

$$P_{total} = \int_{-\infty}^{\infty} P(\omega) d\omega \tag{5.10}$$

being the integrated power spectral density over all frequencies and $P(0)$ the power contained in the beat-note signal. Following the procedure outlined in reference [171] using the auto-correlation function of the electrical field and the Wiener-Khintchine theorem, it can be shown that

$$\frac{P(0)}{P_{total}} = exp(-\sigma_{\phi}^2). \tag{5.11}$$

As depicted in figure 5.5 (a), this fraction was measured to be 98.4%, i.e., a residual phase-noise variance of $\sigma_{\phi}^2 < 0.02$ rad^2 was achieved including the contribution of

the local reference oscillator. This result is comparable or better than the previous realizations [167, 166], although a digital-only phase detector was used.

5.4. First EIT experiments

In order to test the laser system and the agreement between theoretical simulation and experiment, a first EIT setup was built using macroscopic probe powers, as shown in figure 5.6.

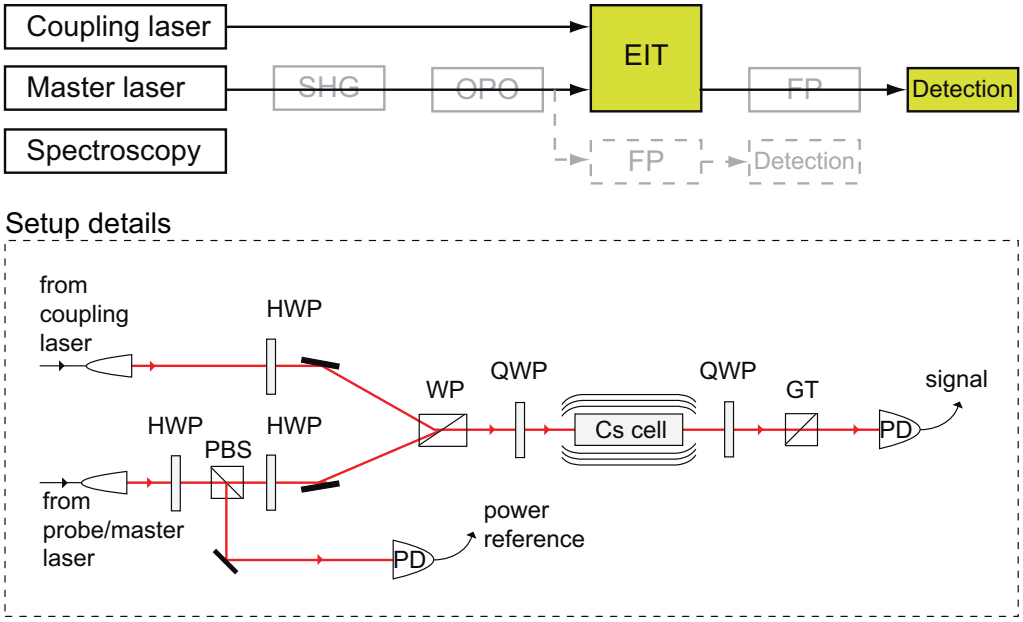

Figure 5.6.: First EIT setup. Coupling and probe laser are polarized and superimposed by a Wollaston prism (WP). The polarization is changed to circular and both lasers co-propagate through a magnetically shielded Cs cell. After the polarization is transformed back to linear, a Glan-Thompson prism (GT) filters the coupling beam behind the cell. Two photo detectors (PD) detect the signal after the cell and the reference level.

Probe and coupling laser are both mode-cleaned by single-mode optical fibres, subsequently superimposed and orthogonally linear polarized by a high quality Wollaston prism. A quarter-wave plate (QWP) switches from linear to left and right circular polarization of the coupling and probe, respectively. Both lasers co-propagate through a 4 cm long glass cell of diameter 25 mm containing 99.99% isotopically pure ^{133}Cs. The number of interacting cesium atoms at a given temperature can be calculated via the vapor pressure curve [157] and the beam waists in the respective measurement. In order to minimize losses and the formation of parasitic etalons, the end facets of the gas cell are AR coated for 894 nm. The cell is shielded against external magnetic fields, mainly earth's magnetic field, by 3 layers of μ-metal in order to suppress level shifts and de-

coherence between the hyperfine ground states. The particular shield design attenuates DC magnetic fields by a factor of $\sim 2 \times 10^5$[172] resulting in a very small and negligible residual line shift of ~ 3.5 Hz per Gauss [157], i.e., around 1 Hz due to earth's magnetic field. Heating foil wrapped around the cell together with a homemade temperature controller (based on a WTC3243 chip) allows to adjust the cell temperature between 25-80 °C. The long-term temperature stability was measured to be ±10 mK over 10 h.

Behind the Cs cell a second QWP transforms the polarization back to linear, and the coupling laser is filtered by a Glan-Thompson prism. The two QWPs were produced at the same time from the same piece of material which allows one QWP to compensate for slight manufacturing inaccuracies of the other. Eventually, this setup reaches a rejection of the coupling laser by 10^{-6} before detection. The probe laser is detected by a homemade PIN diode-based DC coupled photo detector.

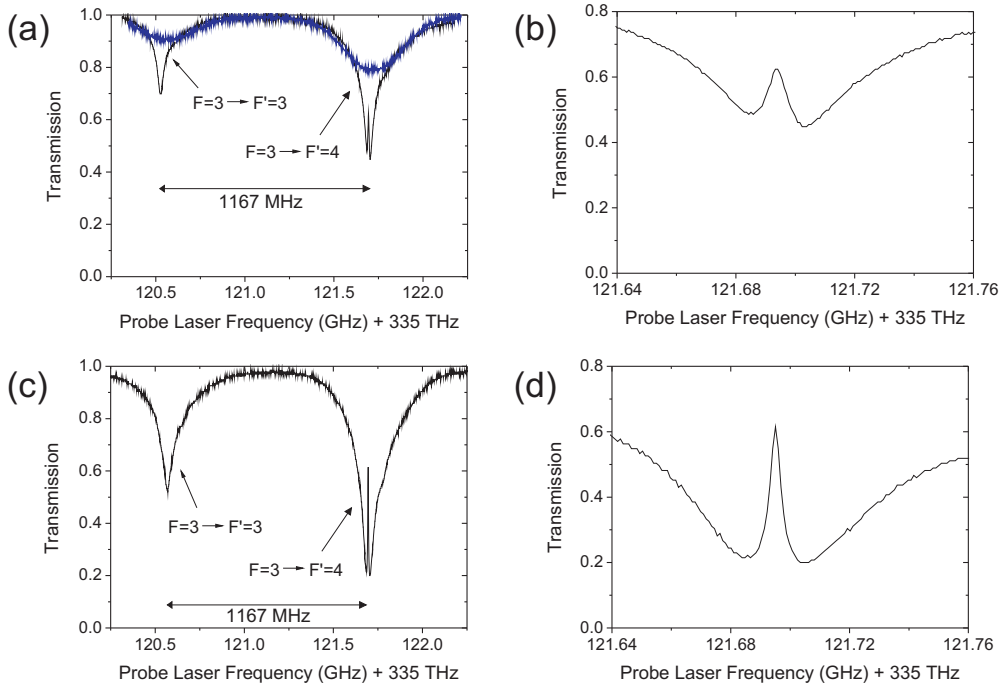

Figure 5.7.: Full scans across the probe laser resonance on the cesium D1 line without frequency offset look. (a) Absorption (blue) and EIT spectrum (black) before optimization and probe laser transmission for reference. (b) Zoom into the EIT peak. (c) Corresponding measurement after optimization of relevant beam parameters. (d) Zoom into the improved EIT peak.

As first pre-study the EIT spectrum was obtained using this setup but without the frequency offset lock for laser stabilization. Instead, this time the coupling laser was itself frequency locked to the $6^2S_{1/2}(F = 4) \rightarrow 6^2P_{1/2}(F' = 4)$ hyperfine transition in the D1-line of ^{133}Cs using the FMS. The probe laser was scanned by its external-cavity

piezo across the $6^2S_{1/2}(F = 3) \rightarrow 6^2P_{1/2}(F' = 4)$ transition. This is the only possible measurement in this setup that shows the full well-known EIT spectrum, see figure 5.7. Later measurements always use the frequency offset lock to optimize the results through the use of phase-locked lasers, which, however, prevents such wide scan ranges as the frequency offset lock is optimized for stability and for narrow scan ranges only.

The figures 5.7(a) and (b) provide a first visual proof of EIT with the characteristic transparency window on the proper hyperfine line. After optimizing the parameters of the two beams, namely polarization, beam profile matching, and collinearity, the EIT transparency increased from only 0.32 to 0.52, as shown in figures 5.7(c) and (d).

To study EIT in detail and verify the theoretical description from section 5.2.2, the laser configuration was changed and the frequency-stabilized and phase-locked lasers were now used as coupling and probe laser. Two consecutive acusto-optical modulators (AOMs) were utilized to scan the probe laser across the transition frequency without loosing frequency stability. The two AOMs (Isomet 1205C) have a resonance frequency of 80 MHz. Both are used in double-pass configuration allowing a scan range of ±20 MHz with intensity changes <10%. The application of two AOMs allows to scan around zero detuning, i.e., one AOM is configured to increase the laser frequency, the other to decrease it, which is necessary as the laser stabilization frequency and the EIT center frequency are the same. To compensate for the remaining intensity changes due to the AOMs, a reference detector in front of the EIT experiment is used to calibrate each measurement. A multi-channel arbitrary waveform generator (Novatech Instruments DDS409A) controls the two AOMs, and the whole experiment is computer controlled. This allows to construct the EIT spectra step-by-step from hundreds of consecutive measurements, each with an exactly adjusted probe laser frequency.

As a first test, the probe laser was scanned by ±20 MHz around the $F = 3 \rightarrow F' = 4$ transition while the wavelength of the coupling laser was locked via frequency offset lock to the $F = 4 \rightarrow F' = 4$ transition. A probe laser power of 100 μW with a beam diameter of ∼0.8 mm was used. The coupling power was 4 mW with ∼2 mm beam diameter. The transmission signal was normalized without ^{133}Cs frequency stabilization by a ∼600 MHz detuned probe laser outside the Doppler-broadened transition. Several scans of the probe laser across the ^{133}Cs resonance were performed. Figure 5.8 shows the results for different cell temperatures. The theoretical fits calculated using equation 5.6 are in excellent agreement, and it should be pointed out that the dephasing rate is the only fit parameter because γ_{ab} and γ_{ac} are set to the spontaneous emission rate of the Cs D1-line [157]. The coupling laser wavelength is assumed to be exact, i.e., $\Delta_{ac} = 0$, and the decoherence rate is determined by time-of-flight broadening due to atoms moving in and out of the coupling laser beam. It can be calculated using the Maxwell-Boltzmann velocity distribution

$$\gamma_{bc} = \frac{\sqrt{2k_B T_{Cs}/M_{Cs}}}{4\pi w}\,. \tag{5.12}$$

Here, M_{Cs} denotes the mass of a cesium atom, T_{Cs} the temperature and w the mean beam waist inside the cell. The dephasing rate is found to be γ_{deph} = 75-110 kHz, as indicated in figure 5.8. As expected, with increasing temperature and Doppler broadening

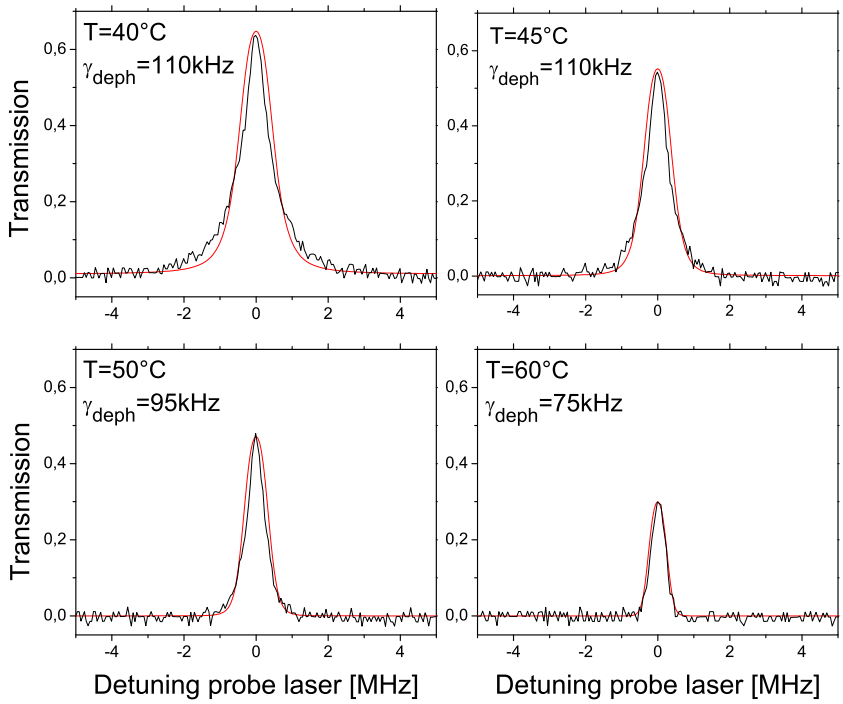

Figure 5.8.: Scans across the probe laser resonance for cell temperatures between 40 and 60 °C. Measurements (black) are compared to theoretical fits (red curves), where the dephasing rate γ_{deph} is the only fit parameter.

the width of the transparency window drops and at the same time the opacity increases due to higher cesium density.

5.5. Discussion and short summary

EIT on the cesium D1 line in atomic vapor with macroscopic probe power was demonstrated. At first, an appropriate phase-locked laser system was described and the relevant performance parameter, namely the residual phase-noise variance studied. With a phase-noise variance of $\sigma_\phi^2 < 0.02$ rad^2 the system was found to be comparable or better than the previous realizations described in the literature [167, 166]. In elementary EIT studies it was then shown that the measured parameters of the EIT transparency window are in excellent agreement with a theoretical approach based on a single free parameter only. This parameter γ_{deph} accounts for pure dephasing between the two hyperfine ground states and is found to be $\gamma_{deph} = 75$-110 kHz in this setup. There is a trend of decreasing γ_{deph} with higher cell temperatures which might be further investigated. The FWHM of the transparency window is found to be 0.5-1 MHz. The experiment shows the suitability of both, the theoretical description and the experimental setup for further

and more advanced EIT experiments. All further experiments and simulations will be based on these studies as the theoretical framework remains valid for ultra-low probe intensities also.

5.6. EIT as phase modulator

In the EIT cell an amplitude modulation of the strong coupling field is transferred to the weak, possibly single-photon probe field. Single-photon probe beam amplitude modulations will be experimentally shown in chapter 6, but the modulation transfer in general is also an outcome of the theoretical treatment in section 5.2.2. Besides an amplitude modulation of the probe, the EIT effect will also result in a cross-phase modulation. Some preliminary studies were performed in order to investigate the influence of the coupling laser on the probe laser phase under EIT conditions. To allow phase measurements the experimental setup from figure 5.6 was extended by a Mach-Zehnder interferometer around the EIT cell, as shown in detail in figure 5.9.

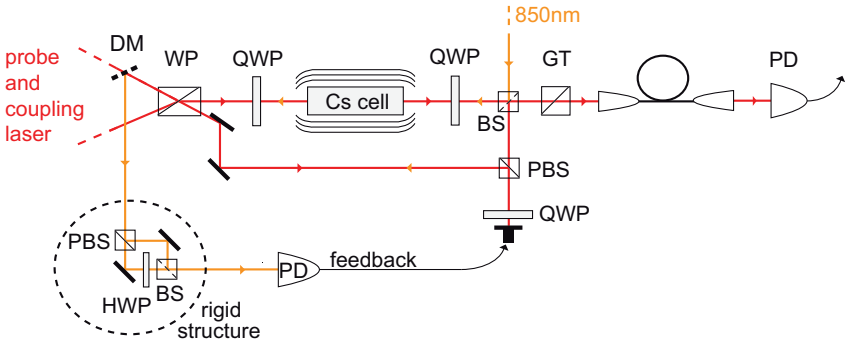

Figure 5.9.: Details of the setup for EIT phase measurements. The Mach-Zehnder interferometer is stabilized by a counter-propagating auxiliary 850 nm laser using a dichroic mirror (DM) and a feedback loop with piezoelectric elements in one arm. The dashed line encloses a rigid setup of polarizing optics to close the Mach-Zehnder interferometer and obtain an interference signal for active arm-length stabilization, see text for more info. A single-mode fiber in front of the photo detector ensures spatial mode matching of probe and reference beam in order to increase the interferometer's visibility.

In front of the EIT cell the probe laser is split into two components, one passes the EIT cell and the other is used as phase reference. The interferometer is actively stabilized using a mirror mounted on a piezoelectric element in the reference arm and a counter-propagating auxiliary laser at 850 nm, i.e., far off-resonant from the coupling and probe transitions. The auxiliary laser light was produced using another external-cavity laser system (Toptica DLpro) with a typical linewidth of only 100 kHz and very low drift due to ambient temperature changes ($\ll$ 100 MHz/K) and good isolation against acoustics and vibrations. As a result of the particular experimental configuration needed for the

EIT effect, the auxiliary laser leaves its output port of the interferometer with different polarization of its two parts which traveled the probe and the reference arm. Thus, in order to measure interference some further optical components are required to separate these two superimposed beams, change one beam's polarization and superimpose them again in front of a photodiode. To ensure that virtually no arm length fluctuations occur in this part of the beam path, all optics are integrated in a small rigid aluminium structure of ~ 30 mm diameter. Using this configuration, arm length fluctuations of the probe or reference arm directly result in changes of the interference signal detected by the photodiode.

At first, the Mach-Zehnder interferometer itself was checked. Therefore, without the EIT cell in place the reference arm of the interferometer was linearly scanned and the interferometer visibility was studied by monitoring the probe laser interference at its output port. As shown in figure 5.10, the visibility is very good, it was found to be > 0.98.

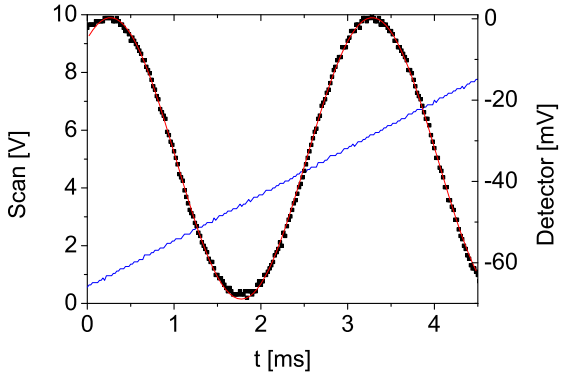

Figure 5.10.: Scan of the reference arm in the Mach-Zehnder interferometer. The blue line shows the applied scan voltage, the black dots the measured interference and the red curve a fitted sinus curve. The visibility is > 0.98.

Now, for EIT cross-phase modulation measurements the reference arm-length was actively stabilized using the auxiliary laser interference signal as reference. With active stabilization the probe laser interference signal was found to be virtually constant. The EIT configuration was established by adjusting coupling and probe laser frequency to match their respective transitions while a continuous wave probe beam of 20μW and 2 mW coupling power was used. Behind the EIT cell the superimposed probe and reference signal was detected by a fast, low-noise photo detector (Hamamatsu C4777). The EIT cell was operated at 54° C in order to increase the EIT transmission modulation amplitude, albeit at the cost of lower overall transmission. Figure 5.11 (A) shows the intensity at one output of the Mach-Zehnder interferometer under resonant EIT conditions. A pronounced temporal intensity fluctuation is apparent. This fluctuation is only present if the EIT cell is in place and a resonant coupling beam is present, as several test measurements proved.

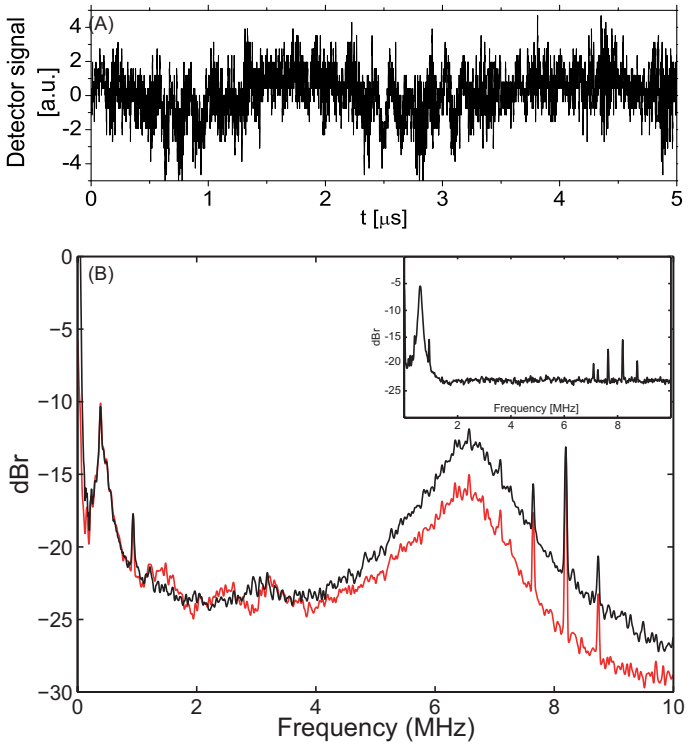

Figure 5.11.: (A) Interference signal of the probe laser measured at one output of the Mach-Zehnder interferometer (see figure 5.9) under resonant EIT conditions. (B) Comparison of the Fourier transform of the signal in (A) (red curve) with the normalized Fourier transform of the direct beat-note signal between the coupling laser and the stabilized probe (black curve). The beat note signal was obtained by down-mixing via a local oscillator of ≈ 9.2 GHz. A common broad spectral feature (see text) between $5\,MHz$ and $7\,MHz$ is clearly visible. For comparison, the inset shows the normalized Fourier transformation of the direct beat-note signal of the probe laser with itself. The sharp features at 385 kHz and 930 kHz and at 7, 7.6, 8.2, 8.7 MHz are attributed to the laser frequency stabilization electronics.

In order to gain further insight a Fourier transformation of the measured intensity fluctuation signal was performed, which is shown as red curve in figure 5.11 (B). As reference, a beat-note signal between the coupling laser and the stabilized probe laser was measured using direct detection by a 10 GHz photo diode and down-mixing via a local oscillator of ≈ 9.2 GHz. Its Fourier transformation is plotted as black curve in figure 5.11 (B). The data for the red and for the black curve were recorded simultaneously using two channels of a digital storage oscilloscope with 20M samples record length. Thereafter, the Fourier transformation was performed on both data sets individually.

It is apparent that both signals almost overlap, apart from a linear decline of the red curve towards higher frequencies, which suggests a 3 dB bandwidth of 10 MHz for the modulation observed in figure 5.11 (A). In particular, a characteristic broad frequency component between $5\,MHz$ and $7\,MHz$, which reflects a side-band produced by the loop-filters in the phase-lock electronic, occurs in both curves. This measurement shows that there is cross-phase modulation between the coupling and the probe laser [173], as this characteristic broad frequency component is not present on the probe beam before it passes the EIT cell, which is proven by a test measurement shown in the inset of figure 5.11 (B). Here, the beat-note signal of the probe laser with itself is shown. It was measured at the output of the Mach-Zehnder interferometer with the EIT cell being removed, the characteristic frequency component between $5\,MHz$ and $7\,MHz$ is absent. With a blocked coupling beam in front of the EIT cell the modulation is also not present.

It is important to note that the cross-phase modulation between coupling and probe laser cannot be achieved by electronic modulation, e.g., by detecting the coupling laser and feeding this signal on an EOM to modulate the probe field. However, a coherent modulation mediated by EIT is required.

5.7. Discussion and short summary

Cross-phase modulation between coupling and probe laser was observed. Due to the coherent nature of the modulation also non-classical correlations, e.g., as present in a squeezed pump beam, can be transferred to the probe beam. Cross-phase modulation is thus a possible tool to transfer quantum correlations between strong light beams and weak beams, possibly single photons. Cross-phase modulations were proven through a characteristic frequency component caused by the phase-locking electronics which modulated the coupling laser. Without EIT, this frequency component is present on the coupling beam only, but it is visible as phase-modulation on the probe beam behind the EIT cell as soon as the EIT effect occurs. Although selective and controlled phase manipulations were prevented in these first experiments by the superimposed noise modulation on the coupling beam, this can be overcome by a more stable laser source [174, 175]. In addition, using AOM [176] or EOM generated coupling laser sidebands as probe field and a selective coupling beam modulation in front of the EIT cell instead of the two separate phase-locked lasers might be a reasonable enhancement for this experiment. A fast active coupling laser amplitude fluctuation compensation, e.g., by using another AOM, might also be needed.

Whereas cross-phase modulation between weak, possibly single-photon fields were already discussed and demonstrated [149, 177, 150], it might also be possible to utilize cross-phase modulation between a stronger coupling field and a weak, possibly single-photon field. Possible applications may concern transfer of quantum correlations between quadrature components of two strong beams to correlations between a quadrature component of a strong beam and the phase of a single photon. An example would be to use one arm of two entangled beams as coupling laser in an EIT configuration and to map its amplitude fluctuation on the phase of a single photon using a Mach-Zehnder

interferometer in the same way as shown in figure 5.9. Except for an additional detector in the second arm of the interferometer the setup is similar to the one used by Lobino et al. [178] for quantum tomography of a light pulse stored in ^{87}Rb vapor. In that paper an extra noise component of the stored and retrieved state was attributed to the population exchange between atomic ground states of the EIT Λ-system while the light was stored and the coupling field was switched off. Here, the effect of the coupling field itself on the probe field was analyzed, and a combination of the two experiments is certainly aspired.

6. Single Photon EIT Experiments

In the previous chapter 5 the concept of EIT and basic experiments used to evaluate the setup were demonstrated. In this chapter the study of EIT will be extended to the single-photon regime. The challenging task of coupling beam suppression is discussed and an EIT setup capable of working with a single-photon probe beam is introduced **(6.1)**. Subsequently, EIT with pulses on the single photon level are studied **(6.2)**. The results presented here are the first published EIT measurements in Cs vapor on the single photon level.

Parts of this chapter were published in *Electromagnetically induced transparency in cesium vapor with probe pulses on the single photon level*, Phys. Rev. Lett. **105**, 153605 (2010).

6.1. Coupling beam suppression

In spite of the potential advantages of cesium compared to rubidium, there have been no EIT experiments on the single photon level with cesium vapor, mostly because of the problem to suppress the strong coupling beam. To allow detection of the probe pulses on the single photon level while using a coupling laser power of a few mW, the coupling laser needs to be suppressed in front of the probe detector by almost 12 orders of magnitude. This is not possible with polarization filtering alone, as was done for the experiments in chapter 5. Even with the very high quality polarization optics used there, i.e., a Wollaston prism as polarization adjuster, two matched quarter-wave plates and the Glan-Thompson prism as filter, the combined suppression of the coupling beam was not higher than 55 dB. Although spatial filtering of the coupling beam by non perfect overlap of probe and coupling beam can be supplemented, this is by far not enough. Even for counter-propagating beams, as measured already in section 4.2, the remaining noise on the probe detector is much too high and it would even be higher in the EIT configuration with co-propagating beams. Therefore, spectral filtering is additionally required even though probe and coupling beam are only separated by 9.2 GHz. In fact, all three filter stages need to be combined, as shown in figure 6.1.

Supplementary to the already existing EIT setup spatial filtering with a single-mode fiber and the triple-pass planar Fabry-Pérot etalon was employed. This etalon was presented already in chapter 4. It has a measured peak transmission of 65% and a suppression of off-resonant light by 46 dB. Due to the FSR of 17.4 GHz, the coupling laser wavelength lies very well in between two transmission peaks which guarantees optimal suppression. The coupling beam has a center frequency of approximately 335 THz, hence the frequency difference between coupling and probe beam is only $< 0.003\%$ (~ 9.2 GHz).

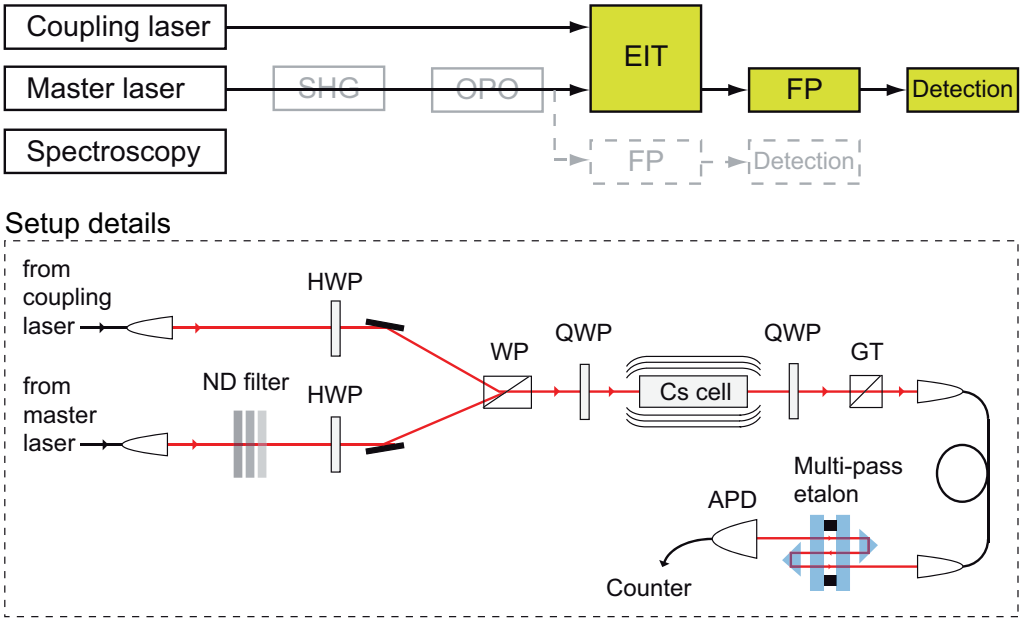

Figure 6.1.: Setup for EIT experiments with a probe beam on the single photon level. The setup from chapter 5 is extended by spatial filtering and the triple-pass planar Fabry-Pérot etalon presented in chapter 4. In addition, several neutral density (ND) filters are used to reduce the probe beam intensity in front of the EIT cell. The probe detection is performed by an APD.

Nevertheless, the multi-pass etalon allows an extremely large suppression of the coupling beam and thus makes single photon experiments possible. The contrast of the etalon filter is $10-15$ dB better than that of other ultranarrow bandpass filters of comparable peak transmission [114]. Also, the FWHM of the passband is much narrower than most other filters. In addition, the etalon based filter is very flexible and adaptable to the particular task. For example, filters based on absorption of an atomic transition, that are often used in single photon experiments in combination with atomic systems [69], are very narrow-band and have good transmission too but lack fast and easy tunability. Furthermore, they are only available for a particular wavelength corresponding to the specific atomic level schema. There is no suitable atomic system available for experiments based on cesium, but only for experiments using rubidium.

In in our experiment the probe beam is attenuated by several orders of magnitude in front of the EIT cell. Instead of a photo diode, a single-photon counting avalanche photo diode module (APD) is used as detector behind all filters. The APD was placed in a fully stray light isolated box which is connected free-beam to the output of the etalon. The etalon itself is also fully isolated from stray light, and the beam is coupled into the etalon by a single-mode fiber. Taken together, this reduces the detector dark counts to 100 counts/s which is the intrinsic dark-count level of the used APD.

6.1.1. EIT with ultralow probe power

As first test of the setup, a frequency scan of the probe laser over the EIT resonance was performed in the same way as in chapter 5, i.e., by modulation of the probe laser wavelength using two consecutive acousto-optic modulators (AOMs) in double-pass configuration and thus by computer controlled wavelength scanning. The measurement is shown in figure 6.2, the characteristic EIT transmission peak is apparent.

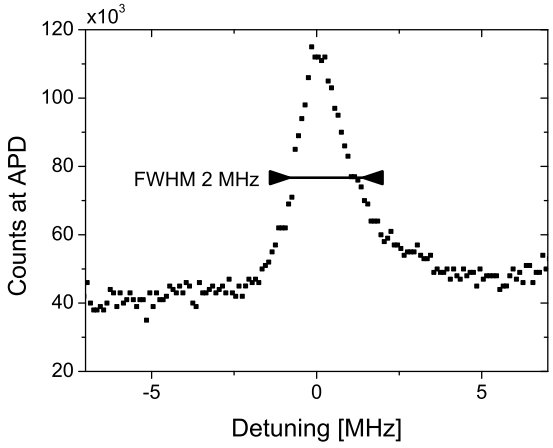

Figure 6.2.: Probe laser scan around the EIT resonance with ultralow probe laser intensity. The EIT transmission peak is clearly visible. Background, due to coupling laser photons that were scattered into the probe mode (around 90×10^3 counts/s), is subtracted from the raw data (see text).

For this measurement the probe laser power was attenuated to ~ 350 fW. The coupling laser power was 2.2 mW, and the coupling laser was phase-locked using the offset frequency locking electronics described in section 5.3. The detector counts were integrated for 100 ms. Before the scan was performed the multipass-etalon filter was adjusted without the EIT cell and the coupling beam for maximum probe laser transmission. As the FWHM of the etalon is 165 MHz, the etalon transmission remains mostly constant if the probe laser is scanned for $\pm < 20$ MHz, as in this measurement. However, the noise level is rather high and the quality of the measurement with a continuous wave probe light therefore limited. Nevertheless, this experiment proves the outstanding performance of the combined filters for coupling beam suppression and their applicability for EIT experiments with ultralow probe intensity. From the coupling beam alone, i.e., without Cs cell being present and without the probe laser, 15×10^3 counts/s were recorded behind the three filter stages by the APD which has 35% detection efficiency. This shows a combined suppression of 114 dB by the three filters. From the known filtering performance of the polarization filtering (55 dB) and the etalon (46 dB) the effect of the spatial filtering can be calculated to be 13 dB.

6.1.2. Noise

While the above values show that the combined filter almost reaches the aimed coupling beam suppression of 12 orders of magnitude, another unexpected noise source becomes apparent here. In figure 6.2 around 90×10^3 counts/s had been subtracted because this represents a noise floor that is present at all times as soon as the EIT cell is inserted into the path of the probe beam and the coupling beam is switched on. This noise floor was found to be produced inside the EIT cell from the coupling laser, but its wavelength is exactly the wavelength of the probe transition. Therefore, spectral filtering is not possible at all. Several measures were taken to reduce the noise. The whole experiment was carefully aligned, but a slight deviation from perfect probe and coupling beam overlap was introduced, also the coupling beam was not fully collimated. The probe beam was routed for ~ 2 meters free beam behind the cell before it was coupled into the fiber. In addition, the cell temperature was reduced to 26 °C and the coupling power to 1.2 mW. All in all, these measures slightly reduce the quality of the EIT spectrum, but at the same time reduce the noise counts to 20×10^3 counts/s.

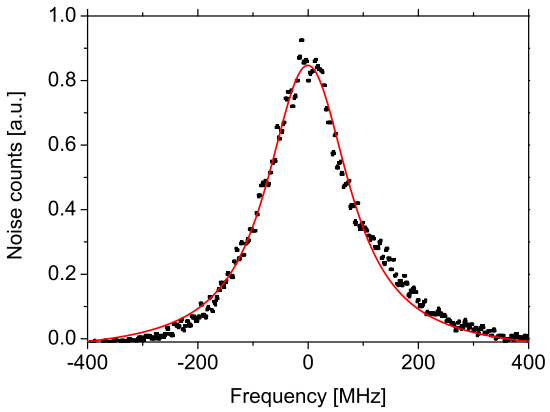

Figure 6.3.: Scan of the multi-pass etalon filter around the probe transition wavelength when only the coupling laser is applied. The black curve shows the normalized signal detected by the APD. The simulation (red curve) is performed using a Voigt profile with the multi-pass etalon linewidth as FWHM for the Lorenzian part. The Gaussian part FWHM as fit parameter is found to be 47 MHz.

The noise signal itself was studied by scanning the multi-pass etalon filter around the probe transition wavelength when only the coupling laser was applied. The measurement was simulated by a Voigt profile with the etalon linewidth as FWHM for the Lorenzian part [179] and the FWHM of the Gaussian part as fit parameter. As shown in figure 6.3, the peak-width is largely defined by the width of the etalon filter, the Gaussian FWHM is found to be only 47 MHz, suggesting a narrow-band noise source. Accordingly, the most dominant noise source is anti-Stokes Raman scattering into the probe mode. The

noise was found to increase both with cell temperature, i.e., atomic density, and coupling field intensity. While a remaining noise floor of 20×10^3 counts/s seems high at first sight if single-photon experiments should be performed, it is important to realize, that a key filtering technique, namely temporal filtering, has so far not at all been used. In several experimental configurations the time when a photon is to be expected is known. E.g., if a storage experiment is performed, this will be shortly after the read process is initiated. This knowledge allows to selectively gate the APD, which will effectively reduce noise counts. Even for quite long gating windows of 100 ns and a single-photon rate as high as 10 kHz, the noise would be reduced below the APD dark count rate if such a temporal filtering is applied.

6.2. EIT with pulses on the single photon level

In order to perform EIT on the single photon level, adequate single probe photons are required. To map quantum states of light on atomic ensembles, photons with a spectral width on the order of Doppler-free atomic lines (a few MHz) are necessary. In the planned single photon storage experiment the OPO described in chapter 3 will be used as photon source. However, interfacing single photons with EIT would require not only very narrow-band probe photons but also an extremely precise adjustment of the central wavelength of the photons. One could adjust the coupling laser wavelength to compensate for small probe photon detuning as long as the detuning is smaller than the Doppler-width of the atomic transition. In this case, the EIT resonance would occur with atoms of another velocity class within the broad velocity distribution of the atoms at room temperature. However, in addition, such a compensation would be helpful only if the probe photons are slightly detuned but stable in this property. A small oscillation of the probe photon's central wavelength, e.g., due to thermal fluctuations in the down-conversion or compensating crystal, would require a permanent readjustment or scanning of the coupling beam. This would cause a major increase of the experimental complexity or would considerably lower the signal-to-noise ratio. While it is not clear if EIT with the OPO photons is impossible, more suitable ideas for realizing the single photon storage experiment will be demonstrated in chapter 8. Nevertheless, EIT with pulses on the single photon level is an outstanding milestone on the way to single photon storage, because it shows that the complex filtering can be handled. Therefore, for the work in this thesis single photons were mimicked with highly attenuated laser pulses from a diode laser. In this way, the pulse length and thus the spectral bandwidth can be controlled conveniently by an electro-optic modulator (EOM), and the central wavelength is locked using the spectroscopy setup. In addition, the single photon rate can be high and the arrival time of each pulse is known. Even without temporal filtering this allows to overcome the problem of noise from anti-Stokes scattered photons. Moreover, based on the known arrival time at the EIT cell it is possible to measure the lower speed of light inside the cell due to the EIT effect, which brings the EIT experiment much closer to single photon storage compared to measuring the increased transparency through EIT only.

The employed experimental setup is sketched in figure 6.4. EIT was again performed within the D1 transition of ^{133}Cs in a Λ-shaped atomic system, as shown in figure 5.1, the laser system is the same as described in 5.3. However, the probe laser was amplitude-modulated by an EOM driven by an arbitrary waveform generator and is strongly attenuated by several ND filters. The electronics and EOM transfer-functions were measured and the driving waveform shaped in such a way to produce perfectly Gauß-shaped probe laser pulses at the input of the EIT cell. This allows an easy conversion of the temporal pulse length into a spectral bandwidth of the pulse. The arbitrary waveform generator was triggered externally, and the trigger pulse was also used as start signal for a time-correlated single-photon counting system (Picoquant, PicoHarp 300). Filtering and detection was again performed by the three stage filtering setup including the multi-pass etalon and by an APD. The APD signal was used as stop signal for the time measurement.

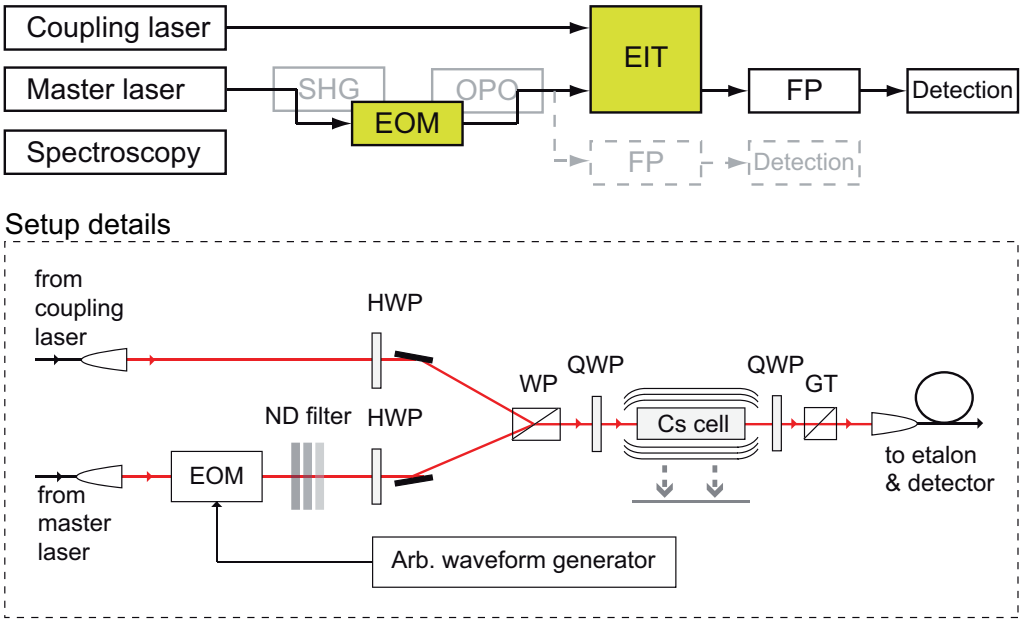

Figure 6.4.: Experimental setup for EIT experiments with probe laser pulses containing only a single photon on average. The setup consists of probe and coupling laser, an electro-optical modulator (EOM), Wollaston prism (WP), polarization optics, i.e., half-wave plates (HWP), quarter-wave plates (QWP) and polarizing beam splitters, as well as a Glan-Thompson prism (GT) and spectral filtering through a multi-pass etalon. A photo diode (PD) and avalanche photo diode (APD) are used for detection. The EIT cell is moveable perpendicularly to the laser propagation between two fixed positions in order to allow a calibration of the time measurement without the cell being present.

For the measurements, attenuated probe pulses at a rate of 100-200 kHz with a mean photon number $\bar{n} = 1.0 \pm 0.1$ were used. The time-correlated detector counts were

integrated for up to 30 minutes in order to increase the signal-to-noise ratio. The Cs cell is moveable perpendicularly to the laser propagation between two fixed positions. This allows to measure probe pulse delays with and without the cell in order to calibrate the time measurement. Contrary to the measurement of off-resonance transmission through the cell, as it is often performed in other experiments, this method does not require any other change in the experimental configuration. In this way the laser lock and Fabry-Pérot configuration is unaffected making the procedure more reliable.

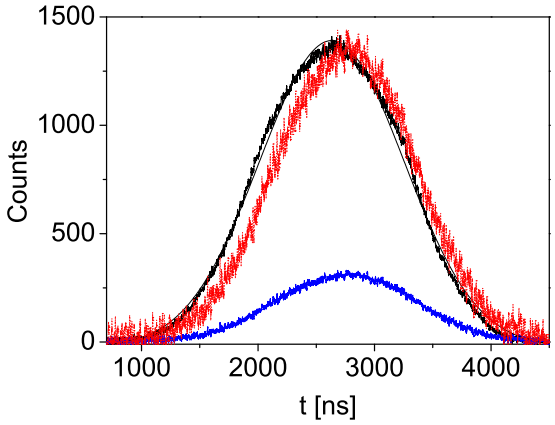

Figure 6.5.: Delayed single-photon probe pulse. The black (blue) line shows the pulse without (with) EIT cell. For comparison of the pulse shape the curve for the delayed pulse is multiplied by a factor of four and plotted as red curve. Fitting a Gauß-curve to the temporal distribution shown here allows to measure delay times caused by the low group velocity due to EIT. In addition, a modification of the pulse shape of the delayed pulses can be seen. See text for details.

In a first experiment, the delay of a pulse at the single photon level caused by the low group velocity inside the EIT cell was studied. The delay times were measured by fitting a Gauß-curve to the temporal distribution of the probe photon detection events with and without the EIT cell in the beam line. Figure 6.5 shows exemplarily a measurement for a probe pulse length of ≈ 1.5 μs. A transmission of 25% for the probe pulse can be derived. For comparison the curve for the delayed pulse is enlarged accordingly which makes the pulse delay apparent. In addition, a slight reshaping of the pulse is visible.

To further investigate this effect, a systematic study of EIT delays for varying lengths and thus spectral widths of the probe pulses was performed. The results are shown in figure 6.6. For each measurement the EOM driving function and thus the pulse length was modified, and the intensity of the probe pulses was subsequently adjusted in order to maintain the Gaußian pulse shape and the average intensity of one photon per pulse. The calculated curve in figure 6.6 is based on equation 5.8 from section 5.2.2 and the experimentally accessible parameters, these are cell temperature, spontaneous emission

rate of the Cs D1-line, and coupling laser power. Just like in section 5.4 the atomic dephasing rate was introduced as the only fit parameter. An excellent agreement with the measured data (dots in figure 6.5) is observed, in particular for the most relevant pulses with a bandwidth of approximately the EIT transmission window width, which is indicated by the vertical line.

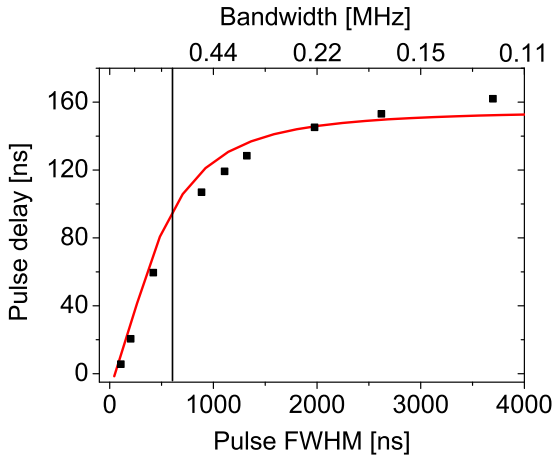

Figure 6.6.: Dependence of time delays caused by EIT on the spectral and temporal FWHM of the probe pulse. The vertical line indicates the width of the EIT transmission window. The dots are experimental results and the solid line is a theoretical calculation based on equation 5.8 from section 5.2.2. Besides experimentally accessible parameters the atomic dephasing rate was introduced as the only fit parameter.

Due to the small width of the EIT transmission window, which is around 720 kHz, a modification of the pulse shape of the delayed pulses, which can be attributed to group velocity dispersion, can be expected for pulses with a spectral bandwidth similar or larger than the width of the EIT transmission window. Since pulses of a spectral bandwidth ranging from 100 kHz to 4.5 MHz have been studied in order to come close to the single photons from the OPO, such pulse shape modifications can be expected. In fact, they are present in figure 6.5. The red curve in figure 6.5 representing the enlarged delayed pulse is modified compared to the undelayed pulse (black curve in figure 6.5).

6.2.1. Single photon amplitude modulation

The successful demonstration of EIT in the Cs cell at ultralow intensity together with the first experiments on EIT based phase control from section 5.6 in principle also allows coherent amplitude and phase control of light pulses on the single photon level [69]. Amplitude and phase shaping of single photons has gained considerable interest and, using an EOM as modulator, both techniques were demonstrated recently [180, 181]. Due to limited modulation and detection speed, the key components in these setups are photon sources that produce single photons of very long temporal length and at the same time

of a well defined time origin. In fact, these are exactly the properties of the single-photon pairs produced by the cavity-enhanced down-conversion source from chapter 3. Accordingly, several ideas exist to use the OPO source for such experiments, which will be discussed in chapter 8. There are several potential applications for amplitude and phase shaping of single photons. Amplitude modulation might be used to optimally load a single photon into an optical cavity [15], or to study the transient response of atoms to different single-photon waveforms. It might also improve the efficiency of storage and retrieval of single photons in an atomic ensemble [152, 72, 182, 183]. In the context of quantum information applications amplitude and phase modulation together would allow full control over the single-photon waveforms. This would further allow encoding of information into the relative phase difference between consecutive pulses of a single-photon waveform that is constructed as a train of identical pulses [184], as well as applications in the field of time-bin entanglement [185]. Phase control of single photons would enable to create and even compensate any arbitrary phase shape, a technique that might be used for quantum computation protocols with linear optics [25, 186]. Also, shaping the phase of a reference photon would allow to fully determine the phase properties of an unknown photon, a technique which could also be used for quantum key distribution protocols [187] with the advantage of not requiring interferometric stability. To demonstrate the idea of EIT based amplitude modulation of a pulse on the single photon level, the setup in figure 6.4 was extended by an AOM that modulates the coupling laser's amplitude. The AOM was controlled by a second arbitrary waveform generator triggered simultaneously with the EOM controller. Due to the direct dependency of the EIT transmission on the coupling laser power, an arbitrary waveform of the probe pulse can be generated by modulating the coupling beam while the probe pulse traverses the EIT cell.

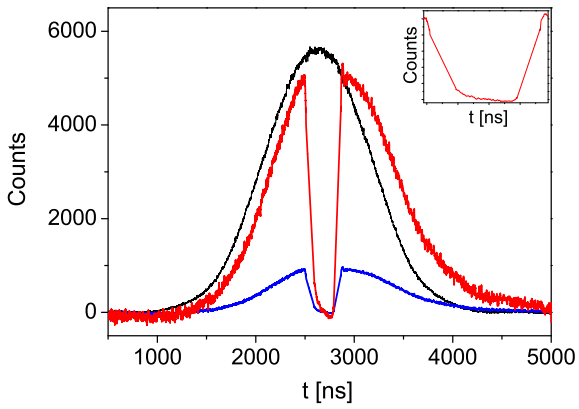

Figure 6.7.: Control of a probe laser wave packet containing only a single photon on average through EIT by modulation of the coupling laser. The black curve is the undisturbed pulse without EIT cell. The blue curve shows the probe pulse, which is split coherently into two components thus forming a time-bin encoded qubit state. For comparison the curve for the split pulse is multiplied by a factor of 5.5 and plotted as red curve. The inset shows an enlarged version of the dip in the middle of the probe pulse (see text).

As an example, figure 6.7 shows a pulse at the single photon level which was split into two pulses. The inset in figure 6.7 shows an enlarged version of the dip in the middle of the probe pulse. It reveals that the modulation amplitude is almost 100% and that the modulation speed is mainly limited by the speed of the AOM. The AOM caused the fully linear part of the decrease and increase of the probe amplitude around the central dip, the respective rise time corresponds well to the AOM specification. The waveform shown in figure 6.4 represents a time-bin encoded state [188] because the phase between the two components of the wave packet can be controlled by changing the off-time duration of the coupling laser. Such a modulation might be used in a quantum key distribution (QKD) protocol exploiting weak classical pulses and the decoy state protocol [23]. This protocol has been quite successful in QKD in recent years because it is unconditionally secure even with a classical photon source. It only requires a source emitting attenuated light pulses of several different fixed intensities (e.g., average photon number per pulse μ of 0.55, 0.1 and 7.5×10^{-4}, respectively [189]) and the pulses must not contain on average just $\mu \sim t$ photons for unconditional security [22], where t is the transmittivity of the quantum channel. Hence, for long channels the average number of photons per pulse can be much higher, and the transmission rate will increase accordingly.

6.2.2. Discussion and short summary

The results above prove, that the very important threshold of EIT in Cs vapor at room temperature with light pulses containing only one photon was reached for the first time. This was made possible by the advanced spectral filtering using a multi-pass etalon, and it now allows experiments in the quantum regime. As pointed out in section 5.2, Cs offers certain advantages compared to Rb, among them a transition wavelength compatible with solid-state single or entangled photons (e.g., based on InAs quantum dots) and most importantly, a larger hyperfine splitting allowing storage of photons with a larger bandwidth than Rb [76]. Based on these results, single photon storage experiments should be possible soon. The route towards such experiments will be outlined in part III. Several other groups work on the extension of EIT or related setups to the single photon level, e.g., in the supplementary information of Reim et al. [76] it is explicitly stated that moving towards quantum operation by using single photons is a major goal, but that this was not possible yet. It can be expected that a filtering system like the one described above would be beneficial for several other experiments too.

In addition, time-bin encoded states were generated and controlled with wavelengths corresponding to the Cs D1-line. Experiments with 'true' single photons generated by the OPO described in chapter 3 can be envisioned. The modulation amplitude is almost 100% and its speed is mostly defined by the AOM. However, it would be interesting to study whether the remaining non linearities shown in the inset in figure 6.7 are caused by the atomic system itself, i.e., if a possible simulation of the EIT dynamics shows the same effect. The EIT cell can be regarded here as a temporal beam splitter capable of distributing a pulse at the single photon level over two distinct temporal modes. In conjunction with the 'true' narrow-band single photons a single photon entangled state can be generated and subsequently transferred to other atomic ensembles. While such

an idea was discussed and demonstrated by Choi et al. [190] in a setup purely based on atomic systems in a magneto-optical trap, it would be very interesting to study these effects in a combined system based on a down-conversion source and an atomic system, as this would represent a 'real' quantum interface.

Part III.

Conclusion and Outlook

7. Summary of the Experimental Status Quo

Based on the outline of the research context given in chapter 1, the consecutive chapters described the objectives that have been already reached and details about completed building blocks of the single photon storage experiment. This final chapter provides a brief overview of the present state of the experiment together with information about next steps and the envisioned concepts for its further development.

During this thesis several important milestones of the single photon storage experiment were reached.

1. The single-photon source that already existed in our research group was carefully examined. This yielded new results and allowed insights into the statistics of heralded single photons produced by a down-conversion source. A triple-coincidence analysis of two-photon states emitted from the SPDC source under cw excitation was performed. Due to a tremendously enhanced coherence time of this source compared to former studies, the detector's time jitter was negligible and the first direct detailed measurements of the triple-coincidence statistics became possible.

2. A spectral filter based on a multi-pass etalon was built and its performance studied. With a measured peak transmission of 65% and a suppression of off-resonant light by 46 dB the performance is satisfactory for several tasks in the overall single photon storage experiment. Even though other multi-pass etalon implementations reported in the literature have a far higher contrast, they have a much lower peak transmission. In fact, an appropriate scaling of the transmission of these other instruments to an acceptable value would result in a lower contrast than what was reached during the work presented here. As in QIP every photon lost due to low filter transmission may cause a loss in quantum information, hence a high transmission is crucial. The performance of the multi-pass etalon was studied in real applications, namely filtering of single photons from the SPDC source and coupling beam filtering in an EIT experiment, and in a simulation as noise filter for long range free-space QKD experiments.

3. A phase-locked laser system for EIT experiments was built and its performance studied in terms of the achievable residual phase-noise variance. The system was found to be comparable or better than the previously described realizations.

4. Based on the phase-locked laser system and using the multi-pass etalon filter EIT experiments in Cs vapor at room temperature with a single-photon probe beam were performed for the first time. This can be regarded as crossing an important

threshold as it allows to extend EIT experiments in Cs to the quantum regime. The results extend single-photon EIT to a particularly interesting wavelength. For example, in conjunction with recently demonstrated broad-band optical quantum memories in Cs vapor cells [76] manipulation or storage of single or entangled photons from semiconductor sources at a wavelength capable to match Cs transitions [191] becomes feasible.

Based on the results obtained, the overview of the aspired full experimental setup for single photon storage from chapter 1 can be supplemented with information on the status of the individual components, as shown in figure 7.1.

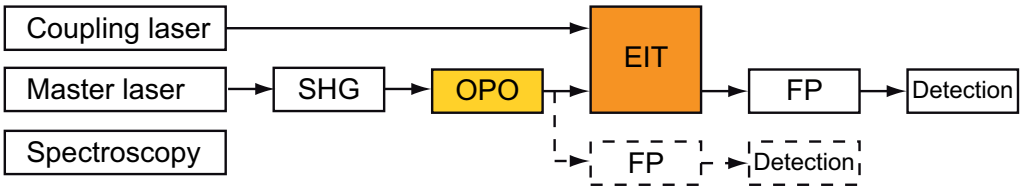

Figure 7.1.: Overview of the experimental building blocks described in this thesis with their respective status. White boxes show completed building blocks, yellow (orange) denotes necessary minor improvements (major changes).

While several building blocks are almost completed, some problems arose during the work on other parts of the experiment, requiring adjustments of the overall concept. However, at the same time this allows some major extensions of the experimental goals. The extended goals and resulting adjustments of the concept shall be discussed in the following sections. In summary, the goal of using ultranarrow bandwidth photons is slightly weakened due to new memory options. At the same time, the ability to produce these photons opens up new possibilities for noise reduction and capacity scaling.

8. Towards Quantum Repeaters

The distribution of quantum states over long distances is currently limited by loss and decoherence in the quantum channel. An optical fiber based channel is limited by losses of 0.2 dB/km in the optimal wavelength, i.e., 95% transmission for a fiber of 1 km length. Even with a photon production rate of 10 GHz, for a 500 km transmission one would have a transmission rate of only 1 Hz, which drops to 10^{-10} Hz for 1000 km. Although technologies like satellite based QKD (see section 4.3) might extend the exchange of quantum information to global scales, for quantum networks or more complex QKD systems the necessity to connect individual transmission lines remains. In classical telecommunication this can be reached by a simple amplifier (often called repeater). However, the no-cloning theorem [58, 59] shows that noiseless amplification is only possible for sets of orthogonal states, whereas the quantum nature and thus the advantage of protocols like QKD arise from the existence of non-orthogonal states. The problem can be overcome by using a so-called quantum repeater [26] based on entanglement between distant systems. The idea is to make use of a particular feature of entanglement, namely that it can be swapped [61]. From two existing entangled states, one between system A and system B and another between systems C and D, it is possible to create an entangled state between systems A and D by performing a joint measurement of systems B and C and classical communication of the result. In a quantum repeater one would generate entanglement over a long distance L by entanglement swapping starting from two entangled pairs, each of which covers only $\frac{L}{2}$. This could be extended by creating those states from states covering only $\frac{L}{4}$ and so on, as shown in figure 8.1.

If one finally has an entangled state over distance L, one can use this state to teleport an arbitrary quantum state over this distance or perform entanglement-based QKD directly [192].

8.1. Quantum memories

One essential requirement for such a quantum repeater protocol is that one has to be able to store the created elementary entanglement until entanglement has been established in the next link. Furthermore, the capability to store photons would also allow to improve the quality of established entanglement via entanglement distillation. Therefore, quantum repeaters require high quality quantum memories. A quantum memory can be realized using different approaches based on atomic ensembles [193, 194, 145] and solid-state systems [195]. In a quantum repeater setup the quantum memory should have long coherence times, efficient interfacing with photons and the possibility to perform entanglement swapping operations. Furthermore, the relevant criteria for evaluating quantum memories are fidelity, efficiency, storage time, bandwidth, and the ability to

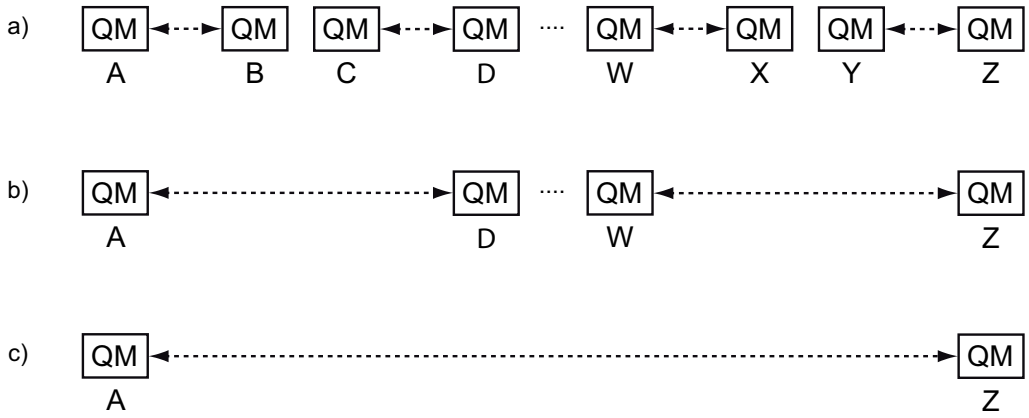

Figure 8.1.: Principle of quantum repeaters. Step by step course towards long-distance entanglement. a) Entanglement is first created independently within short links, e.g., between locations A and B, C and D, W and X, Y and Z. b) Entanglement is subsequently swapped between neighboring links, i.e., A and D,...,W and Z share entanglement. c) Entanglement swapping is performed successively until entanglement is distributed over the entire distance, i.e., A and Z share entanglement. QM stands for quantum memory, dashed arrows indicate entanglement.

store multiple photons, i.e., multi-mode operation. The fidelity is related to the overlap between the quantum input and output state of the memory. It is important for error-free communication. A high efficiency of the memory is clearly desirable but not always mandatory, depending on the application. However, the combined fidelity times efficiency must be higher than the classical limit [80]. The storage time is very important for long-distance quantum communication as it limits the available communication time between the nodes. The bandwidth limits the possible repetition rates. While for all of these criteria a higher value is always better, some mutual compensation is possible and the particular relevance depends on the particular application [196].

Today, several proposals exist for building quantum repeaters using single-photon sources and quantum memories [62]. Probably the most prominent one is the DLCZ protocol introduced by Duan, Lukin, Cirac, and Zoller in 2001 [17], which is based on atomic ensembles as quantum memories and on linear optics. Based on the results of this thesis, another protocol described by Simon et al. in reference [197] is of particular interest, as it is also based on the building blocks of a photon-pair source and an absorptive memory. In this protocol entanglement creation between two remote locations A and B is performed using a photon-pair source and one memory at each location, denoted $S_{A(B)}$ and $M_{A(B)}$, as shown in figure 8.2.

The sources are simultaneously and coherently excited, and each of them has a small

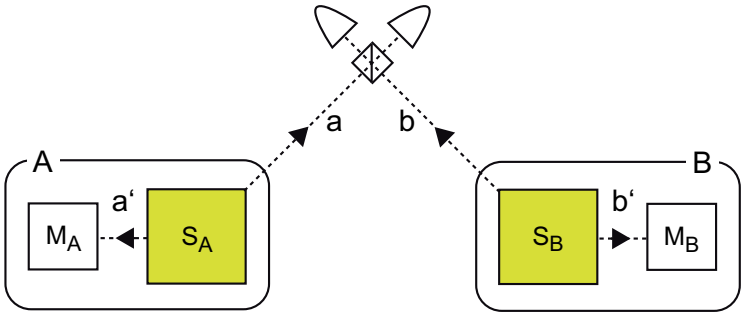

Figure 8.2.: Quantum repeater using photon-pair source and absorptive memory. The yellow (SPDC) source $S_{A(B)}$ on location A and B emits photon pairs. One photon out of the pair is stored locally, the other is transmitted to a central station. At the central location the two incoming photons are combined on a beam splitter, such that the detection of a single photon in one of the output ports heralds quantum entanglement between the memories $M_{A(B)}$ in A and B.

probability $p/2$ to emit a photon pair, corresponding to the state

$$\left[1+\sqrt{\frac{1}{2}}e^{i\phi_A}a\dagger a'\dagger+e^{i\phi_B}b\dagger b'\dagger+O(p)\right]|0\rangle\ . \tag{8.1}$$

The modes a and a' (b and b') correspond to S_A (S_B), ϕ_A (ϕ_B) is the phase of the pump laser at location $A(B)$, $|0\rangle$ is the vacuum state. The $O(p)$ term describes the possibility of multiple-pair emission and, as it introduces errors into the protocol, leads to the requirement that p has to be kept small. The modes a' and b' are stored locally, a and b are combined on a beam splitter at a central station and are detected. The detection of a single photon behind the beam splitter heralds the storage of a single photon in memories A and B, which can be written as entangled state of the two memories,

$$|\Phi_{AB}\rangle=\frac{1}{\sqrt{2}}(|1\rangle_A|0\rangle_B+e^{i\Theta_{AB}}|0\rangle_A|1\rangle_B)\,, \tag{8.2}$$

where $|0\rangle_{A(B}$ denotes the empty state of $M_{A(B)}$ and $|1\rangle_{A(B}$ denotes storing of a single photon. It is $\Theta_{AB}=\Theta_B-\Theta_A$ and $\Theta_{A(B)}=\phi_{A(B)}+\chi_{A(B)}$, where $\chi_{A(B)}$ are the phases acquired by the photons on their way to the central station.

In the context of this experiment it would be reasonable to realize the photon-pair source by a modified cavity-enhanced down-conversion source, similar to the one described in chapter 3 but with pulsed excitation. As photon memory an EIT based system, similar to the one described in chapter 6, might be used. However, recent findings [76] suggest some modifications of the setup, i.e., to establish a so-called Raman memory.

8.2. Raman memories

The idea behind Raman memories is to use off-resonant Raman interactions to access long-lived material coherences optically and thereby store propagating photons as stationary excitations of a Raman coherence while avoiding fluorescent losses. The storage bandwidth is generated dynamically by ancillary write/read pulses, which dress the narrow atomic resonances to produce a broad virtual state to which the signal field couples [198, 199, 152, 200]. The signal is coherently absorbed into this virtual state and, unlike in EIT, no reduction of the group velocity occurs.

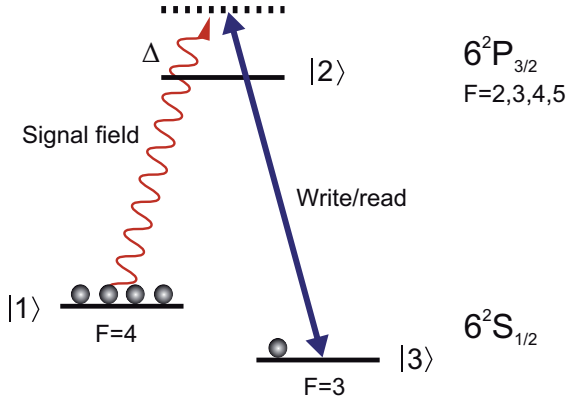

Figure 8.3.: Λ-shaped level structure of the atoms in the Raman memory. The atoms are prepared in the ground state $|1\rangle$ by optical pumping. The signal is tuned into two-photon resonance with a so-called write field. Both fields are detuned Δ from the excited state $|2\rangle$. Absorption of a signal photon transfers an atom from $|1\rangle$ into the storage state $|3\rangle$ via Raman scattering stimulated by the write field. Upon retrieval, the interaction is reversed. [76]

The main benefit of such a memory is its ability to store broadband pulses, which makes interfacing with down-conversion sources much easier and at the same time allows a higher photon 'clock rate' due to shorter pulses. Because the Raman transition is detuned far beyond the Doppler linewidth of cesium vapor, its insensitivity to inhomogeneous broadening and a lower noise floor can be expected. Although the physical effects used for photon storage are different from an EIT based memory, the experimental setup required is very similar. The first Raman memory was demonstrated in 2010 [76] using a Cs vapor cell too, however, utilizing the D2 line at 852 nm. The atomic level structure which was used in this experiment is shown in figure 8.3. Unlike in an EIT based setup the optical fields are detuned away from the excited state resonance. The bandwidth of the stored pulses was 1 GHz and is limited by the splitting of the ground state and the storage state of the atomic medium. In case of Cs, this is the ground state hyperfine splitting of 9.2 GHz which allows a maximum storage bandwidth of approximately 4 GHz. Storage times of 5 μs have been observed already [201], and the limit is probably

on the order of 100 μs or even much longer if the atoms are confined, e.g., as dopants in a solid-state host [80, 202]. The total efficiency so far is 15 %, more than 90 % should be reachable with phase-matched retrieval in the backward direction [203].

Operating such a broad-band Raman memory on the single photon level instead of the EIT based memory would be very worth pursuing for several reasons: It would require less effort on the side of the single-photon source as photons need not be as narrow-band as for an EIT based storage system. Also, it might overcome the problems of Raman noise which, as our measurements suggest, are still an obstacle even with improved noise suppression. In addition, a memory allowing to store photons which are more than 2 orders of magnitude broader than the produced photons, paves the way for totally new applications, as described in the following section.

8.3. Spread spectrum encoding of single photons

Very recent works [204] describe the use of so-called spread spectrum technology [205] at the single photon level. This technology, which originates from the field of classical communication, basically modulates a data signal onto a wideband carrier so that the resulting transmitted signal has a bandwidth which is much larger than the data signal bandwidth and which is relatively insensitive to the spectral width of the data signal. This technique makes the resulting signal insensitive to noise and jamming. It can be adapted to single photons using two synchronously driven electro-optic phase modulators as transmitter and receiver. This allows a narrow-band photon to be modulated and thus broadened and later demodulated for detection behind a narrow-band filter. In a situation where the single-photon beam should be transmitted, e.g., through an environment of other photons that have a linewidth that is comparable to that of the original photon beam, the noise will be spectrally broadened by the second modulator. Thus only a fraction of its power is transmitted through the narrow-band filter in front of the receiver. As a result, the signal-to-noise ratio is increased approximately by the ratio of the modulation bandwidth to the bandwidth of the final filter. The increased signal-to-noise ratio is called a processing gain. Such a processing gain of a factor of 50 was already demonstrated in a single photon experiment [204]. Using such a modulation of the single photons together with a broadband memory should further reduce the problem of (anti-Stokes) noise photons as these noise photons are very narrow-band, as shown in section 6.1.2. The spread spectrum technique requires that the bandwidth of the modulated photons is much larger than the bandwidth of the unmodulated photons, i.e., the photon source must have a much narrower bandwidth than the storage system, a prerequisite perfectly fulfilled by the OPO photons and a Raman memory.

This concept might be even extended further and may eventually lead to multiplexing of single photons inside the memory, i.e., multi-mode quantum memories.

8.4. Multi-mode quantum memories

In a nested quantum repeater protocol [26] of which the DLCZ protocol [17] is the best known one, the entanglement connection operations creating entanglement between non-neighboring nodes can only be performed once entanglement between the neighboring nodes A and B is established. This is typically conditioned on a measurement, e.g., the detection of one or more photons at a station between these two nodes [197]. Hence, the measurement has to be transmitted to A and B first, which requires a communication time of the order of D_0/c_{fiber}, where D_0 is the distance between A and B and $c_{fiber} = 2\times 10^8$ m/s. This limits conventional repeater protocols to a single entanglement generation attempt per elementary link per time interval D_0/c_{fiber}. For a total link distance of $D_{tot} = 1000$ km even with an optimistically assumed memory and detection efficiency of $\eta_m = \eta_d = 0.9$ the resulting entanglement distribution time $T_{tot} = 4100$ seconds is very long [62]. In particular, the memory storage time has to be comparable to T_{tot}. This seems out of reach with current technology as the longest storage time achieved in solid state systems, which are particularly suited for long storage times, is of the order of 1 second, though not yet at the quantum level [206]. Decoherence times as long as 30 seconds have been demonstrated [207] in solid state systems as well, but there is currently no system within reach that promises longer storage times of more than two orders of magnitude.

A solution for these fundamental problems might arise from multi-mode quantum memories. The basic idea is to build a quantum repeater as introduced in the beginning of this chapter, that does not require to wait for the communication time D_0/c_{fiber} until the next pulse is sent. Instead, a train of N pulses is sent and at the same time stored in a multi-mode quantum memory. This leads to an increase of the entanglement generation probability P_0 by a factor of N (for $NP_0 \ll 1$), which directly translates into an increase of the entanglement distribution rate by the same factor. Using a memory with e.g. $N = 100$ modes together with the protocol from reference [197] would result in $T_{tot} = 51$ seconds or even $T_{tot} = 12$ seconds in case of $\eta_m = \eta_d = 0.95$. Thus, the demonstration of a multi-mode quantum memory would be a very interesting experiment. Theoretical considerations showed that atomic ensembles are in principle well qualified for multi-mode memories [208], and a realization based for example on spread spectrum encoding of single photons should be studied further.

8.5. Planned experimental setup

A first experimental setup that incorporates the ideas of Raman memory and spread spectrum encoding into the single photon storage experiment is suggested in figure 8.4.

The Raman memory is from an experimental point of view similar to the EIT based memory. However, a much higher coupling beam intensity (from now on called write/read laser) is required, therefore, additional tapered amplifiers will be needed. The exact write/read laser frequency could be flexibly adjusted using the available frequency offset lock. In order to allow amplitude modulation of the write/read laser to generate the

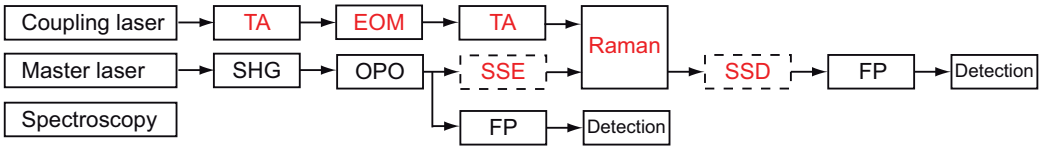

Figure 8.4.: Planned experimental setup. The photon storage will be modified to employ a Raman memory. This requires additional tapered amplifiers (TA) and an EOM for amplification and amplitude modulation of the coupling laser. Moreover, the setup shall be extended by spread spectrum encoding and decoding (SSE, SSD) of the single photons.

required write and read pulse with the necessary fast timing, a (preferably fiber-based) EOM is needed. It could be controlled by a fast arbitrary waveform generated and triggered for instance on the detection of an idler photon with an adequate delay line, i.e., a long fiber, for the signal photon (not shown) installed in front of the cesium cell.

By use of two phase modulating EOMs in front of and behind the EIT cell, spread spectrum encoding/decoding of the stored signal photon could be implemented. Both EOMs need to be controlled by fast synchronized bit sequence generators in order to use one pseudo random bit sequence for encoding and its inverse for decoding. The bit sequence generators have to be fast enough to match the width of the Raman memory, i.e., around 1 Gb/s is required for a width of the Raman memory of 1 GHz. The encoding signal could possibly be triggered on the detection of an idler photon as well. The decoding needs to be synchronized with the read laser pulse.

8.6. Physics of very long single-photon wave packets

Besides the new concepts for the single photon storage experiment, other research fields open up based on the already developed and the envisioned experimental building blocks. One can regard the ultranarrow-band single photons produced by the OPO as one of the largest quantum objects created so far, and at the same time they are relatively simple and reliable to produce. A spectral width of $\sim$ 4.6 MHz corresponds to a temporal dimension of $\sim$ 220 ns for the wave packet and therefore to a spatial length of 66 meters. Although other sources are capable of producing even slightly narrower photons [30, 48, 49] of around 1 MHz spectral bandwidth, they require single-atom/-ion traps or a MOT, making them complex and not very reliable.

The long extension of the photon wave packet, hence of the coherence time, allows to perform new experiments with single photons that require electronic systems to operate on time scales far below the coherence time. For example, detecting one of the two generated photons allows to establish the time origin for electronic modulation of the second photon. The wave packet is very long compared to the temporal resolution of a single-photon detector, which can be as low as 40 ps. Once the time origin is established, the wave packet of the second photon may be modulated in the same manner as a classical pulse of light can be modulated. The wave packet may be phase, frequency, amplitude,

or digitally modulated and the maximum modulation frequency is limited only by the resolution of the detection of the first photon [180].

Another application would be to study interference effects between the two generated photons. Unlike with classical optical fields, single-photon interference on a beam splitter can result in a reduction of coincidence detection behind the beam splitter well below 50%, which is the classical limit. Using very long single-photon wave packets this well-known *Hong-Ou-Mandel effect* [209] could be studied in more detail. Such studies are otherwise often prevented by the limited time resolution of the detectors compared to the coherence time of the photons [210].

Appendix A: Cesium D1-Line

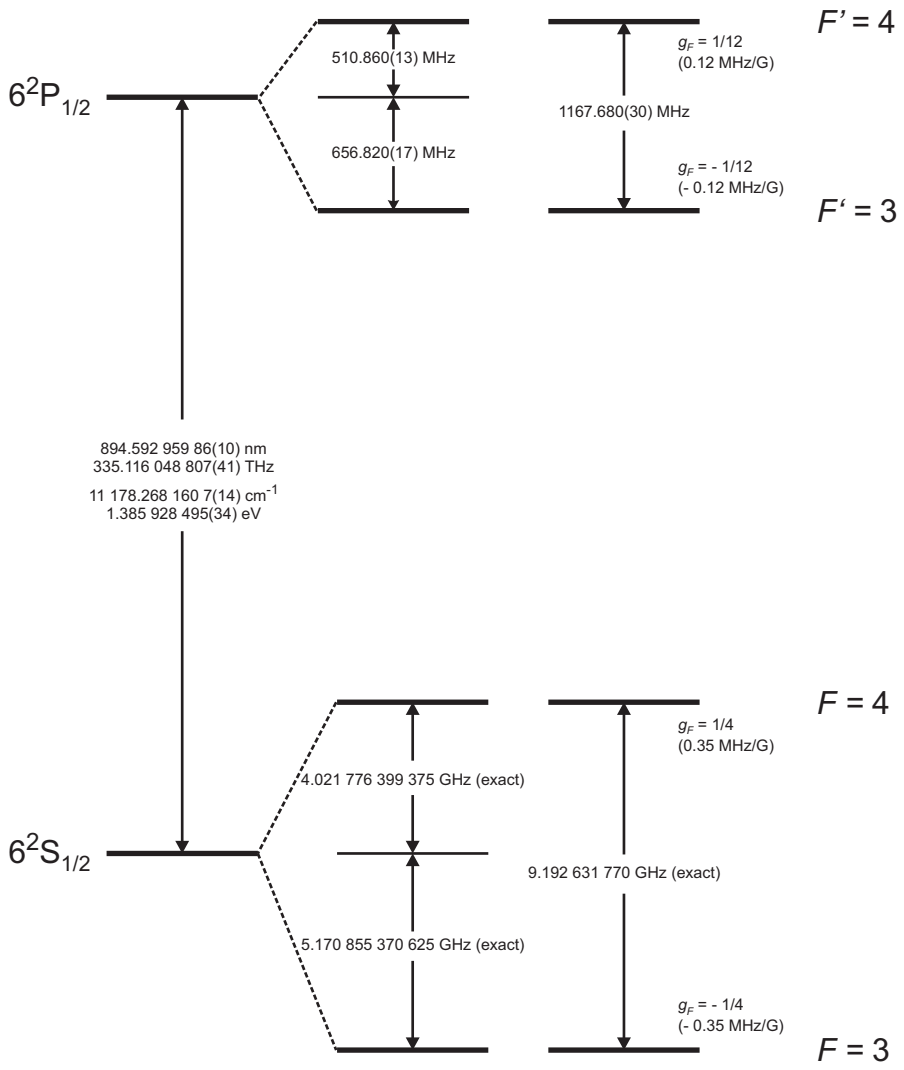

Figure A.1.: Frequency splittings between the hyperfine energy levels on the cesium D1-line. The ground-state values are exact as a result of the current definition of the second. The g_F denote the approximate Landé factors for each level together with level shifts due to a magnetic field [157].

Abbreviations

AOM	Acusto-Optical Modulator
APD	Avalanche Photo Diode
BP	Band-Pass
BS	Beam Splitter
BW	Bandwidth
cw	continuous-wave
DL	Diode Laser
DLCZ protocol	Duan, Lukin, Cirac, and Zoller protocol
DM	Dichroic Mirror
DWDM	Dense Wavelength Division Multiplex
EIT	Electromagnetically Induced Transparency
EOM	Electro-Optic Modulator
HBT	Hanbury Brown and Twiss
FC	Fiber Coupler
FFT	Fast Fourier Transform
FMS	Frequency Modulation Spectroscopy
FP	Fabry-Pérot
FSR	Free Spectral Range
FWHM	Full Width at Half Maximum
GT	Glan-Thompson Prism
HWP	Half-Wave Plate
IF	Interference Filter
$KNbO_3$	Potassium Niobate
KTP	Potassium Titanyl Phosphate
LOQC	Linear Optics Quantum Computation
LO	Local Oscillator
LP	Long-Pass
MOT	Magneto-Optical Trap
NA	Numerical Aperture
NV	Nitrogen-Vacancy
OPLL	Optical Phase-Locked Loop
OPO	Optical Parametric Oscillator

PBS	Polarizing Beam Splitter
PD	Photo Diode
PFD	Phase Frequency Detector
PH	Pinhole
Pol	Polarizer
PPKTP	Periodically Poled Potassium Titanyl Phosphate
PLL	Phase-Locked Loop
PS	Power Source
PZT	Piezo-electric Tube
QD	Quantum Dot
QIP	Quantum Information Processing
QWP	Quarter-Wave Plate
RF	Radio Frequency
SEM	Scanning Electron Microscope
SHG	Second Harmonic Generation
SPDC	Spontaneous Parametric Down-Conversion
SPS	Single-Photon Source
SSPD	Superconducting Single-Photon Detector
TEM	Transverse Electro-Magnetic
WDM	Wavelength Division Multiplex
WP	Wollaston Prism

Own publications

The following papers were published during the work on this thesis.

Steudle, Gesine, Schietinger, Stefan, **Höckel, David**, Dorenbos, Sander, Zwiller, Valéry, and Benson, Oliver
Measuring antibunched photon statistics of a quantum emitter with a single detector,
Nano Lett., *in preparation*

Höckel, David, Koch, Lars and Benson, Oliver
Direct measurement of heralded single-photon statistics from a parametric down-conversion source,
Phys. Rev. A **83**, 013802 (2011)

Höckel, David and Benson, Oliver
Electromagnetically induced transparency in cesium vapor with probe pulses on the single photon level,
Phys. Rev. Lett. **105**, 153605 (2010)

Höckel, David, Martin, Eugen and Benson, Oliver
Note: An ultranarrow bandpass filter system for single-photon experiments in quantum optics,
Rev. Sci. Instrum. **81**, 026108 (2010)

Höckel, David, Koch, Lars, Martin, Eugen and Benson, Oliver
Ultranarrow bandwidth spectral filtering for long-range free-space quantum key distribution at daytime,
Opt. Lett. **34**, 3169 (2009)

Höckel, David, Scholz, Matthias and Benson, Oliver
Electromagnetically induced transparency experiments in cesium vapor - Towards single photon operation,
AIP Conf. Proc. **1110**, 253 (2009)

Höckel, David, Scholz, Matthias and Benson, Oliver
A robust phase-locked diode laser system for EIT experiments in cesium,
Appl. Phys. B **94**, 429 (2009)

Talks and presentations at conferences

Höckel, David, Koch, Lars and Benson, Oliver
Electromagnetically induced transparency in cesium vapor with a single photon probe beam,
French-German Research: 50 Years in the Light of the Laser, Berlin (2010)

Höckel, David, Koch, Lars and Benson, Oliver
Electromagnetically induced transparency in cesium vapor with a single photon probe beam,
Quantum Electronics and Laser Science Conference, San Jose (2010)

Höckel, David, Martin, Eugen and Benson, Oliver
Ultra-narrow bandwidth spectral filtering for long range free-space quantum key distribution at daytime,
International Conference on Quantum Information Processing and Communication, Rome (2009)

Höckel, David, Scholz, Matthias and Benson, Oliver
Phase-locked laser system for electromagnetically induced transparency experiments in cesium vapor,
9th International Conference on Quantum Communication, Measurement and Computation, Calgary (2008)

Höckel, David, Scholz, Matthias and Benson, Oliver
Delayed light pulses using cesium vapor,
DPG Frühjahrstagung, Düsseldorf (2007)

Bibliography

[1] Gordon Earle Moore. Cramming more components onto integrated circuits. *Electronics*, 19(3):114–117, 1965.

[2] Richard Feynman. Simulating physics with computers. *Int. J. Theor. Phys.*, 21 (6):467–488, 1982.

[3] Lov K. Grover. A fast quantum mechanical algorithm for database search. *STOC '96: Proceedings of the twenty-eighth annual ACM symposium on Theory of computing*, pages 212–219, 1996.

[4] Peter W. Shor. Polynomial-time algorithms for prime factorization and discrete logarithms on a quantum computer. *SIAM J. Comput.*, 26(5):1484–1509, 1997.

[5] Tatjana Wilk, Simon C. Webster, Axel Kuhn, and Gerhard Rempe. Single-atom single-photon quantum interface. *Science*, 317(5837):488–490, 2007.

[6] Immanuel Bloch. Quantum coherence and entanglement with ultracold atoms in optical lattices. *Nature*, 453(7198):1016–1022, 2008.

[7] Ferdinand Schmidt-Kaler, Hartmut Häffner, Mark Riebe, Stephan Gulde, Gavin P. T. Lancaster, Thomas Deuschle, Christoph Becher, Christian F. Roos, Jürgen Eschner, and Rainer Blatt. Realization of the Cirac-Zoller controlled-not quantum gate. *Nature*, 422(6930):408–411, 2003.

[8] D. Leibfried, B. DeMarco, V. Meyer, D. Lucas, M. Barrett, J. Britton, W. M. Itano, B. Jelenkovic, C. Langer, T. Rosenband, and D. J. Wineland. Experimental demonstration of a robust, high-fidelity geometric two ion-qubit phase gate. *Nature*, 422(6930):412–415, 2003.

[9] Rainer Blatt and David Wineland. Entangled states of trapped atomic ions. *Nature*, 453(7198):1008–1015, 2008.

[10] Peter Michler, A. Kiraz, Christoph Becher, W. V. Schönfeld, Pierre M. Petroff, Lidong Zhang, Evelyn Hu, and Atac Imamoğlu. A quantum dot single-photon turnstile device. *Science*, 290(5500):2282–2285, 2000.

[11] J. R. Petta, A. C. Johnson, J. M. Taylor, E. A. Laird, A. Yacoby, M. D. Lukin, C. M. Marcus, M. P. Hanson, and A. C. Gossard. Coherent manipulation of coupled electron spins in semiconductor quantum dots. *Science*, 309(5744):2180–2184, 2005.

[12] L. Childress, M. V. Gurudev Dutt, J. M. Taylor, A. S. Zibrov, F. Jelezko, J. Wrachtrup, P. R. Hemmer, and M. D. Lukin. Coherent dynamics of coupled electron and nuclear spin qubits in diamond. *Science*, 314(5797):281–285, 2006.

[13] J. E. Mooij, T. P. Orlando, L. Levitov, Lin Tian, Caspar H. van der Wal, and Seth Lloyd. Josephson persistent-current qubit. *Science*, 285(5430):1036–1039, 1999.

[14] Y. A. Pashkin, T. Yamamoto, O. Astafiev, Y. Nakamura, D. V. Averin, and J. S. Tsai. Quantum oscillations in two coupled charge qubits. *Nature*, 421(6925):823–826, 2003.

[15] Juan Ignacio Cirac, Peter Zoller, H. J. Kimble, and H. Mabuchi. Quantum state transfer and entanglement distribution among distant nodes in a quantum network. *Phys. Rev. Lett.*, 78(16):3221–3224, 1997.

[16] Seth Lloyd, M. S. Shahriar, Jeffrey H. Shapiro, and P. R. Hemmer. Long distance, unconditional teleportation of atomic states via complete Bell state measurements. *Phys. Rev. Lett.*, 87(16):167903, 2001.

[17] L.-M. Duan, Mikhail D. Lukin, Juan Ignacio Cirac, and Peter Zoller. Long-distance quantum communication with atomic ensembles and linear optics. *Nature*, 414 (6862):413–418, 2001.

[18] H. J. Kimble. The quantum internet. *Nature*, 453(7198):1023–1030, 2008.

[19] Charles H. Bennett and Gilles Brassard. Quantum cryptography: Quantum key distribution and coin tossing. *Proceedings of the IEEE International Conference on Computers, Systems and Signal Processing*, pages 175–179, 1984.

[20] Nicolas Gisin, Grégoire Ribordy, Wolfgang Tittel, and Hugo Zbinden. Quantum cryptography. *Rev. Mod. Phys.*, 74(1):145–195, 2002.

[21] Gilles Brassard, Norbert Lütkenhaus, Tal Mor, and Barry C. Sanders. Limitations on practical quantum cryptography. *Phys. Rev. Lett.*, 85(6):1330–1333, 2000.

[22] Valerio Scarani, Helle Bechmann-Pasquinucci, Nicolas J. Cerf, Miloslav Dušek, Norbert Lütkenhaus, and Momtchil Peev. The security of practical quantum key distribution. *Rev. Mod. Phys.*, 81(3):1301–1350, 2009.

[23] Won-Young Hwang. Quantum key distribution with high loss: Toward global secure communication. *Phys. Rev. Lett.*, 91(5):057901, 2003.

[24] Pieter Kok, William J. Munro, Kae Nemoto, T. C. Ralph, Jonathan P. Dowling, and Gerard J. Milburn. Linear optical quantum computing with photonic qubits. *Rev. Mod. Phys.*, 79(1):135, 2007.

[25] E. Knill, Raymond Laflamme, and Gerard J. Milburn. A scheme for efficient quantum computation with linear optics. *Nature*, 409(6816):46–52, 2001.

[26] Hans J. Briegel, W. Dür, Juan Ignacio Cirac, and Peter Zoller. Quantum repeaters: The role of imperfect local operations in quantum communication. *Phys. Rev. Lett.*, 81(26):5932–5935, 1998.

[27] Dik Bouwmeester, Jian-Wei Pan, Klaus Mattle, Manfred Eibl, Harald Weinfurter, and Anton Zeilinger. Experimental quantum teleportation. *Nature*, 390(6660): 575–579, 1997.

[28] E. Moreau, I. Robert, L. Manin, V. Thierry-Mieg, Jean-Michel Gérard, and I. Abram. Quantum cascade of photons in semiconductor quantum dots. *Phys. Rev. Lett.*, 87(18):183601, 2001.

[29] Philippe Grangier, Barry Sanders, and Jelena Vuckovic. Focus on single photons on demand. *New J. Phys.*, 6, 2004.

[30] Axel Kuhn, Markus Hennrich, and Gerhard Rempe. Deterministic single-photon source for distributed quantum networking. *Phys. Rev. Lett.*, 89(6):067901, 2002.

[31] M. Keller, B. Lange, K. Hayasaka, W. Lange, and H. Walther. Continuous generation of single photons with controlled waveform in an ion-trap cavity system. *Nature*, 431(7012):1075–1078, 2004.

[32] Christian Brunel, Brahim Lounis, Philippe Tamarat, and Michel Orrit. Triggered source of single photons based on controlled single molecule fluorescence. *Phys. Rev. Lett.*, 83(14):2722–2725, 1999.

[33] Brahim Lounis and W. E. Moerner. Single photons on demand from a single molecule at room temperature. *Nature*, 407(6803):491–493, 2000.

[34] Peter Michler, Atac Imamoğlu, M. D. Mason, P. J. Carson, G. F. Strouse, and S. K. Buratto. Quantum correlation among photons from a single quantum dot at room temperature. *Nature*, 406(6799):968–970, 2000.

[35] M. Nirmal, B. O. Dabbousi, M. G. Bawendi, J. J. Macklin, J. K. Trautman, T. D. Harris, and L. E. Brus. Fluorescence intermittency in single cadmium selenide nanocrystals. *Nature*, 383(6603):802–804, 1996.

[36] Pavel Frantsuzov, Masaru Kuno, Boldizsar Janko, and Rudolph A. Marcus. Universal emission intermittency in quantum dots, nanorods and nanowires. *Nat. Phys.*, 4(5):519–522, 2008.

[37] Christian Kurtsiefer, Sonja Mayer, Patrick Zarda, and Harald Weinfurter. Stable solid-state source of single photons. *Phys. Rev. Lett.*, 85(2):290–293, 2000.

[38] Alexios Beveratos, Sergei Kühn, Rosa Brouri, Thierry Gacoin, Jean-Philippe Poizat, and Philippe Grangier. Room temperature stable single-photon source. *Eur. Phys. J. D*, 18(2):191–196, 2002.

[39] D. A. Kleinman. Theory of optical parametric noise. *Phys. Rev.*, 174(3):1027–1041, 1968.

[40] Robert L. Byer and S. E. Harris. Power and bandwidth of spontaneous parametric emission. *Phys. Rev. A*, 168(3):1064–1068, 1968.

[41] Leonard Mandel and Emil Wolf. *Optical coherence and quantum optics*. Cambridge University Press, Cambridge, 1995.

[42] David C. Burnham and Donald L. Weinberg. Observation of simultaneity in parametric production of optical photon pairs. *Phys. Rev. Lett.*, 25(2):84–87, 1970.

[43] Paul G. Kwiat, Klaus Mattle, Harald Weinfurter, Anton Zeilinger, Alexander V. Sergienko, and Yanhua Shih. New high-intensity source of polarization-entangled photon pairs. *Phys. Rev. Lett.*, 75(24):4337–4341, 1995.

[44] W. T. Buttler, R. J. Hughes, S. K. Lamoreaux, G. L. Morgan, J. E. Nordholt, and C. G. Peterson. Daylight quantum key distribution over 1.6 km. *Phys. Rev. Lett.*, 84(24):5652–5655, 2000.

[45] Rupert Ursin, Felix Tiefenbacher, Tobias Schmitt-Manderbach, Henning Weier, Thomas Scheidl, M. Lindenthal, Bibiane Blauensteiner, Thomas Jennewein, Josep Perdigues, P. Trojek, B. Omer, Martin Fürst, M. Meyenburg, John G. Rarity, Zoran Sodnik, C. Barbieri, Harald Weinfurter, and Anton Zeilinger. Entanglement-based quantum communication over 144km. *Nat. Phys.*, 3(7):481–486, 2007.

[46] C. Bonato, A. Tomaello, V. Da Deppo, G. Naletto, and P. Villoresi. Feasibility of satellite quantum key distribution. *New J. Phys.*, 11(4):045017, 2009.

[47] David Höckel, Lars Koch, Eugen Martin, and Oliver Benson. Ultranarrow bandwidth spectral filtering for long-range free-space quantum key distribution at daytime. *Opt. Lett.*, 34(20):3169–3171, 2009.

[48] Christian Maurer, Christoph Becher, Carlos Russo, Jürgen Eschner, and Rainer Blatt. A single-photon source based on a single Ca^+ ion. *New J. Phys.*, 6(1):94, 2004.

[49] Shengwang Du, Pavel Kolchin, Chinmay Belthangady, G. Y. Yin, and S. E. Harris. Subnatural linewidth biphotons with controllable temporal length. *Phys. Rev. Lett.*, 100(18):183603, 2008.

[50] Y. J. Lu and Z. Y. Ou. Optical parametric oscillator far below threshold: Experiment versus theory. *Phys. Rev. A*, 62(3):033804, 2000.

[51] Christopher E. Kuklewicz, Franco Ngai Chuen Wong, and Jeffrey H. Shapiro. Time-bin-modulated biphotons from cavity-enhanced down-conversion. *Phys. Rev. Lett.*, 97(22):223601, 2006.

[52] Jonas S. Neergaard-Nielsen, B. Melholt Nielsen, H. Takahashi, A. I. Vistnes, and Eugene S. Polzik. High purity bright single photon source. *Opt. Express*, 15(13): 7940–7949, 2007.

[53] Xiao-Hui Bao, Yong Qian, Jian Yang, Han Zhang, Zeng-Bing Chen, Tao Yang, and Jian-Wei Pan. Generation of narrow-band polarization-entangled photon pairs for atomic quantum memories. *Phys. Rev. Lett.*, 101(19):190501, 2008.

[54] Matthias Scholz, Lars Koch, and Oliver Benson. Statistics of narrow-band single photons for quantum memories generated by ultrabright cavity-enhanced parametric down-conversion. *Phys. Rev. Lett.*, 102(6):063603, 2009.

[55] Matthias Scholz, Lars Koch, R. Ullmann, and Oliver Benson. Single-mode operation of a high-brightness narrow-band single-photon source. *Appl. Phys. Lett.*, 94 (20):201105, 2009.

[56] Matthias Scholz, Lars Koch, and Oliver Benson. Analytical treatment of spectral properties and signal-idler intensity correlations for a double-resonant optical parametric oscillator far below threshold. *Opt. Comm.*, 282(17):3518–3523, 2009.

[57] Matthias Scholz. *New Light Sources for Quantum Information Processing*. PhD thesis, Humboldt-Universität zu Berlin, 2009.

[58] Dennis Dieks. Communication by EPR devices. *Phys. Lett. A*, 92(6):271–272, 1982.

[59] William K. Wootters and W. H. Zurek. A single quantum cannot be cloned. *Nature*, 299(5886):802–803, 1982.

[60] Ryszard Horodecki, Paweł Horodecki, Michał Horodecki, and Karol Horodecki. Quantum entanglement. *Rev. Mod. Phys.*, 81(2):865, 2009.

[61] Marek Zukowski, Anton Zeilinger, M. A. Horne, and Artur K. Ekert. "Event-ready-detectors" Bell experiment via entanglement swapping. *Phys. Rev. Lett.*, 71 (26):4287–4290, 1993.

[62] Nicolas Sangouard, Christoph Simon, Hugues de Riedmatten, and Nicolas Gisin. Quantum repeaters based on atomic ensembles and linear optics. *arXiv:0906.2699v2*, 2009.

[63] K.-J. Boller, Atac Imamoğlu, and S. E. Harris. Observation of electromagnetically induced transparency. *Phys. Rev. Lett.*, 66(20):2593–2596, 1991.

[64] S. E. Harris. Electromagnetically induced transparency with matched pulses. *Phys. Rev. Lett.*, 70(5):552–555, 1993.

[65] Michael Fleischhauer and Mikhail D. Lukin. Dark-state polaritons in electromagnetically induced transparency. *Phys. Rev. Lett.*, 84(22):5094–5097, 2000.

[66] M. Bajcsy, Alexander S. Zibrov, and Mikhail D. Lukin. Stationary pulses of light in an atomic medium. *Nature*, 426(6967):638–641, 2003.

[67] C. P. Sun, Y. Li, and X. F. Liu. Quasi-spin-wave quantum memories with a dynamical symmetry. *Phys. Rev. Lett.*, 91(14):147903, 2003.

[68] Daisuke Akamatsu, Keiichirou Akiba, and Mikio Kozuma. Electromagnetically induced transparency with squeezed vacuum. *Phys. Rev. Lett.*, 92(20):203602, 2004.

[69] Matthew D. Eisaman, Axel André, F. Massou, Michael Fleischhauer, Alexander S. Zibrov, and Mikhail D. Lukin. Electromagnetically induced transparency with tunable single-photon pulses. *Nature*, 438(7069):837–841, 2005.

[70] T. Chanelière, D. N. Matsukevich, S. D. Jenkins, S.-Y. Lan, T. A. B. Kennedy, and A. Kuzmich. Storage and retrieval of single photons transmitted between remote quantum memories. *Nature*, 438(7069):833–836, 2005.

[71] David F. Phillips, A. Fleischhauer, Alois Mair, Ronald L. Walsworth, and Mikhail D. Lukin. Storage of light in atomic vapor. *Phys. Rev. Lett.*, 86(5): 783, 2001.

[72] Irina Novikova, Alexey V. Gorshkov, David F. Phillips, Anders S. Sørensen, Mikhail D. Lukin, and Ronald L. Walsworth. Optimal control of light pulse storage and retrieval. *Phys. Rev. Lett.*, 98(24):243602, 2007.

[73] Svenja Knappe, Vishal Shah, Peter D. D. Schwindt, Leo Hollberg, John Kitching, Li-Anne Liew, and John Moreland. A microfabricated atomic clock. *Appl. Phys. Lett.*, 85(9):1460–1462, 2004.

[74] Fritz Henneberger and Oliver Benson. *Semiconductor Quantum Bits*. World Scientific, 2008.

[75] D. Pinotsi and Atac Imamoğlu. Single photon absorption by a single quantum emitter. *Phys. Rev. Lett.*, 100(9):093603, 2008.

[76] K. F. Reim, J. Nunn, V. O. Lorenz, B. J. Sussman, K. C. Lee, K Langford, D. Jaksch, and Ian A. Walmsley. Towards high-speed optical quantum memories. *Nat. Photon.*, 4(4):218–221, 2010.

[77] Dik Bouwmeester, Artur K. Ekert, and Anton Zeilinger. *The Physics of Quantum Information: Quantum Cryptography, Quantum Teleportation, Quantum Computation*. Springer, Berlin, 2000.

[78] A. Kuzmich, W. P. Bowen, A. D. Boozer, Andrea Boca, Chin-Wen Chou, L.-M. Duan, and H. J. Kimble. Generation of nonclassical photon pairs for scalable quantum communication with atomic ensembles. *Nature*, 423(6941):731–734, 2003.

[79] Caspar H. van der Wal, Matthew D. Eisaman, Axel André, Ronald L. Walsworth, David F. Phillips, Alexander S. Zibrov, and Mikhail D. Lukin. Atomic memory for correlated photon states. *Science*, 301(5630):196–200, 2003.

[80] Christoph Simon, Mikael Afzelius, Jürgen Appel, A. Boyer de la Giroday, S. J. Dewhurst, Nicolas Gisin, C. Y. Hu, F. Jelezko, S. Kröll, J. H. Müller, J. Nunn, Eugene S. Polzik, John G. Rarity, H. De Riedmatten, W. Rosenfeld, Andrew J. Shields, N. Sköld, R. Mark Stevenson, Rob T. Thew, Ian A. Walmsley, M. C. Weber, Harald Weinfurter, J. Wrachtrup, and R. J. Young. Quantum memories. *Eur. Phys. J. D*, 58(1):1–22, 2010.

[81] G. I. Taylor. Interference fringes with feeble light. *Proceedings of the Cambridge Philosophical Society*, 15:114–115, 1909.

[82] Roy Jay Glauber. The quantum theory of optical coherence. *Phys. Rev.*, 130(6): 2529–2539, 1963.

[83] Daniel Frank Walls and Gerard J. Milburn. *Quantum Optics*. Springer Berlin Heidelberg, 2008.

[84] R. Hanbury Brown and R. Q. Twiss. A test of a new type of stellar interferometer on Sirius. *Nature*, 178(4541):1046–1048, 1956.

[85] Thomas Aichele. *Detection and Generation of Non-Classical Light States from Single Quantum Emitters*. PhD thesis, Humboldt-Universität zu Berlin, 2005.

[86] A. Batalov, V Jacques, F. Kaiser, P. Siyushev, P. Neumann, L. J. Rogers, R. L. McMurtrie, N. B. Manson, F. Jelezko, and J. Wrachtrup. Low temperature studies of the excited-state structure of negatively charged nitrogen-vacancy color centers in diamond. *Phys. Rev. Lett.*, 102(19):195506, 2009.

[87] J. H. N. Loubser and J. A. van Wyk. Electron spin resonance in the study of diamond. *Rep. Prog. Phys.*, 41(8):1201, 1978.

[88] Philippe Tamarat, N. B. Manson, J. P. Harrison, R. L. McMurtrie, A. Nizovtsev, C. Santori, R. G. Beausoleil, P. Neumann, T. Gaebel, F. Jelezko, P. R. Hemmer, and J. Wrachtrup. Spin-flip and spin-conserving optical transitions of the nitrogen-vacancy centre in diamond. *New J. Phys.*, 10(4):045004, 2008.

[89] F. Jelezko and J. Wrachtrup. Single defect centres in diamond: A review. *Phys. Stat. Sol. A*, 203(13):3207–3225, 2006.

[90] Michael Barth. *Hybrid Nanophotonic Elements and Sensing Devices based on Photonic Crystal Structures*. PhD thesis, Humboldt-Universität zu Berlin, 2010.

[91] A. Verevkin, A. Pearlman, W. Słysz, J. Zhang, M. Currier, A. Korneev, G. Chulkova, O. Okunev, P. Kouminov, K. Smirnov, B. Voronov, G. N. Gol'tsman, and Roman Sobolewski. Ultrafast superconducting single-photon detectors for

near-infrared-wavelength quantum communications. *J. Mod. Opt.*, 51 9:1447–1458, 2004.

[92] G. N. Gol'tsman, A. Korneev, I. Rubtsova, I. Milostnaya, G. Chulkova, Olga Minaeva, K. Smirnov, B. Voronov, W. Słysz, A. Pearlman, A. Verevkin, and Roman Sobolewski. Ultrafast superconducting single-photon detectors for near-infrared-wavelength quantum communications. *Phys. Stat. Sol. C*, 2(5):1480–1488, 2005.

[93] Sander Dorenbos. Fabrication and characterization of superconducting detectors for single photon counting. Master's thesis, Delft University of Technology, 2007.

[94] Stefan Schietinger, Michael Barth, Thomas Aichele, and Oliver Benson. Plasmon-enhanced single photon emission from a nanoassembled metal-diamond hybrid structure at room temperature. *Nano Lett.*, 9(4):1694–1698, 2009.

[95] M. Houe and Paul D. Townsend. An introduction to methods of periodic poling for second-harmonic generation. *J. Phys. D*, 28(9):1747–1763, 1995.

[96] Theodor W. Hänsch and B. Couillaud. Laser frequency stabilization by polarization spectroscopy of a reflecting reference cavity. *Opt. Comm.*, 35(3):441–444, 1980.

[97] A. Mooradian and M. Fleming. Spectral characteristics of external-cavity controlled semiconductor lasers. *IEEE J. Quantum Electron.*, 17(1):44–49, 1981.

[98] R. Wyatt and W. J. Devlin. 10 kHz linewidth 1.5μm InGaAsP external cavity laser with 55 nm tuning range. *Electron. Lett.*, 19(3):110–112, 1983.

[99] Gary C. Bjorklund. Frequency-modulation spectroscopy: A new method for measuring weak absorptions and dispersions. *Opt. Lett.*, 5(1):15–17, 1980.

[100] Gary C. Bjorklund, M. D. Levenson, W. Lenth, and C. Ortiz. Frequency modulation (FM) spectroscopy. *Appl. Phys. B*, 32(3):145–152, 1983.

[101] Wolfgang Demtröder. *Laser Spectroscopy. Basic Concepts and Instrumentation.* Spinger, Berlin, 2007.

[102] Y. J. Lu, R. L. Campbell, and Z. Y. Ou. Mode-locked two-photon states. *Phys. Rev. Lett.*, 91(16):163602, 2003.

[103] E. Bocquillon, C. Couteau, M. Razavi, R. Laflamme, and G. Weihs. Coherence measures for heralded single-photon sources. *Phys. Rev. A*, 79(3):035801, 2009.

[104] M. Razavi, I Söllner, E. Bocquillon, C. Couteau, R. Laflamme, and G. Weihs. Characterizing heralded single-photon sources with imperfect measurement devices. *J. Phys. B*, 42(11):114013, 2009.

[105] Stefano Bettelli. Comment on "Coherence measures for heralded single-photon sources". *Phys. Rev. A*, 81(3):037801, 2010.

[106] Jeffrey H. Shapiro. Quantum noise and excess noise in optical homodyne and heterodyne receivers. *IEEE J. Quantum Electron.*, 21(3):237–250, 1985.

[107] Jeffrey H. Shapiro and Ke-Xun Sun. Semiclassical versus quantum behavior in fourth-order interference. *J. Opt. Soc. Am. B*, 11(6):1130–1141, 1994.

[108] Horace P. Yuen. Two-photon coherent states of the radiation field. *Phys. Rev. A*, 13(6):2226–2243, 1976.

[109] Franco Ngai Chuen Wong, Jeffrey H. Shapiro, and T. Kim. Efficient generation of polarization-entangled photons in a nonlinear crystal. *Laser Phys.*, 16(11):1517–1524, 2006.

[110] Jeffrey H. Shapiro. Quantum Gaussian noise. *Proc. SPIE*, 5111(1):382–395, 2003.

[111] Sylvain Fasel, Olivier Alibart, Sébastien Tanzilli, Pascal Baldi, Alexios Beveratos, Nicolas Gisin, and Hugo Zbinden. High-quality asynchronous heralded single-photon source at telecom wavelength. *New J. Phys.*, 6:163–173, 2004.

[112] Ulrike Herzog, Matthias Scholz, and Oliver Benson. Theory of biphoton generation in a single-resonant optical parametric oscillator far below threshold. *Phys. Rev. A*, 77(2):023826, 2008.

[113] J. D. Franson. Bell inequality for position and time. *Phys. Rev. Lett.*, 62(19): 2205–2208, 1989.

[114] Dan Sadot and Efraim Boimovich. Tunable optical filters for dense wdm networks. *IEEE Commun. Mag.*, 36(12):50, 1998.

[115] Giuliano Scarcelli and Seok Hyun Yun. Confocal brillouin microscopy for three-dimensional mechanical imaging. *Nat. Photon.*, 2(1):39–43, 2008.

[116] P. Piironen and E. W. Eloranta. Demonstration of a high-spectral-resolution lidar based on an iodine absorption filter. *Opt. Lett.*, 19(3):234–236, 1994.

[117] J. M. Vaughan. *The Fabry-Perot Interferometer.* Taylor & Francis, New York, 1989.

[118] C. Roychoudhuri and M. Hercher. Stable multipass Fabry-Perot interferometer: design and analysis. *Appl. Opt.*, 16:2514, 1977.

[119] Robert Chabbal. Finesse limite d'un Fabry-Perot formé de lames imparfaites. *J. Phys. Radium*, 19:295–300, 1958.

[120] P. D. Atherton, Newrick K. Reay, J. Ring, and T. R. Hicks. Tunable Fabry-Perot filters. *Opt. Eng.*, 20(6):806–814, 1981.

[121] S. M. Lindsay, M. W. Anderson, and J. R. Sandercock. Construction and alignment of a high performance multipass vernier tandem Fabry–Perot interferometer. *Rev. Sci. Instrum.*, 52(10):1478, 1981.

[122] J. G. Dil, N. C. J. A. van Hijningen, F. van Dorst, and R. M. Aarts. Tandem multipass Fabry-Perot interferometer for Brillouin scattering. *Appl. Opt.*, 20(8): 1374, 1981.

[123] M. Avenhaus, H. B. Coldenstrodt-Ronge, K. Laiho, W. Mauerer, Ian A. Walmsley, and Christine Silberhorn. Photon number statistics of multimode parametric down-conversion. *Phys. Rev. Lett.*, 101(5):053601, 2008.

[124] Peter J. Mosley, Andreas Christ, Andreas Eckstein, and Christine Silberhorn. Direct measurement of the spatial-spectral structure of waveguided parametric down-conversion. *Phys. Rev. Lett.*, 103(23):233901, 2009.

[125] Hiroki Takesue, Sae Woo Nam, Qiang Zhang, Robert H. Hadfield, Toshimori Honjo, Kiyoshi Tamaki, and Yoshihisa Yamamoto. Quantum key distribution over a 40-dB channel loss using superconducting single-photon detectors. *Nat. Photon.*, 1(6):343–348, 2007.

[126] M. Rau, Martin Fürst, H. Krauss, S. Schreiner, Henning Weier, and Harald Weinfurter. Daylight free-space quantum key distribution. CLEO/Europe-EQEC Munich, ED5.5, 2009.

[127] D. Elser, T. Bartley, B. Heim, Ch. Wittmann, D. Sych, and G. Leuchs. Feasibility of free space quantum key distribution with coherent polarization states. *New J. Phys.*, 11(4):045014, 2009.

[128] Momtchil Peev, C. Pacher, R. Alleaume, C. Barreiro, J. Bouda, W. Boxleitner, T. Debuisschert, Eleni Diamanti, M. Dianati, J. F. Dynes, Sylvain Fasel, S. Fossier, Martin Fürst, Jean-Daniel Gautier, O. Gay, Nicolas Gisin, Philippe Grangier, A. Happe, Y. Hasani, M. Hentschel, H. Hubel, G. Humer, T. Langer, M. Legre, R. Lieger, J. Lodewyck, T. Lörunser, N. Lütkenhaus, A. Marhold, T. Matyus, Oliver Maurhardt, L. Monat, S. Nauerth, J.-B. Page, Andreas Poppe, E. Querasser, Grégoire Ribordy, S. Robyr, Louis Salvail, A. W. Sharpe, Andrew J. Shields, D. Stucki, M. Suda, C. Tamas, T. Themel, Rob T. Thew, Y. Thoma, A. Treiber, P. Trinkler, Rosa Tualle-Brouri, F. Vannel, N. Walenta, Henning Weier, Harald Weinfurter, I. Wimberger, Z. L. Yuan, Hugo Zbinden, and Anton Zeilinger. The SECOQC quantum key distribution network in Vienna. *New J. Phys.*, 11(7): 075001, 2009.

[129] Markus Aspelmeyer, Thomas Jennewein, Martin Pfennigbauer, W. R. Leeb, and Anton Zeilinger. Long-distance quantum communication with entangled photons using satellites. *IEEE J. Sel. Top. Quantum Electron.*, 9(6):1541–1551, 2003.

[130] Cheng-Zhi Peng, Tao Yang, Xiao-Hui Bao, Jun Zhang, Xian-Min Jin, Fa-Yong Feng, Bin Yang, Jian Yang, Juan Yin, Qiang Zhang, Nan Li, Bao-Li Tian, and Jian-Wei Pan. Experimental free-space distribution of entangled photon pairs over 13 km: Towards satellite-based global quantum communication. *Phys. Rev. Lett.*, 94(15):150501, 2005.

[131] Tobias Schmitt-Manderbach, Henning Weier, Martin Fürst, Rupert Ursin, Felix Tiefenbacher, Thomas Scheidl, Josep Perdigues, Zoran Sodnik, Christian Kurtsiefer, John G. Rarity, Anton Zeilinger, and Harald Weinfurter. Experimental demonstration of free-space decoy-state quantum key distribution over 144 km. *Phys. Rev. Lett.*, 98(1):010504, 2007.

[132] Alessandro Fedrizzi, Rupert Ursin, Thomas Herbst, Matteo Nespoli, Robert Prevedel, Thomas Scheidl, Felix Tiefenbacher, Thomas Jennewein, and Anton Zeilinger. High-fidelity transmission of entanglement over a high-loss free-space channel. *Nat. Phys.*, 5:389–392, 2009.

[133] P. Villoresi, Thomas Jennewein, F. Tamburini, Markus Aspelmeyer, C. Bonato, Rupert Ursin, C. Pernechele, V. Luceri, G. Bianco, Anton Zeilinger, and C. Barbieri. Experimental verification of the feasibility of a quantum channel between space and earth. *New J. Phys.*, 10(3):033038, 2008.

[134] Josep Maria Perdigues Armengol, Bernhard Furch, Clovis Jacinto de Matos, Olivier Minster, Luigi Cacciapuoti, Martin Pfennigbauer, Markus Aspelmeyer, Thomas Jennewein, Rupert Ursin, Tobias Schmitt-Manderbach, Guy Baister, John G. Rarity, Walter Leeb, Cesare Barbieri, Harald Weinfurter, and Anton Zeilinger. Quantum communications at ESA: Towards a space experiment on the ISS. *Acta Astronautica*, 63(1-4):165–178, 2008.

[135] Miao Er-long, Han Zheng-fu, Gong Shun-sheng, Zhang Tao, Diao Da-sheng, and Guo Guang-can. Background noise of satellite-to-ground quantum key distribution. *New J. Phys.*, 7:215, 2005.

[136] Hoi-Kwong Lo, Xiongfeng Ma, and Kai Chen. Decoy state quantum key distribution. *Phys. Rev. Lett.*, 94(23):230504, 2005.

[137] Xiang-Bin Wang. Beating the photon-number-splitting attack in practical quantum cryptography. *Phys. Rev. Lett.*, 94(23):230503, 2005.

[138] Federico Dios, Juan Antonio Rubio, Alejandro Rodríguez, and Adolfo Comerón. Scintillation and beam-wander analysis in an optical ground station-satellite uplink. *Appl. Opt.*, 43(19):3866–3873, 2004.

[139] L. C. Andrews, R. L. Phillips, and P. T. Yu. Optical scintillations and fade statistics for a satellite-communication system. *Appl. Opt.*, 34(33):7742–7751, 1995.

[140] V. Hansen. Spectral distribution of solar radiation on clear days: A comparison between measurements and model estimates. *J. Appl. Meteorol.*, 23:772–780, 1984.

[141] C. Leinert, S. Bowyer, L. K. Haikala, M. S. Hanner, M. G. Hauser, A.-C. Levasseur-Regourd, I. Mann, K. Mattila, W. T. Reach, W. Schlosser, H. J. Staude, G. N. Toller, J. L. Weiland, J. L. Weinberg, and A. N. Witt. The 1997 reference of diffuse night sky brightness. *Astron. Astrophys. Suppl. Ser.*, 127(1):1–99, 1998.

[142] Thomas Weyrauch and Mikhail A. Vorontsov. Free-space laser communications with adaptive optics: Atmospheric compensation experiments. *J. Opt. Fiber Commun. Rep.*, 1(4):355–379, 2004.

[143] Thomas Weyrauch and Mikhail A. Vorontsov. Dynamic wave-front distortion compensation with a 134-control-channel submillisecond adaptive system. *Opt. Lett.*, 27(9):751–753, 2002.

[144] Thomas Aichele, Gaël Reinaudi, and Oliver Benson. Separating cascaded photons from a single quantum dot: Demonstration of multiplexed quantum cryptography. *Phys. Rev. B*, 70(23):235329, 2004.

[145] Klemens Hammerer, Anders S. Sørensen, and Eugene S. Polzik. Quantum interface between light and atomic ensembles. *Rev. Mod. Phys.*, 82(2):1041–1093, 2010.

[146] A. Kuzmich, Klaus Mølmer, and Eugene S. Polzik. Spin squeezing in an ensemble of atoms illuminated with squeezed light. *Phys. Rev. Lett.*, 79(24):4782–4785, 1997.

[147] Lene Vestergaard Hau, S. E. Harris, Zachary Dutton, and Cyrus H. Behroozi. Light speed reduction to 17 metres per second in an ultracold atomic gas. *Nature*, 397(6720):594–598, 1999.

[148] Danielle A. Braje, Vlatko Balić, G. Y. Yin, and S. E. Harris. Low-light-level nonlinear optics with slow light. *Phys. Rev. A*, 68(4):041801(R), 2003.

[149] Hoonsoo Kang and Yifu Zhu. Observation of large kerr nonlinearity at low light intensities. *Phys. Rev. Lett.*, 91(9):093601, 2003.

[150] H. Schmidt and Atac Imamoğlu. High-speed properties of a phase-modulation scheme based on electromagnetically induced transparency. *Opt. Lett.*, 23(13): 1007–1009, 1998.

[151] Q. A. Turchette, C. J. Hood, W. Lange, H. Mabuchi, and H. J. Kimble. Measurement of conditional phase shifts for quantum logic. *Phys. Rev. Lett.*, 75(25): 4710–4713, 1995.

[152] Alexey V. Gorshkov, Axel André, Michael Fleischhauer, Anders S. Sørensen, and Mikhail D. Lukin. Universal approach to optimal photon storage in atomic media. *Phys. Rev. Lett.*, 98(12):123601, 2007.

[153] H. Lee, Yuri V. Rostovtsev, C. J. Bednar, and Ali Javan. From laser-induced line narrowing to electro magnetically induced transparency: Closed system analysis. *Appl. Phys. B*, 76(1):33–39, 2003.

[154] C. Cohen-Tannoudji, J. Dupont-Roc, and G. Grynberg. *Atom-Photon Interactions: Basic Processes and Applications.* Wiley VCH, New York, 1998.

[155] Ali Javan, Olga Kocharovskaya, Hwang Lee, and Marlan O. Scully. Narrowing of electromagnetically induced transparency resonance in a Doppler-broadened medium. *Phys. Rev. A*, 66(1):013805, 2002.

[156] Theodor W. Hänsch and P. Toschek. Theory of a three-level gas laser amplifier. *Z. Phys. A*, 236(3):213–244, 1970.

[157] Daniel Adam Steck. Cesium D Line Data. Technical report, Los Alamos National Laboratory, 1998.

[158] Eden Figueroa, Frank Vewinger, Jürgen Appel, and Alexander I. Lvovsky. Decoherence of electromagnetically induced transparency in atomic vapor. *Opt. Lett.*, 31(17):2625, 2006.

[159] Olga Kocharovskaya, Yuri V. Rostovtsev, and Marlan O. Scully. Stopping light via hot atoms. *Phys. Rev. Lett.*, 86(4):628–631, 2001.

[160] P. Rabinowitz, J. Latourrette, and G. Gould. AFC optical heterodyne detector. *Proc. IEEE*, 51:857–858, 1963.

[161] L. H. Enloe and J. L. Rodda. Laser phase-locked loop. *Proc. IEEE*, 53(2):165–166, 1965.

[162] John L. Hall, Ma Long-Sheng, and G. Kramer. Principles of optical phase-locking: Application to internal mirror He-Ne lasers phase-locked via fast control of the discharge current. *IEEE J. Quantum Electron.*, 23(4):427–437, 1987.

[163] Jun Ye and John L. Hall. Optical phase locking in the microradian domain: potential applications to NASA spaceborne optical measurements. *Opt. Lett.*, 24(24): 1838–1840, 1999.

[164] Wei Liang, Naresh Satyan, Firooz Aflatouni, Amnon Yariv, Anthony Kewitsch, George Rakuljic, and Hossein Hashemi. Coherent beam combining with multilevel optical phase-locked loops. *J. Opt. Soc. Am. B*, 24(12):2930–2939, 2007.

[165] J. Stuhler, M. Fattori, T. Petelski, and G.M. Tino. MAGIA - using atom interferometry to determine the Newtonian gravitational constant. *J. Opt. B*, 5(2): S75–S81, 2003.

[166] A.M. Marino and C. R. Stroud, Jr. Phase-locked laser system for use in atomic coherence experiments. *Rev. Sci. Instrum.*, 79(1):013104, 2008.

[167] Luigi Cacciapuoti, M. de Angelis, M. Fattori, G. Lamporesi, T. Petelski, M. Prevedelli, J. Stuhler, and G.M. Tino. Analog + digital phase and frequency detector for phase locking of diode lasers. *Rev. Sci. Instrum.*, 76(5):053111, 2005.

[168] Masaaki Imai and Koji Kawakita. Measurement of direct frequency modulation characteristics of laser diodes by Michelson interferometry. *Appl. Opt.*, 29(3):348–353, 1990.

[169] Motoichi Ohtsu. *Highly coherent semiconductor lasers*. Artech House, Boston, London, 1991.

[170] U. Tietze and Ch. Schenk. *Halbleiter-Schaltungstechnik*. Springer, Berlin, 1993.

[171] Miao Zhu and John L. Hall. Stabilization of optical phase/frequency of a laser system: application to a commercial dye laser with an external stabilizer. *J. Opt. Soc. Am. B*, 10(5):802, 1993.

[172] T. E. Sterne. Multi-lamellar cylindrical magnetic shields. *Rev. Sci. Instrum.*, 6 (10):324–326, 1935.

[173] Yong-Fan Chen, Yu-Chen Liu, Zen-Hsiang Tsai, Shih-Hao Wang, and Ite A. Yu. Beat-note interferometer for direct phase measurement of photonic information. *Phys. Rev. A*, 72(3):033812, 2005.

[174] J. Alnis, A. Matveev, N. Kolachevsky, Th. Udem, and Theodor W. Hänsch. Subhertz linewidth diode lasers by stabilization to vibrationally and thermally compensated ultralow-expansion glass Fabry-Pérot cavities. *Phys. Rev. A*, 77(5):053809, 2008.

[175] Sheng-wey Chiow, Sven Herrmann, Holger Müller, and Steven Chu. 6W, 1 kHz linewidth, tunable continuous-wave near-infrared laser. *Opt. Express*, 17(7):5246–5250, 2009.

[176] B. E. Unks, N. A. Proite, and D. D. Yavuz. Generation of high-power laser light with gigahertz splitting. *Rev. Sci. Instrum.*, 78(8):083108, 2007.

[177] H. Schmidt and Atac Imamoğlu. Giant kerr nonlinearities obtained by electromagnetically induced transparency. *Opt. Lett.*, 21(23):1936–1938, 1996.

[178] Mirko Lobino, C. Kupchak, Eden Figueroa, and Alexander I. Lvovsky. Memory for light as a quantum process. *Phys. Rev. Lett.*, 102(20):203601, 2009.

[179] Stephanie Manz, Thomas Fernholz, Jörg Schmiedmayer, and Jian-Wei Pan. Collisional decoherence during writing and reading quantum states. *Phys. Rev. A*, 75 (4):040101, 2007.

[180] Pavel Kolchin, Chinmay Belthangady, Shengwang Du, G. Y. Yin, and S. E. Harris. Electro-optic modulation of single photons. *Phys. Rev. Lett.*, 101(10):103601, 2008.

[181] H. P. Specht, J. Bochmann, Martin Mücke, B. Weber, Eden Figueroa, David L. Moehring, and Gerhard Rempe. Phase shaping of single-photon wave packets. *Nat. Photon*, 3(8):469–472, 2009.

[182] Nathaniel B. Phillips, Alexey V. Gorshkov, and Irina Novikova. Optimal light storage in atomic vapor. *Phys. Rev. A*, 78(2):023801, 2008.

[183] Irina Novikova, Nathaniel B. Phillips, and Alexey V. Gorshkov. Optimal light storage with full pulse-shape control. *Phys. Rev. A*, 78(2):021802, 2008.

[184] Kyo Inoue, Edo Waks, and Yoshihisa Yamamoto. Differential phase shift quantum key distribution. *Phys. Rev. Lett.*, 89(3):037902, 2002.

[185] I. Marcikic, Hugues de Riedmatten, Wolfgang Tittel, Valerio Scarani, Hugo Zbinden, and Nicolas Gisin. Time-bin entangled qubits for quantum communication created by femtosecond pulses. *Phys. Rev. A*, 66(6):062308, 2002.

[186] Kaige Wang. Quantum theory of two-photon wavepacket interference in a beamsplitter. *J. Phys. B*, 39(18):R293, 2006.

[187] Wolfgang Tittel, Jürgen Brendel, Hugo Zbinden, and Nicolas Gisin. Quantum cryptography using entangled photons in energy-time Bell states. *Phys. Rev. Lett.*, 84(20):4737–4740, 2000.

[188] Jürgen Brendel, Nicolas Gisin, Wolfgang Tittel, and Hugo Zbinden. Pulsed energy-time entangled twin-photon source for quantum communication. *Phys. Rev. Lett.*, 82(12):2594–2597, 1999.

[189] A. R. Dixon, Z. L. Yuan, J. F. Dynes, A. W. Sharpe, and Andrew J. Shields. Gigahertz decoy quantum key distribution with 1 Mbit/s secure key rate. *Opt. Express*, 16(23):18790–18979, 2008.

[190] Kyung Soo Choi, Hui Deng, J. Laurat, and H. J. Kimble. Mapping photonic entanglement into and out of a quantum memory. *Nature*, 452(7183):67–71, 2008.

[191] R. Mark Stevenson, R. J. Young, P. Atkinson, Ken Cooper, David A. Ritchie, and Andrew J. Shields. A semiconductor source of triggered entangled photon pairs. *Nature*, 439(7073):179–182, 2006.

[192] Artur K. Ekert. Quantum cryptography based on Bell's theorem. *Phys. Rev. Lett.*, 67(6):661–663, 1991.

[193] Mikhail D. Lukin. Colloquium: Trapping and manipulating photon states in atomic ensembles. *Rev. Mod. Phys.*, 75(2):457–472, 2003.

[194] Alexander I. Lvovsky, Barry C. Sanders, and Wolfgang Tittel. Optical quantum memory. *Nat. Photon.*, 3(12):706–714, 2009.

[195] Wolfgang Tittel, Mikael Afzelius, T. Chanelière, R. L. Cone, S. Kröll, Sergey A. Moiseev, and M. Sellars. Photon-echo quantum memory in solid state systems. *Laser & Photon. Rev.*, 4:244–267, 2010.

[196] M. Razavi, M. Piani, and N. Lütkenhaus. Quantum repeaters with imperfect memories: Cost and scalability. *Phys. Rev. A*, 80(3):032301, 2009.

[197] Christoph Simon, Hugues de Riedmatten, Mikael Afzelius, Nicolas Sangouard, Hugo Zbinden, and Nicolas Gisin. Quantum repeaters with photon pair sources and multimode memories. *Phys. Rev. Lett.*, 98(19):190503, 2007.

[198] A. E. Kozhekin, Klaus Mølmer, and Eugene S. Polzik. Quantum memory for light. *Phys. Rev. A*, 62(3):033809, 2000.

[199] J. Nunn, Ian A. Walmsley, M. G. Raymer, K. Surmacz, F. C. Waldermann, Z. Wang, and D. Jaksch. Mapping broadband single-photon wave packets into an atomic memory. *Phys. Rev. A*, 75(1):011401, 2007.

[200] O. S. Mishina, N. V. Larionov, A. S. Sheremet, I. M. Sokolov, and D. V. Kupriyanov. Stimulated Raman process in a scattering medium applied to the quantum memory scheme. *Phys. Rev. A*, 78(4):042313, 2008.

[201] K. F. Reim, J. Nunn, V. O. Lorenz, B. J. Sussman, K. C. Lee, K Langford, D. Jaksch, and Ian A. Walmsley. Coherent optical memory with GHz bandwidth. In *CLEO/QELS Conference*, 2010.

[202] Ryan M. Camacho, Praveen K. Vudyasetu, and John C. Howell. Four-wave-mixing stopped light in hot atomic rubidium vapour. *Nat. Photon.*, 3(2):103–106, 2009.

[203] K. Surmacz, J. Nunn, K. F. Reim, K. C. Lee, V. O. Lorenz, B. Sussman, Ian A. Walmsley, and D. Jaksch. Efficient spatially resolved multimode quantum memory. *Phys. Rev. A*, 78(3):033806, 2008.

[204] Chinmay Belthangady, Chih-Sung Chuu, Ite A. Yu, G. Y. Yin, J. M. Kahn, and S. E. Harris. Hiding single photons with spread spectrum technology. *Phys. Rev. Lett.*, 104(22):223601, 2010.

[205] R. Scholtz. The spread spectrum concept. *IEEE Trans. Commun,*, 25(8):748 – 755, 1977.

[206] J. J. Longdell, E. Fraval, M. J. Sellars, and N. B. Manson. Stopped light with storage times greater than one second using electromagnetically induced transparency in a solid. *Phys. Rev. Lett.*, 95(6):063601, 2005.

[207] E. Fraval, M. J. Sellars, and J. J. Longdell. Dynamic decoherence control of a solid-state nuclear-quadrupole qubit. *Phys. Rev. Lett.*, 95(3):030506, 2005.

[208] J. Nunn, K. F. Reim, K. C. Lee, V. O. Lorenz, B. J. Sussman, Ian A. Walmsley, and D. Jaksch. Multimode memories in atomic ensembles. *Phys. Rev. Lett.*, 101 (26):260502, 2008.

[209] C. K. Hong, Z. Y. Ou, and Leonard Mandel. Measurement of subpicosecond time intervals between two photons by interference. *Phys. Rev. Lett.*, 59(18):2044–2046, 1987.

[210] Edward B. Flagg, Andreas Muller, Sergey V. Polyakov, Alex Ling, Alan Migdall, and Glenn S. Solomon. Interference of single photons from two separate semiconductor quantum dots. *Phys. Rev. Lett.*, 104(13):137401, 2010.

Acknowledgement

First of all I like to express my deep gratitude to Professor Oliver Benson who has been my supervisor already long before I started my graduate studies. He taught me how to work scientifically and gave me substantial freedom during my work which allowed me to assume responsibility for the further development of the experiment. He strongly motivated me to bring in my own ideas and sponsored their realization and, at the same time, gave important advice, comprehensive and very helpful suggestions and professional guidance.

Dr. Matthias Scholz was my predecessor at the single photon storage experiment. He left a perfectly planned and far developed setup I could benefit from in manifold ways. This work would not have been possible without the know-how he built up and the experimental parts he had already designed and realized. I also thank Lars Koch who has worked intensively on the experiment and who will now take it over completely. I wish him great success.

I thank the Diploma and Bachelor students, Eugen Martin, Tim Kroh and Johannes Häger, who worked on diverse projects covered by this thesis, for their commitment to our common project and hard work they invested into the success.

Special thanks goes to Dipl.-Ing. Klaus Palis, who made many of the electronic components possible and contributed to the experiment in a variety of ways. I am also grateful to Alexander Walter who assembled numerous electronic devices in a highly professional manner.

Last but not least, I wish to thank all other members of the Nano Optics group for the enjoyable work environment and the good time I had in the group.

I highly appreciate the funding of my graduate studies by the Elsa-Neumann-scholarship from the State of Berlin.

Selbständigkeitserklärung

Ich erkläre, dass ich die vorliegende Arbeit selbständig und nur unter Verwendung der angegebenen Literatur und Hilfsmittel angefertigt habe.

Berlin, den 01.10.2010 David Höckel